Components for Monolithic Fiber Chirped Pulse Amplification Laser Systems

by

Michael Craig Swan

A dissertation submitted in partial fulfillment
of the requirements for the degree of
Doctor of Philosophy
(Physics)
in The University of Michigan
2009

Doctoral Committee:

Professor Almantas Galvanauskas, Co-Chair
Professor Duncan Steel, Co-Chair
Professor Paul Berman
Professor Theodore Norris
Associate Professor Cagliyan Kurdak

To my family

ACKNOWLEDGEMENTS

I would like to thank Almantas Galvanauskas for giving me the opportunity to work in an exciting area of research, and for taking the time to guide and support my work. To Duncan Steel for introducing me to Almantas, and for guidance and mentorship during my graduate career. To my committee, Almantas Galvanauskas, Duncan Steel, Paul Berman, Ted Norris, and Cagliyan Kurdak for taking the time to evaluate my research, and helping to make my thesis a better document.

Both past and present group members, with whom I enjoyed working, and had many useful discussions: Kaai-Hsui Liao, Kai-Chung (Richard) Hou, Guiqing (Noah) Chang, Chi-Hung Liu, Ming-Yuan Cheng, Matt Rever, Xiuquan Ma, Wei-Zung Chang, Shenghong Huang, Max, Caglar Yavuz, and Cheng Zhu.

In addition the friends and colleagues listed above I would like to thank Robert and Stephanie Post, Joe Turner, Chuck Divin, James Easter, Spencer Olson, and Rahul Mhaskar for their support and friendship.

Finally, I would like to thank my parents, James and Jill Swan, my sister, Michele Brown, and my grandmother Dorothy Johnson for their support and love, and without whom this work would not have been possible.

TABLE OF CONTENTS

LIST OF TABLES

Table

LIST OF FIGURES

Figure

CHAPTER I

Introduction

1.1 Introduction

Fiber technology has provided a path to practical high power, high-energy lasers and amplifiers with substantial advantages over their conventional solid state counterparts. The objective of this thesis is to expand the domain of this advantage to higher powers and energies, as well as to ultrafast time scales.

The first challenge, to increase capacity to handle high average and peak powers while maintaining beam quality and signal integrity arises from nonlinear effects that can shift the wavelength of the light or distort the pulse shape. The combination of long interaction length, and high intensity of the confined field result in a low threshold for nonlinear effects for a waveguide of small cross section. The resolution of this problem is to increase the cross section of the waveguide so that the intensity of the light is reduced below a critical value for non-linear effects. However, as the cross section is increased, modes other than the fundamental mode of the guiding structure become present, and this reduces the quality of the output beam from the laser.

Traditionally, to increase the waveguide cross section without degrading output beam quality, one of two approaches is taken. The most prevalent solution is to use

a large mode area (LMA) fiber which is a mildly multi-mode waveguide that can be operated so that factors other than the waveguide structure itself are responsible for higher order modes becoming lossy. The other alternative is to uses photonic crystal fibers (PCF) to create a very weakly guiding structure, so that only one mode propagates. The mode management techniques of the former strategy have practical limitations on the waveguide cross sectional area. The latter strategy is susceptible to mechanical disturbances that can allow light to leak from the guiding region, rendering the structure impractical as coiling is prohibited.

The solution to overcome these limitations is a waveguide structure that has been proposed and demonstrated [2], for which all higher order modes are intrinsically lossy, while the fundamental mode propagates through the structure with low loss. In this thesis, the first active examples of a such a mode selective fiber structure are demonstrated.

The second challenge, to establish a new paradigm for generating femtosecond pulses based on commercially available fibers and diodes, comes about due to the requirements of conventional mode-locked sources being incompatible with fiber technology. First, mode-locked oscillators require a very stable environment for operation, limiting their potential applications. Second, the large physical size of the oscillator and pump laser, as well as the high cost associated with each of these components, limit the range of applications for which they are suitable. Third, the limited tuning range of the repetition rate makes external pulse pickers necessary, and the lack of external control of pulse timing, necessitates the oscillator being the master clock for any experimental setup. Finally, the output beam requires free space coupling of the output pulse to a fiber system, reducing the overall robustness of any mode-locked seeded fiber based systems.

1.2 Fiber Technology Overview

Before discussing the challenges and solutions investigated in this thesis, an overview of current fiber technology is presented. The section begins with a historical overview, then proceeds to the basic system architecture, followed by the advantages of fiber lasers for high power applications. The section concludes with a discussion of ultra-fast technology, which is applicable to both fiber and conventional solid-state technology.

1.2.1 Historical Overview of Fiber Lasers and Amplifiers

Fiber laser technology has its roots in the earliest stages of laser development, with the first demonstration performed by Snitzer in 1961 [3], only a few years after the first demonstration of the laser. However, it wasn't until the first low loss rare earth doped fibers [4, 5] appeared in 1985 that research into fiber lasers began to take off.

The next wave of research in fiber technology was centered around the needs of the telecommunication industry to find suitable solutions for sending signals over long lengths of fiber, in order to make use of the high intrinsic bandwidth of near infrared light. With wavelengths centered around 1550 nm, a region of particularly low loss for silica glass based long haul fiber transmission of signals (i.e. trans-Atlantic) is readily achievable with minimal use of repeaters or other such devices. This intense research led to the development of a large infrastructure for fiber based systems, which has provided low cost and robust solutions for diverse applications and wavelengths.

The current generation of fiber based lasers and amplifiers have substantial advantages over their more conventional solid state counterparts (i.e. non waveguide

based gain media). For high power applications one of the most significant of these is the large surface area per unit volume of the fiber, helping to mitigate thermal issues intrinsic in high power systems such as thermal lensing. More generally, the elimination of free space coupling, a significant impediment to robust performance and reliability, can be realized by splicing the fibers together to create a monolithic system. Further, strong guidance of the light in the waveguide allows the fibers to be coiled, which along with the lack of free space coupling results in a compact laser system setup. Finally, the geometry of the fiber, which provides a relatively long interaction region for gain, along with efficient pump diodes result in an overall electrical to optical efficiency of up to 40 %. The totality of the above is a compact, reliable, robust and efficient system.

A current area of intense interest is the development of high power fiber laser systems, which can be used for a variety of applications including, material processing, cutting, welding, long distance free space communication, frequency conversion, as well as a source for the generation of extreme ultra-violet [6] and X-ray radiation [7]. High power systems are either configured as an oscillator or a master oscillator power amplifier (MOPA), and is the topic of the next section.

1.2.2 Basic Architecture for Fiber Based Lasers and Amplifiers

The current architecture of a fiber laser system has much in common with other types of oscillators and amplifiers, with a pump light source, a gain medium, and either a feedback mechanism for an oscillator, or seed signal for an amplifier. The distinguishing characteristics of fiber laser systems are the size, power scale and lack of free space coupling. In order to have these benefits along with good output beam quality, the fiber must possess several qualities. The fiber must guide the light

strongly enough that light does not leak when coiled. Guiding and core size must be such that mode management techniques such as coiling and single mode excitation can be used to remove higher order modes. Below, the two main configurations for fiber systems will be outlined.

Figure 1.1 shows a schematic diagram of an oscillator, the simplest fiber system, consisting of only a few components, a doped fiber as the gain medium, a pump, a pump coupler, and a feedback mechanism. The active region is most commonly formed by doping the fiber core with rare earth elements, also known as lanthanides, which when pumped at a suitable wavelength become inverted, creating gain. Diode lasers perform the pumping duties for fiber systems due to their high electrical to optical efficiency, and moderately high brightness, which allows the laser diode output to be coupled into a delivery fiber. The fiber coupled diode output is then spliced to a pump coupler, such as a wavelength division multiplexer, that couples the pump and signal into a common core that is then spliced to the active medium. The final step to form a laser cavity, introducing feedback, can be obtained from a variety of structures, the simplest of which is the Fresnel reflection from the straight cleaved fiber ends.

The second class of systems, master oscillator power amplifiers (MOPA), shown in Figure 1.2. MOPA is a multistage amplification scheme taking a small signal, frequently from a laser diode, and amplifying the signal through several stages to produce a large signal. This type of scheme is necessary as the gain from a single stage is insufficient to amplify a small signal to the desired powers. The gain medium, pump, and pump coupler as described above are also used for MOPA systems. The main difference in architecture between a laser and an amplifier is that a seed is injected from a seed laser into the MOPA stage, and feedback is eliminated from the

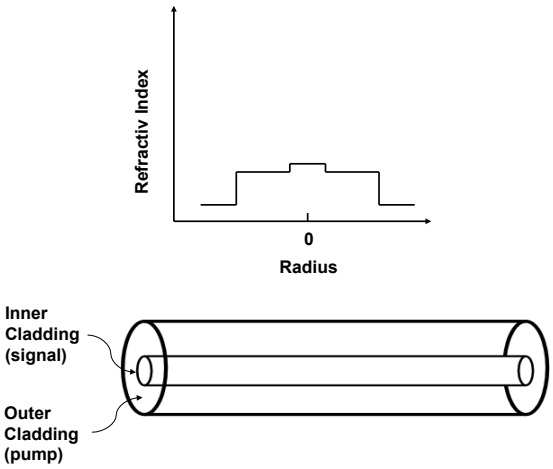

Figure 1.1: Schematic diagram of a double clad fiber

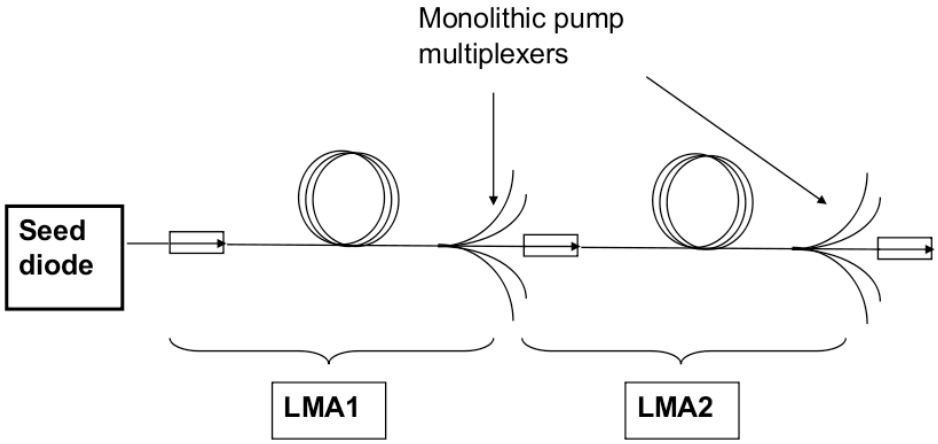

Figure 1.2: Schematic diagram of a master-oscillator-power-amplifier incorporating large mode area fiber (LMA)

system.

1.2.3 Fibers for High Power Laser Systems

For high power fiber systems, one of three effects can destroy or degrade the performance of the system. Thermal effects can distort the output beam profile. Nonlinearities can shift the wavelength of the signal, or distort the temporal profile of the pulse. And finally, for high enough pulse energies the glass substrate can be damaged. Below, I will briefly describe each of these effects and the commonly applied strategies for mitigation. However, it is in the area of nonlinearity mitigation that one of the central themes of this thesis lies.

Heat is introduced into the gain medium by non-radiative relaxation processes associated with pumping, and extracted at the surface. The efficiency of heat extraction increases as the ratio of the surface area to volume increases, which for fibers is substantially higher than that of conventional solid state lasers where for example the gain medium can be a rod. The ratio of the surface area to volume is given by

$$\frac{Surface\ Area}{Volume} = \frac{2}{r}. \tag{1.1}$$

With the transverse dimension of fibers used for power scaling around 500 μm, and for solid state rods on the order of centimeters, there is a substantial advantage for fibers for heat extraction.

Nonlinearities can arise from either the pump or signal. The threshold intensity is the intensity for a nonlinearity to have a substantial effect on the driving signal and of course depends on the mode field diameter in the fiber and hence the core size. The general strategy for power scaling is to increase the size of the guiding structure to reduce the intensity which enhances the capacity of the fiber to cary a given amount of power without deleterious effects.

Fiber lasers and amplifiers are most often end pumped, which for low power applications simply means that the signal and pump share a common guiding structure. However, for high power applications, which require large pumping powers, building a pump diode of sufficient brightness to efficiently couple the light into a small core structure is technically difficult.

In order to overcome this limitation, a double clad fiber structure, as shown in Figure 1.1, is constructed, which has a doped core for the signal, and a larger concentric or nearly concentric core for the pump. Though the double clad structure resolves the problem noted above, it is not without it's own problems. The primary difficulties are that the pump light is not as efficiently absorbed by the doped ions in the signal core due to reduced overlap between the pump and doped core, and that helical rays can propagate without interacting with the doped core. The problem created by reduced pump absorption is the need for longer active fiber lengths which results in a reduced nonlinear threshold for the the system. Both of these can be mitigated. Helical rays can be removed by modifying the outer cladding shape (i.e. octagonal shaped cladding) or the core can be eccentric. Pump overlap can be increased with the use of higher brightness diodes, which allow for smaller pump cladding dimensions.

For the signal, the strategy to delay the onset of nonlinearities is to increase the size of the core carrying the signal. There are several tradeoffs in doing this. The first is that increasing the core size can degrade the quality of the output beam as the structure moves from the domain of single transverse mode operation to multimode operation. External mode management techniques which reduce the content of higher order modes at the output of mildly multimode fiber are successful up to a core size of 20-25 μm. Beyond this limit, the ability to create monolithic systems

is compromised due perturbations at the splice point which scatter power into the higher order modes, which the external mode management techniques are unable to sufficiently remove, resulting in beam quality degradation. The goal of the fiber design demonstrated here is to produce the first active fiber structure with a core size larger than the limits imposed on the core size by splicing techniques, while maintaining single mode operation, which is the definition of an effectively single mode large mode area fiber.

1.2.4 Ultra-fast technology

Laser pulses shorter than one picosecond are referred to as ultra-fast or ultra-short pulses, and have been generated by a variety of methods [8, 9, 10, 11, 12, 13]. Mode-locked oscillators are the most common source of femtosecond pulses today. Kerr-lens mode locking, as used in titanium-sapphire oscillators relies on the kerr-lens effect [14, 15, 16, 17], which results in an intensity dependent change in the refractive index of the medium which leads to self focusing. With the Kerr-lens effect in the laser cavity, a more stable mode of operation can be achieved when the oscillator is mode-locked. Other mode-locking mechanisms, both passive and active, can be used to generate ultra-fast pulses as well. However, regardless of the mode locking mechanism or whether the gain medium is that of a conventional solid state laser or fiber laser, mode-locked cavities are not monolithic. Further, mode-locked oscillators require an interferometric alignment, which is very sensitive to perturbations, and is not robust.

The pulse energy that can be attained by amplifying femtosecond pulses is limited due to the high peak powers, which will generate parasitic nonlinear effects even for pulses with limited energy. That even low energy pulses can have high peak powers

can be seen by noting that for a gaussian pulse, the peak power is approximately given by $P_{peak} \approx E/T_{fwhm}$, where E is the pulse energy and T_{fwhm} is the full width at half maximum of the pulse. In order to overcome this limitation the pulses are stretched in a grating based stretcher [18, 19] or similar device by adding linear chirp, usually to the nanosecond regime resulting in roughly three orders of magnitude reduction in the peak power, and hence a three orders of magnitude greater pulse energy. After the pulse has been amplified, it is then compressed in a grating based compressor [20] by removing the linear chirp from the pulse, resulting in an amplified femtosecond pulse. The scheme of stretching the pulse, followed by amplification and then compression is known as chirped-pules-amplification (CPA) [21]. The components for a CPA system are the same for both conventional solid state lasers and fiber lasers, however in the latter case, multimode fibers have a special requirement. For high energy pulses, a large core fiber is used to facilitate higher pulse energies, however this comes at the expense of several modes being able to propagate. For a fiber, the higher order modes have a higher group velocity, and hence when higher order modes are present pre-puleses will be present as well, degrading the contrast of the pulse. In order to eliminate these, the techniques listed above can be used, however they suffer from limited robustness.

1.3 Thesis Overview

In the first part of this work, the development of a femtosecond seed source compatible with fiber technology is presented. The system starts from a gain-switched laser diode, which is followed by several stages of passive and active components to spectrally broaden and compress (temporally) the pulses. The system is based on telecom grade fiber technology, and can be monolithically integrated.

The second part of the thesis covers the design and demonstration of the first active effectively single mode fibers based on the chirally-coupled-core (CCC) fiber. CCC is an effectively single mode fiber [2] which produces single mode output without relying on external mode management techniques.

1.3.1 Mode-locking Free Femtosecond Technology

Femtosecond sources have a variety of uses, from machining and material processing, to investigating solid state materials and biomedical applications. However current femtosecond sources rely on mode-locking to generate femtosecond pulses, which has limited robustness and flexibility in operational parameters such as timing and repetition rate. These two attributes are due to the cavity length being fairly fixed and the sensitivity of the laser to mechanical disturbances. The system proposed and investigated can be constructed in such a manner that no free space alignments are necessary, and commercially available laser diodes, including the seed laser, can be used. These factors mitigate the traditional hinderances given above to more widespread deployment of femtosecond lasers.

The basic architecture, schematically shown in Figure 1.3, employs a laser diode to provide picosecond pulses followed by several stages of active and passive components where spectral broadening is to generate the desired femtosecond pulses. A similar strategy has been employed before using picosecond pulses from a solid state laser [22, 23] followed by nonlinear spectral broadening in fiber and then compression of the pulse by removal of the linear chirp. However, the performance of the system was limited by the spectral broadening and hence the temporal duration of the compressed pulse being dependent on both the duration and peak power of the pulses delivered from the solid state laser. The system outlined below uses two nonlinear

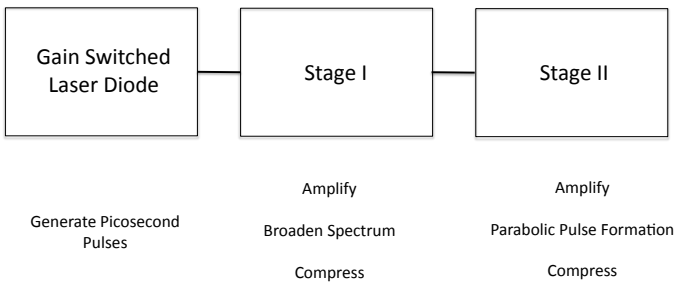

Figure 1.3: Schematic Diagram of the Pulse Compression Scheme

compression stages, the final one relying on parabolic pulse formation, where group velocity dispersion combines with nonlinear spectral broadening in a gain medium to generate stretched pulses whose spectral width, and hence the compression factor depend only on the energy of the pulse. This occurs provided the pulse energy and width fall within a reasonably wide range of parameters.

1.3.2 Effectively Single Mode Fibers

An effectively single mode fiber has a structure which removes higher order mode content from the central core. The effectively single mode structure used for the Yb-doped fibers for power scaling in the second half of this thesis is based on the novel chirally-coupled-core (CCC) structure. This structure consist of a large central core, with a side core helically spun about the central core. Without the CCC structure, the fiber would support several propagating modes modes.

For a pulsed fiber system, a fiber operating in several transverse modes, that is the fundamental mode plus all higher order modes, will generate a pre-pulse for

each higher order mode of the fiber due to each mode having its own group velocity. While for nanosecond systems, operation in the slightly multimode regime is not problematic due to the duration of the pulses being longer than the total delay due to intermodal dispersion, for a femtosecond system this is not the case, and multiple pre-pulses will be observed. This would be catastrophic for the femtosecond system, and thus the goal of having large core fibers to facilitate higher pulse energies, is directly at odds with the requirement that the amplifier be operated such that only one transverse mode exist. Thus, effectively single mode performance of an LMA fiber resolves the conundrum of single mode operation and large core fibers with the traditional positive attributes of fiber based systems. However, the overall goal of a robust and monolithic high power femtosecond system is beyond the scope of this thesis, though it is hoped that the accomplishments of thesis will lay some of the necessary foundations for such a system to be built in the future.

1.4 Thesis Structure

The development of a diode laser seeded, fiber based femtosecond source will be covered in the next chapter. To begin with the basic equations governing nonlinear effects in fibers will be discussed, followed by the limitations and requirements of the system imposed by parasitic as well as desirable nonlinear effects. With the system requirements set, and the basics of nonlinear optics in fiber based systems as needed for this work completed, the performance of laser diodes operated under fast modulation will be outlined. Finally the results obtained will be given and analyzed, and future work considered.

The topic of the fourth and fifth chapters is the development of the first active Chirally Coupled Core fibers. The current state of high power fiber laser technology

will be discussed along with current limitations and bottlenecks. The modal structure of fibers will be briefly reviewed, followed by coupled mode theory, and the basics of power scaling. Next, the numerical methods used to determine robust design of CCC fibers will be reviewed. With the background and supporting material covered, the results will be discussed.

The final chapter will conclude the thesis by reviewing the accomplishments of the previous chapters as well as looking at future directions.

CHAPTER II

Basics of Nonlinearities in Fibers and the Temporal Behavior of Gain Switched Laser Diodes

2.1 Introduction

A discussion of the basic physical phenomena relevant for the work is presented in this chapter. This includes nonlinear effects in fibers as well as the temporal behavior of laser diodes. In the first part of the thesis, pulses from Fabry-Perot laser diodes are compressed with nonlinear spectral broadening. Temporal compression makes use of self-phase-modulation (SPM), and is the only time where a nonlinear effect is beneficial in this work. Power scaling, as demonstrated in the second part of the thesis is accomplished by increasing the core size, which increases the nonlinear threshold that in turn facilitates higher powers and energy extraction from fiber based systems.

Nonlinear effects in fibers are governed by the nonlinear Schrödinger equation (NLSE). The NLSE governs SPM, and when gain is included parabolic pulse generation, both of which are employed in the first part of this work. Stimulated Raman and Brillouin scattering (SRS and SBS respectively) limit the amount of compression that can be achieved in the first part of the thesis, and limit the ultimate power extractable from a large core fiber as discussed in the second part of this work.

2.1.1 NLSE

The NLSE is the basic equation that governs nonlinear effects in fibers. The derivation begins with the wave equation,

$$\nabla^2\mathbf{E} - \frac{1}{c^2}\frac{\partial^2\mathbf{E}}{\partial^2 t} = \mu_o\frac{\partial^2\mathbf{P}_L}{\partial^2 t} + \mu_o\frac{\partial^2\mathbf{P}_{NL}}{\partial^2 t} \tag{2.1}$$

where $\mathbf{P}_L$ and $\mathbf{P}_{NL}$ are the linear and nonlinear polarizations respectively.

Further, by assuming that polarization is maintained along the fiber, and working in the frequency domain, the scaler wave equation for the slowly varying amplitude A is obtained,

$$\frac{\partial A}{\partial z} + \beta_1\frac{\partial A}{\partial t} + \frac{i\beta_2}{2}\frac{\partial^2 A}{\partial t^2} + \frac{\alpha}{2}A = i\gamma|A^2|A \tag{2.2}$$

where β_1 is the inverse of the group velocity, β_2 the group velocity dispersion (GVD), and α the measure of power loss in the fiber. The effective nonlinear parameter is defined as, $\gamma = n_2\omega_o/cA_{eff}$. where n_2, the nonlinear-index coefficient, is a property of the material, A_{eff} the effective area of the core (modal area), ω_o the frequency of light, and c the speed of light. β_1 and β_2 are the taylor coefficients of an expansion of $\beta = n(\omega)\omega/c$ about the central frequency of the pulse ω_o, so that $\beta_j = \partial^j\beta/\partial\omega^j$. Next, the equation is put in a form using a normalized amplitude U, defined as $A(z,\tau) = \sqrt{P_o}exp(-\alpha z/2)U(z,\tau)$, with τ a time normalized by the initial pulse width T_o and moving with the group velocity v_g, so $\tau = T/T_o = (t - z/v_g)/T_o$. Thus

$$i\frac{\partial U}{\partial z} = \frac{1}{2L_D}\frac{\partial^2 U}{\partial\tau^2} - \frac{exp(-\alpha z)}{L_{NL}}|U|^2U \tag{2.3}$$

is obtained, with the linear dispersion length, L_D, and the nonlinear length, L_{NL}, defined as

$$L_D = \frac{T_o^2}{\beta_2} \quad ; \quad L_{NL} = \frac{1}{\gamma P_o}. \tag{2.4}$$

These two length scales determine which effects will dominate, and three cases exist: $L_D \gg L > L_{NL}$ where only nonlinear effects need to be considered, $L_{NL} \gg L > L_D$ where GVD will dominate, and if $L \gg L_D \approx L_{NL}$ both GVD and nonlinear effects need to be considered. The NLSE in either the form of equation 2.2 or 2.3 will be the starting point for understanding the nonlinear effects outlined below.

2.1.2 Self Phase Modulation

Self Phase Modulation (SPM) generates spectral broadening and can be used to compress a pulse. To begin with, the simplified case of negligible GVD yields,

$$\frac{\partial U}{\partial z} = i\frac{exp(-\alpha z)}{L_{NL}}|U|^2 U \tag{2.5}$$

from equation 2.3. Equation 2.5 can be solved by substituting $U = Vexp(i\Phi_{NL})$ and equating the real and imaginary parts, the general solution being,

$$U(L,T) = U(0,T)exp(i\Phi_{NL}(L,T)) \tag{2.6}$$

with $U(0,T)$ the input pulse, $\Phi_{NL} = |U(0,T)|^2 L_{eff}/L_{NL}$ the nonlinear phase, and L_{eff} defined as the effective length of the fiber $L_{eff} = (1 - exp(-\alpha L))/\alpha$. To determine the amount of broadening generated by SPM, we need to consider the instantaneous frequency of the pulse.

$$\delta\omega(T) = -\frac{\partial \Phi_{NL}}{\partial T} = -(L_{eff}/L_{NL})\frac{\partial |U(0,T)|^2}{\partial T} \tag{2.7}$$

This equation describes the new frequencies generated by SPM. The maximum amount of broadening occurs when $\delta\omega(T)$ has its largest value, and this occurs at T = 0, giving

$$\delta\omega_{max} = 0.86\frac{\Phi_{max}}{T_o} = 0.86\frac{\gamma P_o L_{eff}}{T_o}. \tag{2.8}$$

The numerical factor actually varies depending on the initial pulse shape, but has a value near 0.86 for smoothly varying pulses such as gaussian and hyperbolic secant

pulses. Also from equation 2.7 it can be seen that a pulse broadened from SPM is chirped. The chirp across the central portion of the pulse will vary in a linear fashion if the pulse emitted from the diode has a smooth temporal profile.

2.1.3 Parabolic Pulse Formation

Parabolic pulse formation transforms the input pulse from its initial temporal profile to a parabola, through an interplay of spectral and temporal broadening with gain. Parabolic pulse formation will only occur if the input pulse duration is sufficiently short, and the energy is within a suitable range. These requirements along with the characteristics of the output pulse are determined below.

To begin with, a solution to the NLSE with gain, $g\psi/2$,

$$i\frac{\partial\psi}{\partial z} = \frac{\beta_2}{2}\frac{\partial^2\psi}{\partial T^2} - \gamma|\psi|^2\psi + \frac{g}{2}\psi \tag{2.9}$$

is required. Equation 2.9 can be solved numerically, an analytical solution can be found for a limiting case. The outline of the solution to the above equation given here follows that given in [1]. Equation 2.9 is valid when the gain can be considered constant across the spectrum of the pulse and is unsaturated. The energy of the pulse, $U(z) = \int_{-\infty}^{\infty}|\psi(z,T)|^2dT$, follows the conservation equation $U(z) = U(0)\ exp(gz)$, which acts as a constraint on the solution.

To begin, the slowly varying amplitude will be expressed as a positive definite amplitude and phase, and has the form $\psi(z,T) = A(z,T)\ exp[i\Phi(z,T)]$, which after substitution in equation 2.9 yields the following coupled equations

$$\frac{\partial A}{\partial z} = \beta_2\frac{\partial A}{\partial T}\frac{\partial\Phi}{\partial T} + \frac{\beta_2}{2}A\frac{\partial^2\Phi}{\partial T^2} - \frac{g}{2}A \tag{2.10}$$

$$\left[\frac{\beta_2}{2}\left(\frac{\partial\Phi}{\partial T}\right)^2 - \frac{\partial\Phi}{\partial T}\right]A = \frac{\beta_2}{2}\frac{\partial^2 A}{\partial T^2} - \gamma A^3. \tag{2.11}$$

The method of solution presumes self-similar evolution in the fiber, and this results in a reduction in the number of degrees of freedom in the problem by using a self similarity variable ζ. The general form of the solution is

$$A(z,T) = f(z)F(z,T) = f(z)F(\zeta), \tag{2.12}$$

$$\Phi(z,T) = \phi(z) + C(z)T^2 \tag{2.13}$$

with ζ defined as

$$\zeta = f^2(z)exp(-gz)T. \tag{2.14}$$

C(z) is the coefficient of linear chirp, and $F(\zeta)$ describes the temporal profile. Substituting 2.12 and 2.13 into 2.10 and 2.11 yields

$$\frac{\partial f}{\partial z} = \beta_2 C f + \frac{g}{2} f \tag{2.15}$$

$$\left(2\beta_2 c^2 - \frac{dC}{dz}\right)\frac{1}{f^6}exp(2gz)\zeta^2 - \frac{1}{f^2}\frac{d\phi}{dz} = \\ = \frac{\beta_2}{2}\frac{f^2}{F}\frac{\partial^2 F}{\partial \zeta^2}exp(-2gz) - \gamma F^2. \tag{2.16}$$

An analytical solution of equations 2.15 and 2.16 can be found in the asymptotic limit $z \to \infty$, for which the term proportional to $\partial^2 F/\partial\zeta^2$ can be neglected. After taking the limit on equation 2.16, it can be split into two coupled equations

$$\left(2\beta_2 c^2 - \frac{dC}{dz}\right)\frac{1}{f^6}exp(2gz) = a\gamma \tag{2.17}$$

$$\frac{1}{f^2}\frac{d\phi}{dz} = \gamma \tag{2.18}$$

where $F(\zeta) = \sqrt{1 - a\zeta^2}$ for $|\zeta| \leq a^{-1/2}$. The solution for the coupled equations 2.15, 2.17 and 2.18 are

$$A(z,T) = \begin{cases} A_o exp\left(\frac{g}{3}z\right)\left[1 - \frac{T^2}{T_p(z)^2}\right] & , \quad |T| \leq |T_p(z)| \\ 0 & , \quad |T| > |T_p(z)| \end{cases} \tag{2.19}$$

and

$$\Phi(z,T) = \Phi_o + \frac{3\gamma A_o^2}{2g} exp(\frac{2}{3}gz) - \frac{g}{6\beta_2}T^2 \tag{2.20}$$

where

$$T_p(z) = \frac{6A_o\sqrt{\gamma\beta_2/2}}{g} exp\left(\frac{g}{3}z\right) \tag{2.21}$$

and

$$A_o = \frac{1}{2}\left(\frac{gU_{in}}{\sqrt{\gamma\beta_2/2}}\right)^{1/3}. \tag{2.22}$$

Further, the Fourier transform of the solution yields the spectral profile

$$A(z,T) = \begin{cases} |\Psi(z,\omega)|^2 = \frac{3|\beta_2|A_o^2}{g} exp\left(\frac{2}{3}gz\right)\left(1 - \frac{\omega^2}{\omega_p^2(z)}\right) & , \quad |\omega| \leq |\omega_p(z)| \\ 0 & , \quad |\omega| > |\omega_p(z)| \end{cases} \tag{2.23}$$

$$\omega_p(z) = \sqrt{\frac{2\gamma}{\beta_2}} A_o exp\left(\frac{2}{3}gz\right). \tag{2.24}$$

The key feature of the solution is that the spectral width depends on the input energy alone, hence the compression factor will be insensitive to fluctuations of T_o or P_o. Further, the chirp is found to be $\partial\Phi/\partial T = gT/3\beta_2$, which is linear, and therefore easily compressed by a grating pair or chirped fiber bragg grating (FBG).

The analytic solutions were shown to agree with numerical evaluations of equation 2.9 by plotting the evolution of the temporal profile of both the numerical result and the analytical solution (i.e. $T_p(z)$) as a function of distance as shown in Figure 2.1 [1]. Here it can be seen that the temporal width of both solutions follow the values predicted by the analytical solution after a sufficient distance.

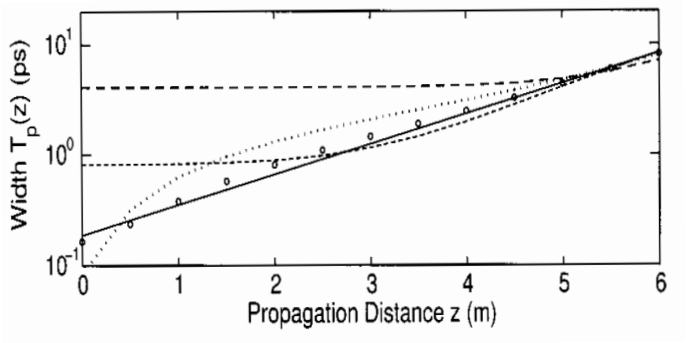

Figure 2.1: Numerical Simulations of Pulses Converging to a Parabola (solid line) [taken from [1], Opt. Lett.]

2.1.4 SRS and SBS

Next considered are SRS and SBS which generate new optical frequencies at the sum and difference of the laser (pump) frequency, ω_p, and phonon frequency, Ω_j (j = R for Raman and B for Brillouin), the former known as the anti-stokes wave, and the latter the stokes wave. The stokes wave, $\omega_s = \omega_p - \Omega_j$, is the destruction of the laser photon and the creation of a new photon of lower energy along with a phonon, while the anti-stokes wave, $\omega_a = \omega_p + \Omega_j$, is the generation of a new photon of higher energy from a pump photon and a substrate phonon. The transfer of energy from the pump to the stokes field occurs quickly once a threshold level is reached, and it is this value that must be calculated and below which the pump power level must stay if SRS and SBS are to be avoided.

Beginning with SRS, the following two equations are valid in the cw and quasi-cw ($T_{FWHM} \geq 100ps$) regime,

$$\frac{dI_s}{dz} = g_r I_p I_s - \alpha_s I_s \tag{2.25}$$

$$\frac{dI_p}{dz} = -\frac{\omega_p}{\omega_s} g_r I_p I_s - \alpha_p I_p \tag{2.26}$$

where I_p and I_s are the intensities of the pump and stokes field respectively, g_r is the raman gain, and α_p and α_s are measures of power loss in the fiber at the pump and stokes wave respectively. The initial intensity of the stokes wave, I_s, is small, and thus the first term of equation 2.25 can be neglected which allows it to be integrated and the result substituted in equation 2.26 yielding

$$I_s(L) = I_s(0) exp(g_r I_o L_{eff} - \alpha_s L), \tag{2.27}$$

where L is the fiber length, and L_{eff} the effective length, and is either defined as $[1-exp(-\alpha_p L)]/\alpha_p]$ or $T_{FWHM}/(v_{gp}^{-1} - v_{gs}^{-1})$, where v_{gp} and v_{gs} are the group velocities of the pump and stokes waves respectively. L_{eff} is taken to be the smaller of the two, the first choice being when absorption limits the penetration depth of the pump, and the latter the length when the pump and stokes pulses no longer sufficiently overlap due to a difference in the group velocities of the pump and stokes waves. Multiplying equation 2.27 by $\hbar\omega$ and integrating over the range of Raman gain yields

$$P_s(L) = P_s^{eff}(0) exp(g_R(\omega_p - \omega_s) I_o L_{eff} - \alpha_s L) \tag{2.28}$$

where $P_s^{eff}(0) = \hbar\omega_s B_{eff}$ and B_{eff} is the effective bandwidth of the stokes radiation. Now, using the threshold condition that the power of the stokes radiation equals that of the pump at the output of the fiber (L) generates the threshold condition for the critical power [24] P_o^{cr}

$$\frac{g_r P_o^{cr} L_{eff}}{A_{eff}} = 16 \tag{2.29}$$

where A_{eff} is the effective mode area of the fiber. The threshold condition for SBS can be obtained starting with equations similar to equations 9 and 10, where the raman gain g_r, is replaced by the Brillouin gain g_b and the ratio $-\omega_p/\omega_s$ is replaced

+1, the sign change being due to the stokes radiation for SBS propagating in the backward direction, and ω_p/ω_s is replaced by one as ω_s and ω_p are approximately equal for SBS. The threshold condition for SBS is then

$$\frac{g_b P_o^{cr} L_{eff}}{A_{eff}} = 21 \tag{2.30}$$

The Brillouin gain is attenuated for spectrally broad pulses according to

$$g_b(\Delta\nu_p, \Delta\nu_b) = g_b \frac{1}{1 + \frac{\Delta\nu_p}{\Delta\nu_b}} \tag{2.31}$$

with $\Delta\nu_p$ and $\Delta\nu_b$ the spectral width of the pump pulse, and brilloun gain repectivley, with g_b the Brillouin gain in the limit of long pulses.

For the second stage the pulses in the fiber will be shorter than 100 ps, and the quasi-cw approximation is not valid. It is thus necessary to consider the coupled NLSE that includes both gain, cross phase modulation (XPM) and the Raman response function ($R_j(z,t)$ where j is either p for pump or s for the stokes fields).

$$\frac{\partial A_p}{\partial z} + \beta_1 \frac{\partial A_p}{\partial t} + \frac{i\beta_2}{2}\frac{\partial^2 A_p}{\partial t^2} = \frac{g}{2}A_p + i\gamma_p(1 - f_R)(|A_p^2|A_p + 2|A_s^2|A_p) + R_p(z,t) \tag{2.32}$$

$$\frac{\partial A_s}{\partial z} + \beta_1 \frac{\partial A_s}{\partial t} + \frac{i\beta_2}{2}\frac{\partial^2 A_s}{\partial t^2} = \frac{g}{2}A_s + i\gamma_s(1 - f_R)(|A_s^2|A_s + 2|A_p^2|A_s) + R_s(z,t) \tag{2.33}$$

The XPM terms ($2|A_s^2|A_p$ and $2|A_p^2|A_s$) are similar to SPM, but the change in refractive index is due to another field. Analytic solutions are not generally available, and so numerical solutions will need to be evaluated. Evaluation of the numerical solution will assume that the term proportional to $|A_s|^2$ in equation 2.32 can be neglected, and that $R_j(z,t)$ is constant for pulses longer than 1 ps.

2.2 Temporal Behaviour of a Laser Diode

Direct modulation of the of output pulses of a laser diode by modulation of the driving current makes them an attractive choice for many applications, as well as a seed sources for master oscillator power amplifier (MOPA) systems. For pulses in the sub one hundred picosecond regime however, the dynamics of the material system are of the same order of magnitude as the current pulses, hence it becomes necessary to investigate the dynamics of the pulsed laser diode in order to gain insight into the behavior of the laser output. The equations governing the behavior of the semiconductor laser are similar to that of conventional lasers, with the exception that the time constants for decay rates are of a shorter time scale than for typical solid state lasers such as Nd:YAG. The coupled equations governing this behavior are

$$\frac{dn_e}{dt} = \frac{J}{ed} - \frac{n_e}{\tau_{sp}} - \frac{c}{\eta n_g} gS \tag{2.34}$$

$$\frac{dS}{dt} = \frac{\gamma}{\tau_{sp}} Dn_e + \frac{c}{n_g}(g - \alpha)S \tag{2.35}$$

where

$$g = \eta \frac{n_g}{c} A(Dn_e - \hat{n}_o) \tag{2.36}$$

with the constants and variables as defined in Table 2.2. The behavior of the carriers, photons, and gain are governed by 2.34, 2.35, and 2.36 respectively. The three terms on the right hand side of 2.34 describe the injected carriers, the recombination of carriers by spontaneous emission, and either stimulated emission or absorption respectively. Equation 2.35 governs the photon behavior, with the terms on the

Symbol	Parameter	Numerical Value	unit
S	photon density		um^{-2}
n_e	electron density		um^{-2}
g	gain		μm^{-1}
J	current density		$\frac{A}{um^2}$
e	electron charge	1.6×10^{-19}	C
d	thickness of active laser region	0.3	μm
L	laser cavity length	250	μm
λ_o	central wavelength	1.3	μm
τ_{sp}	spontaneous electron lifetime	2×10^{-9}	s
τ_{ph}	spontaneous electron lifetime	2×10^{-9}	s
η	mode confinement factor	0.5	
n_g	group index of laser medium	4	
γ	spontaneous emission factor	3.9×10^{-3}	
α	loss coefficient	20×10^{-4}	μm
$\hat{n}_o$	transparency constant	2.2×10^{-3}	μm^{-3}
D	line shape factor	280	

Table 2.1: Parameters for 1.3 um laser diode

right hand side being spontaneous and stimulated emission respectively. The final equation 2.36 gives the gain, and it appears in the third and second terms of equations 2.34 and 2.35 respectively, which are the nonlinear terms which couple the equations.

To better understand the above equations, numerical solutions obtained using a fifth order embedded Runge-Kutta method were investigated for different driving current profiles for a 1.3 μm, 250 μm cavity AlGaAs fabr perot laser diode with the constants as given in Table 2.2. To start, we begin by looking at the turn on period when a constant current is applied as shown in Figure 2.2. The characteristic features of diode behavior during the turn on period as shown in Figure 2.2 are a turn on delay after the bias is initially applied, and oscillation of the output intensity and number density. The more important of these two features is the oscillation of the output intensity due to the number density rising above the equilibrium value, followed by a large increase in the output intensity to a value above its equilibrium value, which in turn results in depletion of the carriers below threshold, followed by a reduction

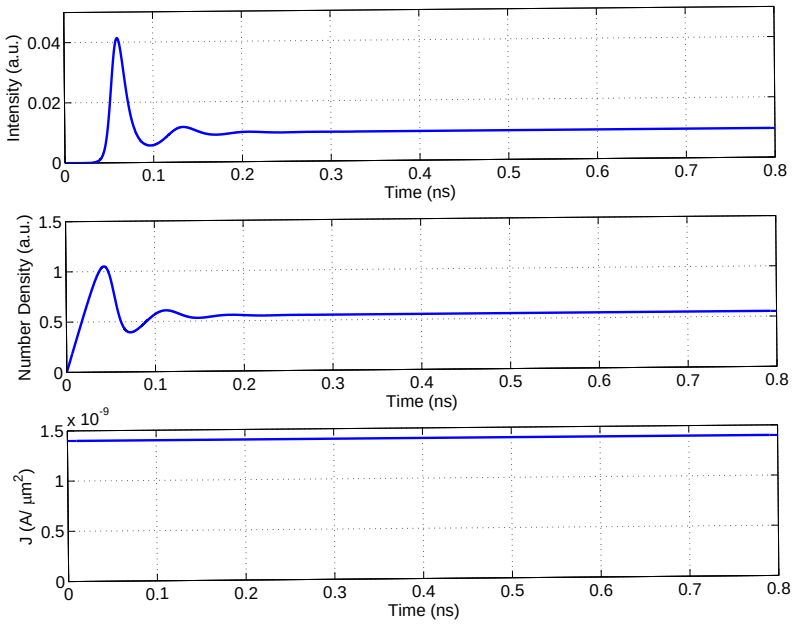

Figure 2.2: Numerical Solutions of a Laser Diode Driven far Above Threshold During the Turn on Period with a Constant Bias Applied. Output Intensity (Top). Number Density (Middle). Driving Current Density (Bottom)

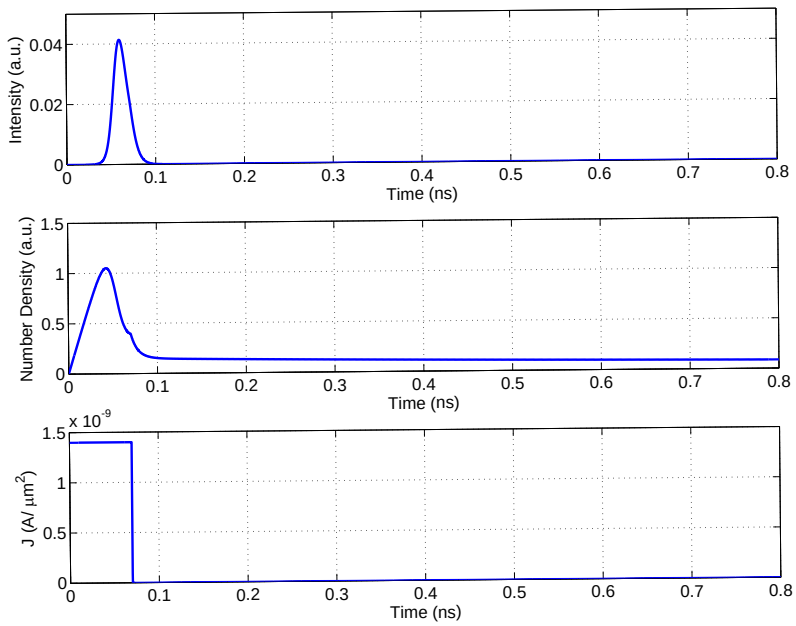

Figure 2.3: Numerical Solutions of a Laser Diode Driven far Above Threshold During the Turn on Period with 70 ps Impulse Bias Applied. Output Intensity (Top). Number Density (Middle). Driving Current Density (Bottom)

in the output intensity. With the output intensity low, the carrier number density begins to build again, and the process starts anew, albeit with lesser amplitude than the previous oscillation. This shows the behavior of damped oscillations, which for the values chosen for these simulations are highly damped. These features are always present during the turn on period of a laser diode, and are exploited to enable the generation of pulses on the order of tens of picoseconds by current modulation rather than through a mode locking mechanism.

Figure 2.3 shows the result of a 70 ps impulse current applied to the 1.3 μm laser diode, which is of a suitable duration to allow only a single oscillation to occur. The output pulse is 19.7 ps in full width half max duration (fwhm). This is an idealized case, where the capacitance and inductance of the laser diode packaging have been completely neglected. As we will see below, including these effects substantially

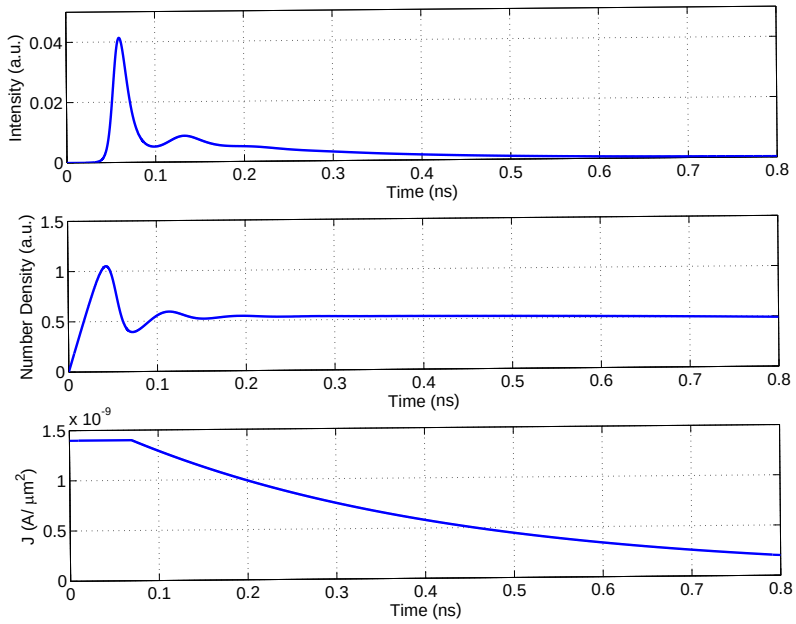

Figure 2.4: Numerical Solutions of a Laser Diode Driven far Above Threshold During the Turn on Period 70 ps Impulse Bias Applied Followed by Exponential Decay. Output Intensity (Top). Number Density (Middle). Driving Current Density (Bottom)

distorts the output optical pulses, due to the current to the laser diode not returning to zero immediately after the driving source shuts off.

The final figure in this series, Figure 2.4, shows the result of a sharp rising impulse bias, followed by exponential decay of the current, which is more realistic than the impulse current shown in the previous figure as physical devices will have some inductance and capacitance associated with it from the bonding of metal leads to the semiconductor, as well as from the case enclosing the laser diode. The result of the exponential decay of the injected current is a slow decay of the carriers after the initial oscillation which in turn results in the slow decay of the output intensity, and this can carry a substantial portion of the total pulse energy, as is evident in the figure.

With the background material covered the experimental design and results will

now be covered in the next chapter.

CHAPTER III

Mode-locking free femtosecond technology: parabolic pulse compression from 100-ps to 100-fs

3.1 IHistorical Overview of Femtosecond Technology and Introduction to Mode-Locking Free Femtosecond Technology

The generation of 100 – 200 fs pulses by nonlinear compression techniques starting from 10 - 100 ps gain switched pulses generated by standard diode lasers at 1.06 μm has been investigated. The technological attractiveness of this is that it would enable the design of a novel, robust, compact, non-mode-locked source to meet the needs of a variety of applications (such as material processing and characterization, biomed, etc.). The elements that have been used during this investigation are all readily available diodes and fibers, which will allow the system to be constructed without the use of expensive or difficult to manufacture specialty components, whether that be fibers or diodes.

The strategy for generating femtosecond pulses is based on a concept of parabolic pulse formation in positive dispersion fibers with gain [1, 25, 26, 27, 28]. Since parabolic pulse formation is completely determined by fiber amplifier parameters (gain, dispersion, effective nonlinearity coefficient) rather than input pulse parameters, the end result is insensitive to the input pulse shape and duration. This is in principle different from diode-compression using soliton-compression techniques

[24], in which short initial pulses are necessary and complex multistage compression arrangements with significant fiber lengths (from 100s of meter to kilometers) are required.

Previous parabolic pulse compression used relatively short ($<$ 5ps) optical seed pulses. The main limitation for generating parabolic pulses from longer (10 – 100 ps) pulses is the onset of Raman scattering before parabolic pulse formation occurs Another issue arises from the non-coherent multimode nature of currently available Fabry-Perot gain-switched diode lasers. The solution to the first problem is a dual-stage nonlinear compression scheme. The first stage amplifies the seed signal to generate self phase modulation (SPM) spectrally broadened pulses. The pulses are then compressed to less than 5 ps, so that they can seed the second stage where spectral broadening by parabolic pulse formation is used to further compress the pulses to the desired 100-200 fs pulses. The second problem is not due to a fundamental limit, but a lack of commercially available diodes with suitable performance at 1.06 μm and so wavelength locking of the pulsed seed diode through injection seeding is necessary.

The compression techniques used in both stages rely on nonlinear effects. The first stage uses SPM, which generates spectral broadening accompanied by positive linear chirp (leading edge of the pulse is red shifted and the trailing edge blue shifted with respect the central wavelength of the pulse ω_o). A compressor is used to generate near bandwidth-limited compressed pulses. For simplicity, a grating based compressor was used, however a chirped fiber Bragg grating (CFBG) can replace this bulky free space component to create a monolithic system. The second stage uses parabolic pulse formation, where three effects, gain, spectral broadening, and temporal elongation from group velocity dispersion (GVD) combine to generate pulses that can

be compressed by a grating pair or a CFBG to the desired femtosecond pulses.

The solution to the second problem, injection seeding, involves a pair of diodes, one gain switched and the other continuous wave (cw), or quasi-cw. The cw diode is aligned into the cavity of the gain switched diode, which allows the gain switched pulse to build up from the injected signal rather than noise in the laser cavity. The result is a single mode being emitted from the pulsed diode.

The idea to generate femtosecond pulses from picosecond pulses is not new, and work in the 1980's towards this end was undertaken [22, 23]. This earlier work used pulses from a Q-switched or mode-locked Nd:YAG laser that were then coupled into a fiber where spectral broadening via SPM occurred, and the output pulses compressed by a grating pair. There are several limitations on the pulses produced by this method. The shape of the input pulse affects the quality of the output pulse, and the amount of spectral broadening from SPM depends on the peak power of the input pulse, with greater broadening, and thus compression, for higher peak powers. As the output from a Nd:YAG laser has both peak power and temporal width fluctuations the compression factor of the output pulses fluctuate, resulting in a noisy pulse train. Further, the maximum compression of the pulse is limited by the threshold value for stimulated Raman scattering (SRS) to around 700 fs, or a compression factor near 100, for a single stage system starting with 10-100 ps pulses. SRS is an energy exchange between the optical field and an optical phonon of the fiber substrate that results in a frequency shift of the optical field. If frequency shifted components are generated, they will interact with the original frequency components through cross phase modulation (XPM) resulting in a pulse that is not linearly chirped. As the chirp is not linear, the pulse cannot be compressed by a simple grating pair. Efforts at producing femtosecond pulses in this manner were

abandoned with the advent of the Ti:Sapphire Kerr-lens mode-locked oscillators [14] which had both shorter pulses and greater stability.

In the two decades since the Nd:YAG experiments, substantial advancements in fiber laser technology have occurred. These include the advent of fiber-bragg-grating stabilized high power (∼600 mW) single mode fiber pigtailed pump laser diodes, pulsed laser diodes, Yb-doped amplifier fibers, and CFBG that allow another take on spectral broadening of long pulses to create femtosecond pulses. This system will be a large step forward from the large and delicate Nd:YAG based systems of the past.

The first stage of the system will face the same stability problems as the Nd:YAG system. However, the compression achieved in the second stage is primarily dependent on the pulse energy and so is relatively insensitive to peak intensity or pulse width fluctuations. Further the onset of SRS is delayed because the energy and temporal width of the pulse simultaneously increase.

In addition to resolving the problems of the Nd:YAG based systems of the past, several shortcomings of the mode-locked lasers currently used to generate femtosecond pulses are addressed. Mode-locking operates by pumping the gain medium with cw light, where a pulsed mode of operation of the cavity occurs that is more stable than cw operation. For the case of Ti:sapphire oscillators, Kerr-lens mode-locking is used. At sufficiently high powers, the refractive index of the gain medium depends on the intensity, which leads to self focusing, and this is known as the Kerr-lens effect. For a Ti:sapphire oscillator, the most stable mode of operation at high intensity is a pulsed mode of operation, and the oscillator is said to be mode-locked. Due to the large bandwidth of the gain medium, the resultant pulses can be as short as a few femtoseconds. Whether the mode-locking mechanism is based on the Kerr-lens

effect, or another phenomena, a high degree of stability is required to maintain the interferometric alignment required for mode locking. As such the oscillator is not robust. Further mode-locking requires a fairly fixed cavity length for mode-locked operation to be achieved, and as such the repetition rate of the oscillator is nearly fixed. The lower stability requirements and robustness of the proposed system are attributable to the fact that the seed is from a diode laser, and that an all fiber, and therefore monolithic, system is possible. Lastly, the repetition rate of the system can be chosen within the operating parameters of the diode laser, and so a wide range of repetition rates are available from a single source.

The remainder of the chapter will be organized as follows. First the basic equations governing nonlinear effects in fibers will be presented. Second, stages one and two will be described in detail, with stage two outlined first, as it determines the requirements of stage one. Third, the transient behavior a laser diode will be detailed, and the finally experimental results will be examined and analyzed, and future work discussed.

3.2 Mode-Locking Free Femtosecond Design

The primary limit on parabolic pulse formation from long pulses (10–100 ps) is Raman scattering. In order to overcome this limitation, a dual stage non-linear compression scheme will be used. The first stage amplifies the diode seed signal in order to generate short pulses using spectral broadening from SPM. The spectrally broadened pulses are then compressed to below 5 ps using a grating based compressor. The second stage uses parabolic pulse compression, where an interplay between spectral broadening, gain, and temporal elongation generate a linearly chirped parabolic output pulse that is then compressed to generate the desired 100–200 fs pulses. As the

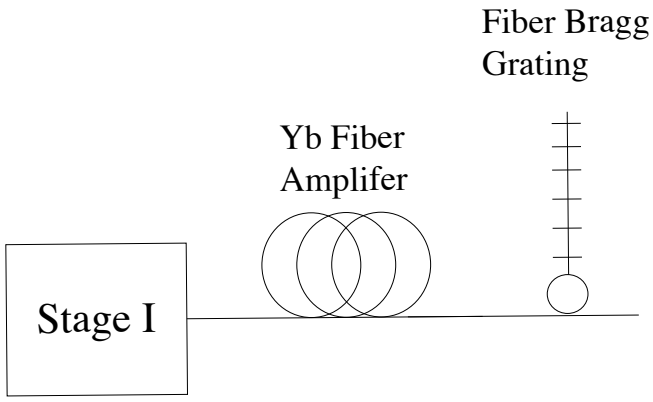

Figure 3.1: Schematic of Stage II

second stage sets the requirements of the first stage, stage II will be detailed first.

3.2.1 Stage II

The second stage, shown in Figure 3.1, consist of a fiber amplifier followed by a linear compressor. This stage transforms the input pulse into a parabola, provided the input pulse duration is sufficiently short, and the energy within a suitable range. The pulse is then compressed to achieve the desired 100-200 fs pulses. This will first be done using a conventional grating pair compressor in order to determine the required amount of negative linear chirp. After the required negative linear chirp is known, a fiber-bragg-grating with this chirp may be substituted for the grating pair compressor, thus enabling a monolithic system. Below, the necessary fiber length, gain, and input pulse parameters, as well as the characteristics of the output pulse are determined.

The analytic solutions for parabolic pulse formation found earlier are primarily useful in that they show the evolution toward a parabolic profile primarily depends on

the pulse energy rather than duration. Unfortunately, little information regarding the energy and temporal width of the input pulse, or the gain and length of the amplifier fiber required to enter the parabolic regime are available in an analytic form, and so we must resort to numerical solution of equation 2.9 in order to determine the necessary length of fiber. Results of these simulations using $\gamma = 4.3\ m^{-1}W^{-1}$ and $\beta_2 = 26\ ps^2/m$ indicate that a 25 m fiber with gain between 20-30 dB is sufficient to generate a pulse with a parabolic temporal profile, and more importantly, a positive linear chirp across the entire pulse. The linear chirp is crucial as it allows the pulse to be compressed with either a grating pair or a linearly chirped fiber-bragg-grating.

Having found the minimum fiber length for parabolic pulse formation, it is now necessary to determine the maximum input and output energies, as well as the maximum allowable length of fiber. There are two limits set on the output energy, the onset of SRS, or the failure of the condition that gain is constant across the entire spectrum of the pulse ($\Delta\omega \not\leq \Delta\omega_g$). Either of these two conditions result in a chirp that is not linear, and thus the pulse cannot be easily compressed (i.e. by removing only the linear chirp of the pulse). First the limit set by the finite gain bandwidth on the input and output energy will be determined. The limiting input energy will then be shown to converge to the parabolic regime (i.e. 25 m of Fiber) before the onset of Raman.

To determine the gain bandwidth limit, the total spectral width ($2\omega_p(z)$) as a function of output energy can be found using equations 2.22 and 2.24 and set equal the amplifier gain bandwidth. Gain is uniform across 30–35 nm for currently available Yb doped fiber amplifiers. Taking 30 nm, to be conservitive, and using $\beta_2 = 26ps^2/m$ and $\gamma = 4.3 \times 10^{-3}\ m^{-1}W^{-1}$, the gain bandwidth limit is found to be 21 nJ. The fiber amplifier has a gain of 25 dB, and so the input energy can not be above 66 pJ.

Using an input energy of 66 pJ the maximum length of fiber permitted by Raman can be found by numerically solving equations 2.32 and 2.33 as indicated in section 2.4. The Raman threshold here is taken as

$$P_s(L) = \kappa P_o exp(\alpha L) \tag{3.1}$$

where κ is some small fraction. The low threshold set here (small value of κ) is to ensure that the pulse will have only linear chirp, and hence can be compressible by a linearly chirped FBG. A graphical solution of this form, with $\kappa = 10^{-4}$ is shown in Figure 3.2. From this plot it is clear that the pulse will enter the parabolic regime (i.e travel at least 25 m) before the onset of Raman. Further the input pulse duration can be at most 6 ps in order to converge to the parabolic solution before the onset of Raman, and below 5 ps if it is to do so before the end of the fiber (i.e. at 25 m).

With the input pulse parameters determined to be 66 pJ, fwhm < 5 ps, and the fiber amplifier 25 m with a gain of 1 dB/m, the duration of the compressed output pulse is found to be 140 fs (FWHM) by removing the linear chirp of the asymptotic solution.

3.2.2 Stage I

With the necessary input pulse parameters of stage II determined, the design of the first stage to meet those requirements can now be determined. The stage begins with a seed pulse (60-100 ps) from a gain switched Fabry-Perot laser diode (FPLD) that is injection locked by seeding from a cw wavelength stabilized FPLD. Following the diode are an isolator that protects the diode from amplified spontaneous emission and then a 10 m Yb doped fiber amplifier capable 20 - 27 dB of gain. Next, the pulse will enter a small core fiber (MFD 6.2 μm) where spectral broadening will occur. Finally, before the pulse enters the second stage, it will be compressed by a

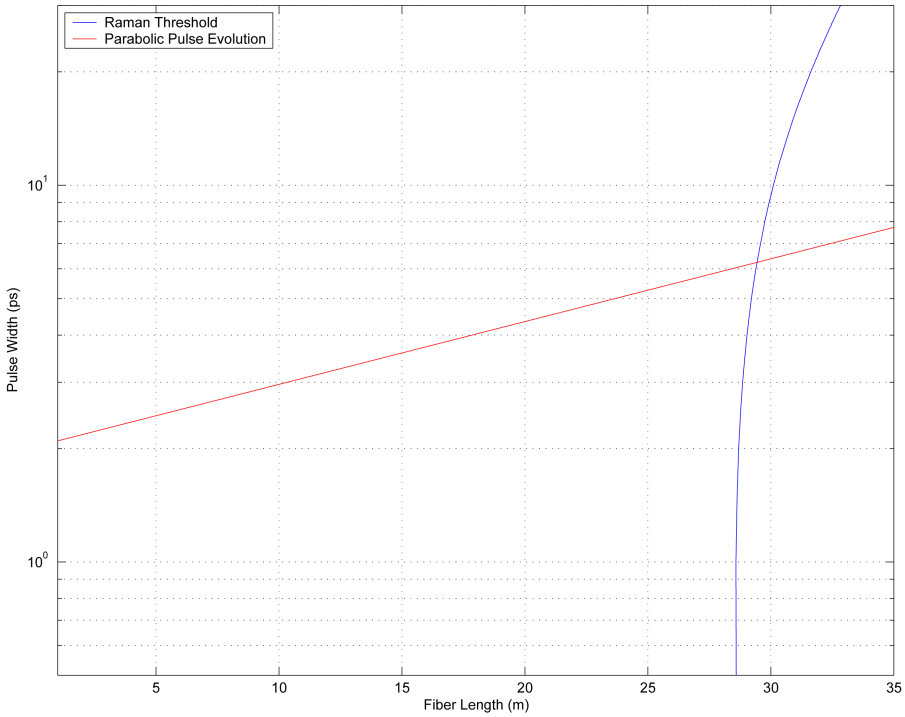

Figure 3.2: Raman Limit for Parabolic Pulse Formation

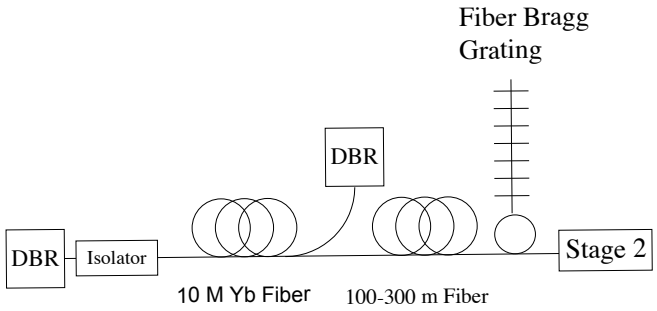

Figure 3.3: Schematic of Stage I

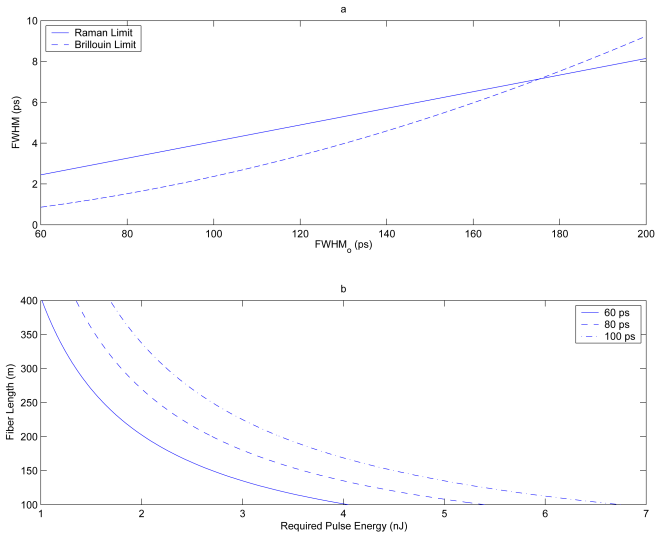

Figure 3.4: Stage I Parameters, (a), Pulse Compression at SRS and SBS Threshold, (b) Required Pulse Energy for 60, 80, and 100ps pulses

grating based compressor. With the components of stage I given, the necessary pulse duration, amplifier gain, and fiber length can be determined.

The maximum compression attainable is limited by the onset of either SRS or SBS. To find this limit, first note that the quantity $P_o^{cr}L$ is completely determined by the fiber parameters as can be seen from equations 2.29 and 2.30. Combining these equations with equation 2.8 yields the maximum spectral broadening attainable, and hence the shortest pulse duration that can be generated from an input pulse, and is given by

$$\Delta\tau = \frac{1}{\delta\omega_{max}} = \frac{g_r c T_o}{13.76 n_2 \omega_o}. \tag{3.2}$$

for SRS, and

$$\Delta\tau = \frac{1}{\delta\omega_{max}} = \frac{g_b c T_o}{18.06 n_2 \omega_o}. \tag{3.3}$$

for SBS, where it should be recalled that $g_b = g_{b,o} c T_o/(1 + \frac{\Delta\nu_p}{\Delta\nu_b})$. The above compression limits depend on physical characteristics of the fiber and the input pulse width

Both the SRS and SBS limits are shown in Figure 3.4a. So, in order to generate pulses shorter than 5 ps as required by stage II, an input pulse less than 120 ps must be launched into the compressor.

Next the necessary input energy and fiber length for a given pulse energy (after the amplifier) for several pulse durations are shown in Figure 3.4b. As the diode can couple between 5 and 7 pJ of energy into the amplifier, and a maximum gain of 26 or 27 dB can be obtained, the amplified pulse will have between 2 and 3.5 nJ of energy per pulse.

The diode generates pulses between 60 and 100 ps (depending on operation parameters), and so the required length of fiber can be found from Figure 3.4b. The upper and lower bounds set by the Raman limit are from a 2 nJ, 100 ps pulse requiring 335 m of fiber, and a 3.5 nJ, 60 ps pulse that requires 115 m of fiber to achieve a pulse shorter than 5 ps.

3.3 Overview of Experimental Setup

The setup for the entire system can be seen in Figure 3.5, with the setup drawn as implemented with a free space setup for pulse compression. The setup is fairly simple with a suitable seed source capable of emitting single frequency picosecond pulses that are then amplified before spectrally broadening in a long passive fiber. A grating based compressor then removes the linear and some third order chirp before the signal enters the second stage where it is amplified in a long amplifier where parabolic pulse formation occurs. Finally the first and third order chirp generated in the second stage are removed by a grating based compressor, with a femtosecond output pulse.

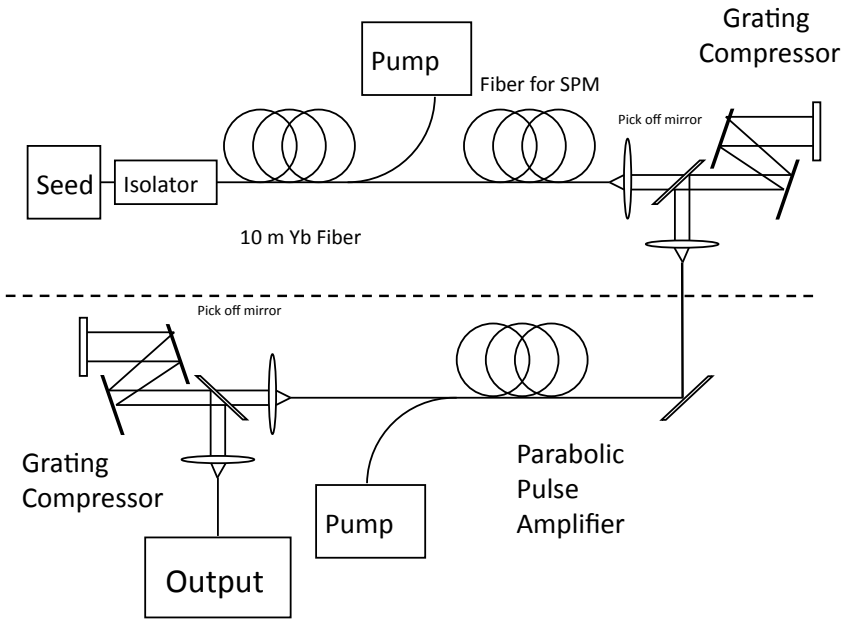

Figure 3.5: System Schematic of Entire Compression Setup. The portion above the dashed line constitutes the first stage, and below the second stage.

3.4 Experimental Setup for Single Longitudinal Mode Picosecond Seeder

To begin with, a suitable pulse must be generated. As arbitrary repetition rate and timing are desirable, a laser diode was selected as the seed source for the system. When a conventional Fabry-Perot (FP) laser diode is gain-switched and picosecond pulses emitted, multiple longitudinal modes are present as shown in Figure 3.6. this strong emmittance of multiple longitudinal modes is characteristic of diode lasers, as the optical path length of the cavity strongly depends on the carrier density, which for gain switching is changing substantially as well as rapidly. In the CW case, a large side mode suppression ratio is achieved due to the system being at equilibrium, and the mode with the largest gain saturating (i.e. depleting the carriers), which reduces the gain for other modes. However, in the transient regime, gain saturation and depletion doesn't occur, hence multiple modes achieve threshold and lase.

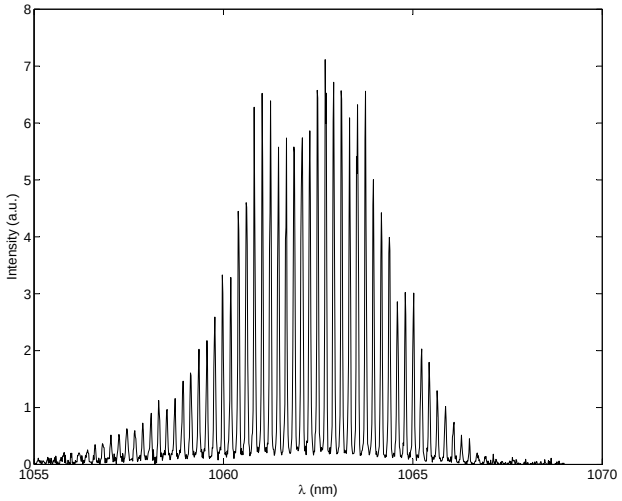

Figure 3.6: Multimode Spectrum of a Gain Switched Fabry Perot Laser Diode (FPLD)

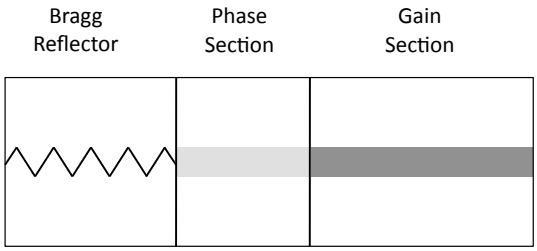

Figure 3.7: Three Section Distributed Bragg Reflector Laser Diode (DBR). The three sections are (i) a wavelength selective Bragg reflector, (ii) a phase section for controlling the optical path length of the cavity which can be used to tune the wavelength of the longitudinal modes, and (iii) the gain section of the laser diode.

In order to achieve spectral broadening in either the first or second stage it is necessary that the seed source emit light from only one longitudinal cavity mode of the diode laser. Two approaches were investigated for generating a pulse with the desired characteristics, the first employing a free running distributed Bragg reflector (DBR) laser diode, and the second using injection locked laser diodes, both DBR and Fabry-Perot.

3.4.1 Distributed Bragg Reflector Laser Diode

A DBR laser diode was used as a seed source, the structure of which is schematically shown in Figure 3.7. The DBR differs from a conventional Fabry-Perot laser diode (FPLD) in that the feedback is provided by a Bragg grating integrated into the semiconductor rather than solely from a fresnel reflection at the facet between semiconductor and air. The Bragg structure has a narrow reflectivity band that is designed such that the maximum reflectivity is near the gain peak. As the gain peak is substantially broader than the Bragg reflectivity peak, it is the Bragg peak which determines the longitudinal mode that lases.

The spectrum shown for the DBR when gain switched is shown in Figure 3.8a. Note that the diode is still multimode. For a single longitudinal mode to be present, the longitudinal mode spacing must be such that only one mode receives substantial feedback from the Bragg grating, a situation shown in Figure 3.9c. For the multimode gain switched case here, multiple longitudinal modes receive substantial feedback as shown in Figure 3.9d. The reason for the decreased spacing between the longitudinal modes of the cavity in Figure 3.9d is the increased length of the cavity.

The outcome of these experiments is that currently available DBR laser diodes with wavelengths centered around 1.064 μm are not capable of single longitudinal

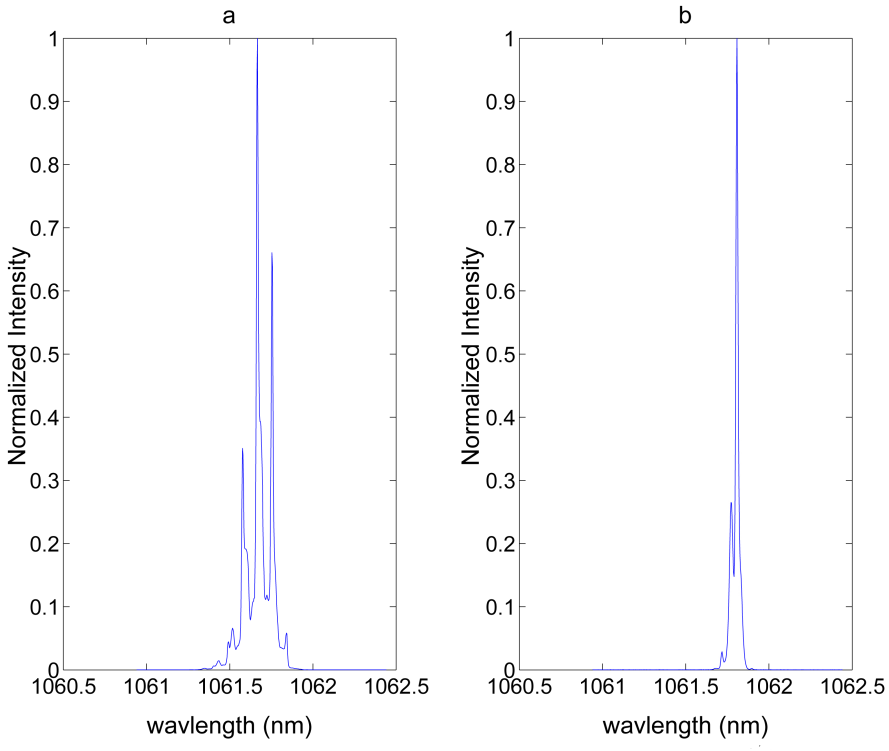

Figure 3.8: DBR spectrum when gain switched, (a) without injection locking and (b) with injection locking

emission when gain switched to generate picosecond pulses and therefore are not suitable for this application. Though the lack of such a diode is not due to technological reasons, but rather due to there currently being no market, as DBR diodes with wavelengths centered around 1.55 μm with suitable temporal and spectral characteristics are commercially available. Changing from a target wavelength of 1.064 μm to 1.55 μm was not a choice due to the second stage of this scheme relying on parabolic pulse formation which requires fibers with positive dispersion.

3.4.2 Injection Locked DBR Laser Diode

The distributed bragg reflector (DBR) laser diode was injection locked to a second DBR master oscillator, the latter running continuous wave (cw). The setup is shown in Figure 3.10. The results are shown in Figure 3.8b, where the spectrum was indeed

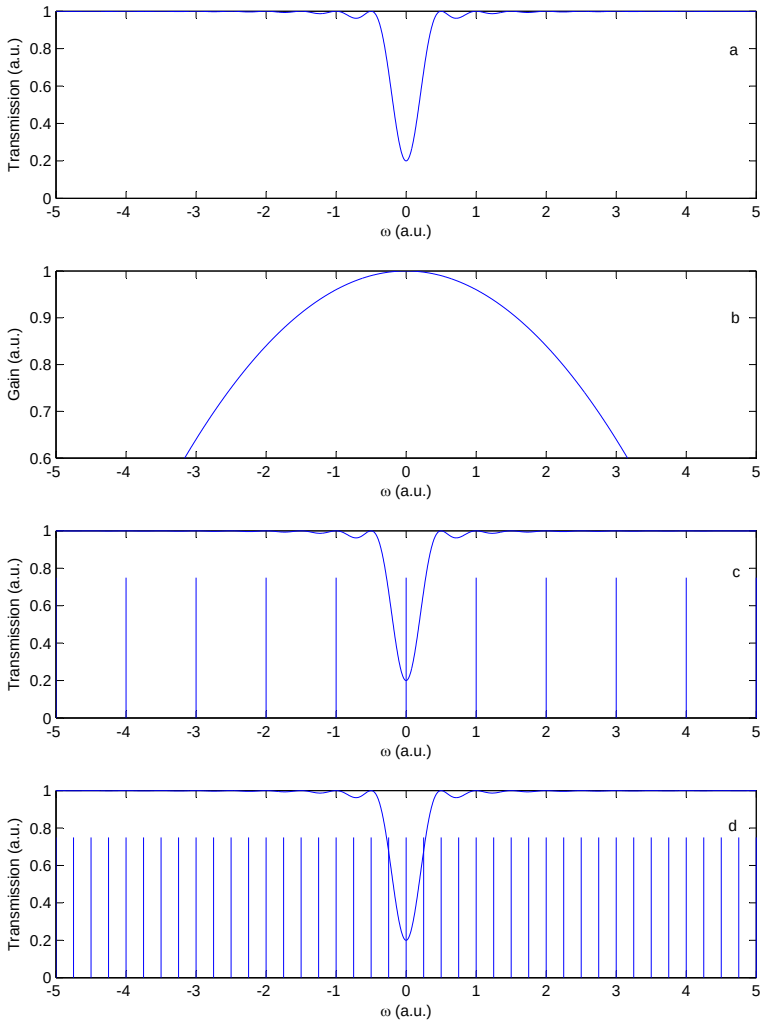

Figure 3.9: Spectral Characteristics of a DBR. (a) Transmission characteristic of the Bragg grating. (b) Laser diode gain spectrum. (c) Longitudinal mode spectrum shown with transmission function of the Bragg grating for a short cavity. Note that only a single longitudinal mode receives substantial feedback. (d) Longitudinal mode spectrum shown with transmission function of the Bragg grating for a long cavity. Note that more than one longitudinal mode receives substantial feedback

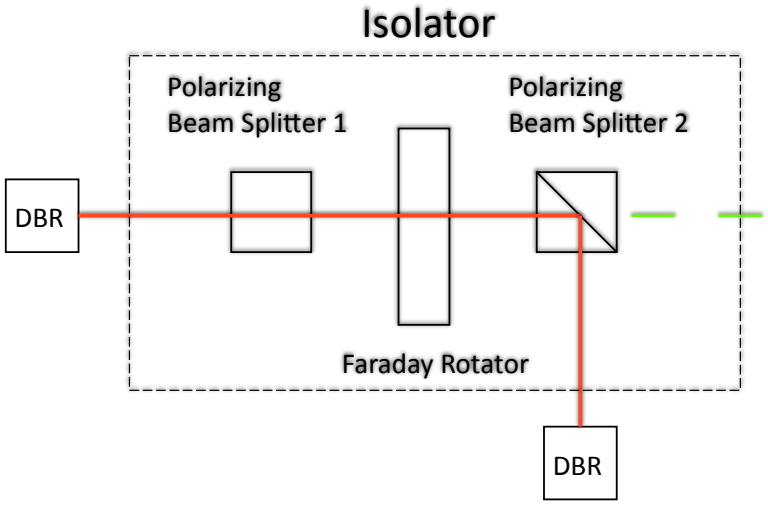

Figure 3.10: Injection Locking Schematic Using a Faraday Rotator. Note that the actual setup used waveplates to control the amount of light input from the master oscillator (quasi-cw), and the polarization of the light as it entered the slave (pulsed) laser diode, with the waveplates placed between the first polarizing beam splitter cube and the slave DBR.

cleaned up, but still showed multimode behavior.

3.4.3 Injection Locked Fabry Perot Laser Diode

An injection locking setup with two Fabry-Perot laser diodes is shown in Figure 3.11. The diodes are not identical, with the master oscillator having a linewidth less than less than 30 MHz, and the wavelength fixed by a Bragg grating which provides feedback. With the wavelength of the master laser diode fixed, the wavelength of the gain-switched laser diode was temperature tuned to lock the wavelength of the slave to the master diode. To implement temperature tuning, the gain switched laser diode was mounted on a TEC, with the temperature regulated by a Wavelength Electronics (WTC3243) temperature controller, with temperature feedback provided by a negative temperature coefficient thermistor (NTC, 25 kΩ at 25^o). Figure 3.16

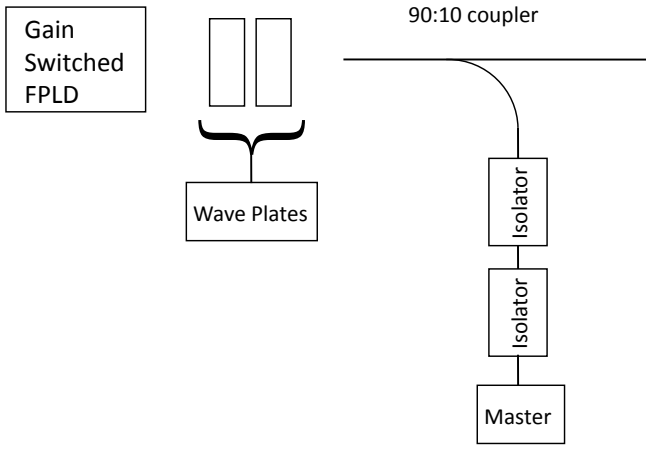

Figure 3.11: Schematic Diagram of Injection Locking Scheme for two FPLDs

shows the behavior of the diode when 60 picosecond gain switched pulses are generated by an 311 ps fwhm electrical pulse with and without injection locking. The free running gain switched slave laser diode (i.e. without injection locking) power was 67 μW while running at 800 kHz, with the continuous wave (cw) master laser diode operated at 123 μW.

3.5 Spectral Broadening of the Gain-Swithced Injection Locked Fabry-Perot Laser Diode

With only 84 pJ in each pulse, which coupling losses reduced to 42 pJ corresponding to a peak power of 700 mW, the pulses were amplified in a two stage amplifier as shown in Figure 3.12 in order to provide sufficient energy to produce the desired spectral broadening. After amplification the pulse energy was 18.3 nJ corresponding to a peak power of 306 W, which including coupling 50 % efficiency between the gain switched laser diode and the input fiber and the 90:10 coupler, corresponds to a net gain 26.4 dB. The amplified pulses were then input into 160 m of Corning HI1060 fiber, an SM fiber, where substantial spectral broadening occurred as can be seen in

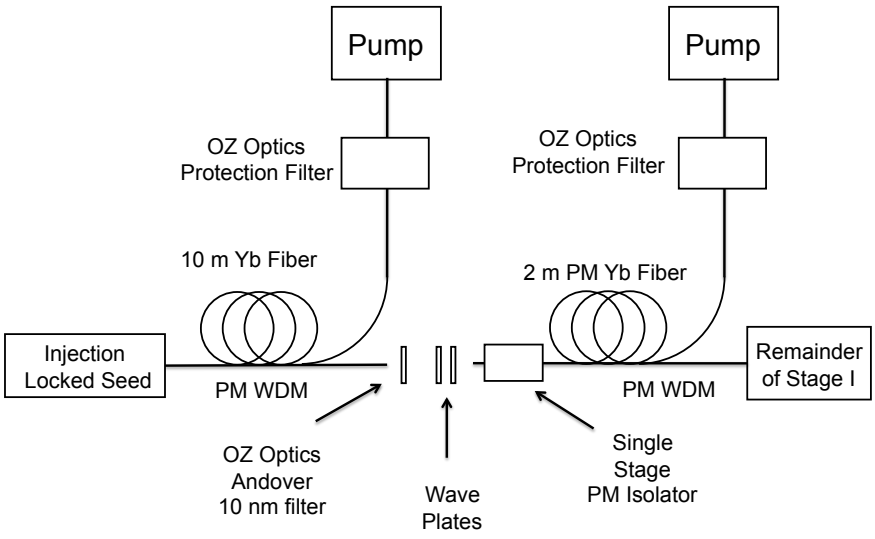

Figure 3.12: Free space dual stage amplification setup

Figure 3.13.

Though there are clearly undesirable features in the spectrum, the source of which was investigated in an effort to eliminate the unwanted features, the output pulse was compressed using a four pass compressor based on a 1200 groove per millimeter diffraction grating. A second harmonic generation autocorrelation was then taken as shown in Figure 3.14, and the fwhm of the autocorrelation found to be 6 ps, which corresponds to a pulse fwhm of 4.3 ps, which as previously discussed is sufficient to seed the second stage or parabolic pulse generation.

3.6 Analysis of the Spectrally Broadened Pulses from Stage I

Looking at Figure 3.13 the characteristic spectral modulation generated by self phase modulation can be seen, however it is also evident that there is a large central spectral component which did not undergo SPM, indicating that a substantial portion

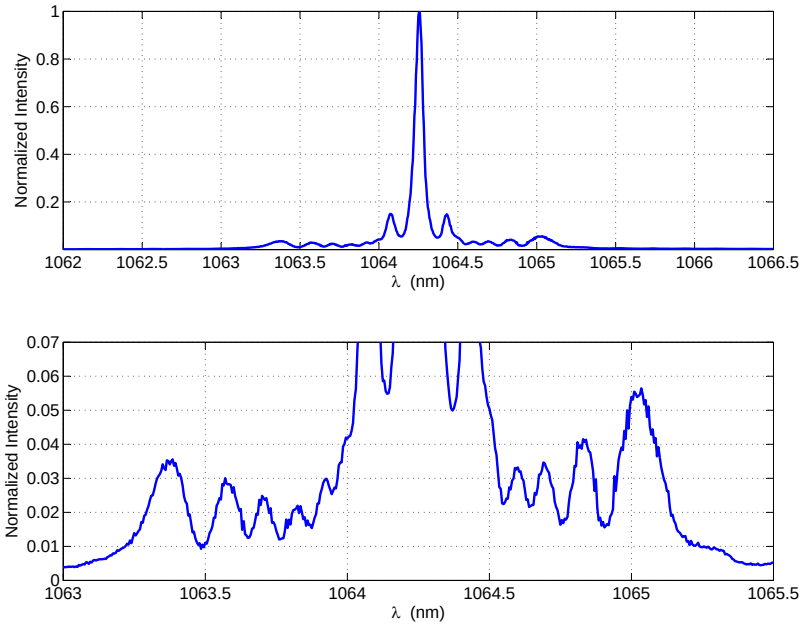

Figure 3.13: Measured spectral broadening for a 60 ps gain switched pulse after 160 m of HI1060 fiber. Top shows normalized intensity, while the bottom focuses on the fine structure which clearly shows the characteristics of self phase modulation (SPM), namely slower oscillations at the edges of the spectrum and faster oscillations towards the central

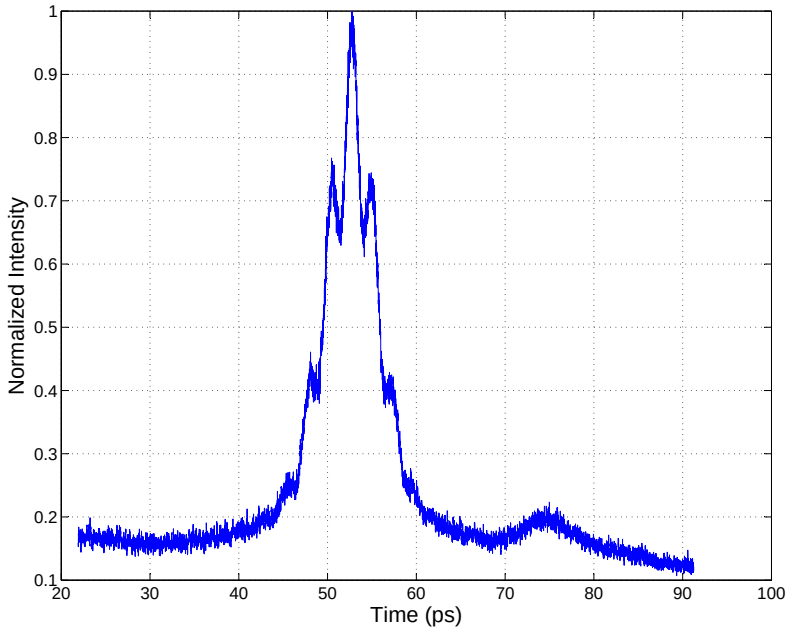

Figure 3.14: Measured SHG autocorrelation of compressed output pulse, which has a fwhm of 6 ps, which corresponds to a pulse width of 4.3 ps.

of the energy is either in the tail of the gain switched pulse or there is a substantial background continuous wave signal. An estimate of the peak power assuming that all of the energy is in a 60 ps gaussian pulse is 256 W. As $L_D \gg L \gg L_{NL}$ it is reasonable to use the simple relation given in equation 2.8, which yields a broadening of 7.7 nm. The simple estimate of spectral broadening compares well to the value determined from numerical solution of equation 2.2 of 6.95 nm, as can be seen in Figure 3.15. Seeing that the simple relation as given in equation 2.8 is fairly accurate for the fiber lengths and power considered here, the relation can be inverted to estimate the peak power of the pulse using the observed broadening of 2 nm, which for a 60 ps gaussian pulse is 58 W. This is nearly a factor of three less than the peak power estimated by assuming that all of the energy is in the pulse, so clearly a substantial portion of the power measured is not in the 60 ps pulse, leading to the conclusion that energy

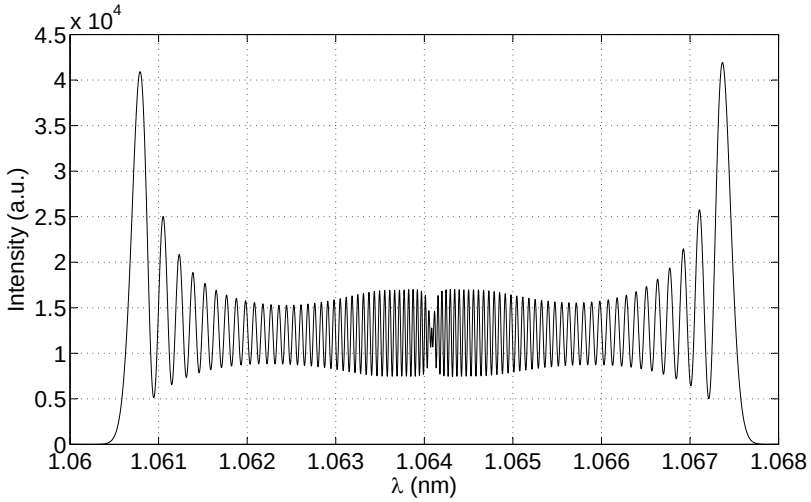

Figure 3.15: Numerically calculated spectral broadening for a 60 ps gaussian pulse with a peak power of 256 W

is in a cw or quasi-cw component, which does not undergo SPM. The two possible sources for this are a portion of the injected signal having been reflected from the diode facet and amplified, or that the gain switched diode itself has a long tail which contains a substantial portion of the pulse energy.

Operation of the laser was changed from a continuous wave (cw) to a pulsed configuration to determine if the un-broadened component is due to the injected signal. The injected seed was changed from a cw signal to a 30 ns pulsed signal with the average power reduced from 123 μW to 19.1 μW, and the peak power rising to 796 μW for the pulsed master seed. With the factor of six reduction in the injected signal, a substantial reduction in the central wavelength is to be expected if the source of the central wavelength component is due to a partial reflection of the master signal. However, as can bee seen in Figure 3.17, no such reduction is evident, indicating that the injected seed was not responsible for the observed component which did not undergo self-phase-modulation (SPM).

As can be seen in Figure 3.18 a substantial portion of the energy is in the tail.

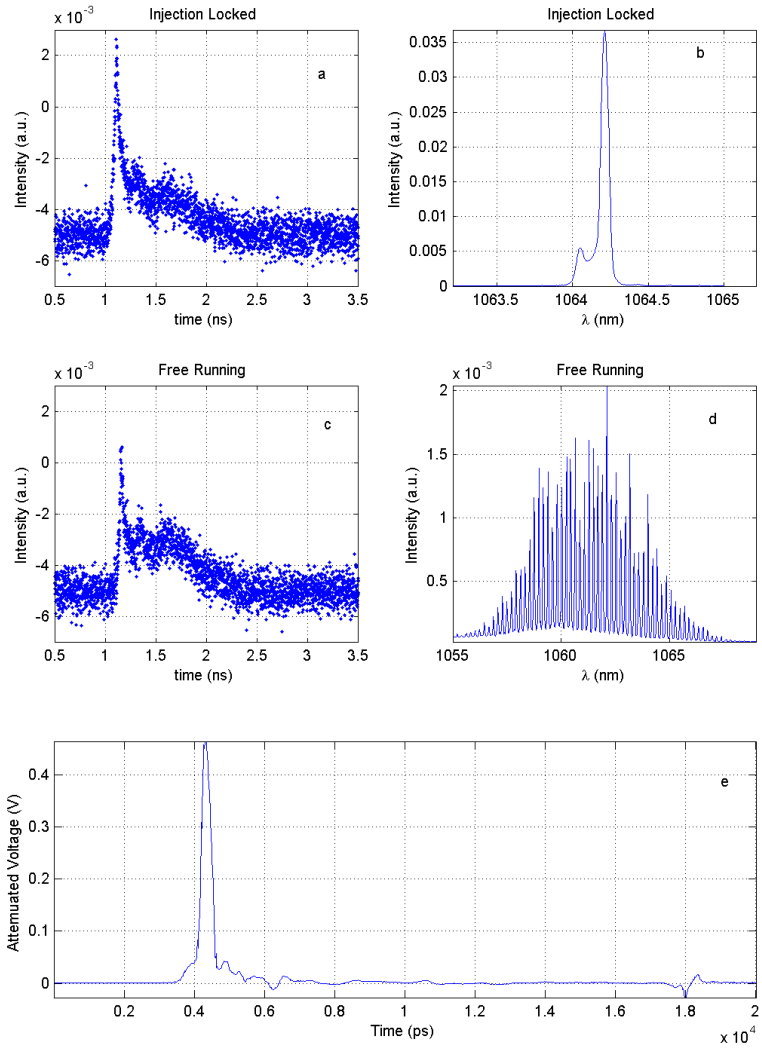

Figure 3.16: Gain switched pulses with and without injection seeding. Plots (a) and (b) showing the temporal and and spectral behavior when injection locked, and plots (c) and (d) without injection locking. Plot (e) is the electrical pulse (30 dB attenuation) driving the gain switched laser diode, which has a fwhm of 311 ps

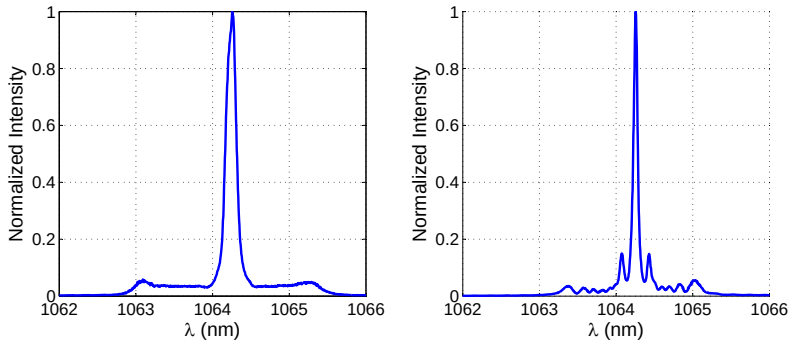

Figure 3.17: Spectrum of self-phase-modulation broadened pulses with a pulsed (left) and cw (right) master seed. The pulsed injection locked signal still has a large unbroadened central peak, with the energy in the peak comparable to that of the cw injection locked pulses.

Numerical integration of the pulse energy as shown in the figure, with the normalized integral shown in the lower portion gives the energy distribution to be 37% in the pulse and 63% in the tail. This roughly corresponds to the fraction of energy calculated to be in the pulse previously by calculating the peak power of the pulse knowing the spectral broadening by use of the relation in equation 2.9.

With suspicion cast upon the tail as the culprit responsible for the unbroadened central spectral peak, the effects of a 60 ps full-width-half-max pulse which has 67% of the total energy in the tail and a peak power of 108 W propagating through 160 m of passive fiber was investigated numerically, the results of which can be seen in Figure 3.19. The tail clearly produces a large unbroadened central peak, however the central peak is not as broad as that which was measured.

If the tail is responsible for the observed component which did not undergo SPM, then a reduction of the energy in the tail should reduce the observed un-broadened component. The reduction of the energy in the tail can be seen in Figure 3.20, which again had repetition rate of 800 kHz, however the average power was 20.5 mW. The energy in the tail was reduced by over a factor of three from 67% to 19%, which is a substantial reduction of the energy in the tail, and if the energy visible in the tail is

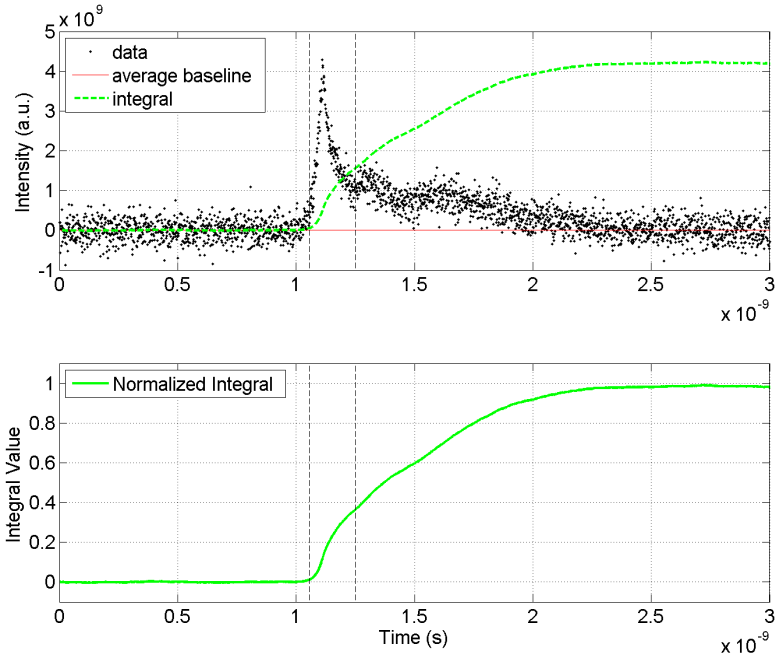

Figure 3.18: Temporal profile of the injection locked pulse, and the integral as a function of time. (a) Temporal profile and integral. (b) Normalized Integral as a function of time.

responsible for the observed unbroadened central spectral peak then a corresponding reduction of this peak is expected. However, the spectrum shown on the right hand side of Figure 3.20 still clearly shows a large central peak. This indicates that a large portion of the energy still is not undergoing SPM and that the observed tail in the temporal profile is not responsible for the observed central peak.

3.7 Numerical Investigation of Parabolic Pulses with 5 ps Pulses

With the output pulses generated from stage I containing a large amount of energy that was not spectrally broadened, the second stage was not built. This was due to the fact that a substantial amount of the amplified signal in the second stage would be the narrow band central component, and a suitable method for eliminating this central peak has not been found and implemented. However a more detailed

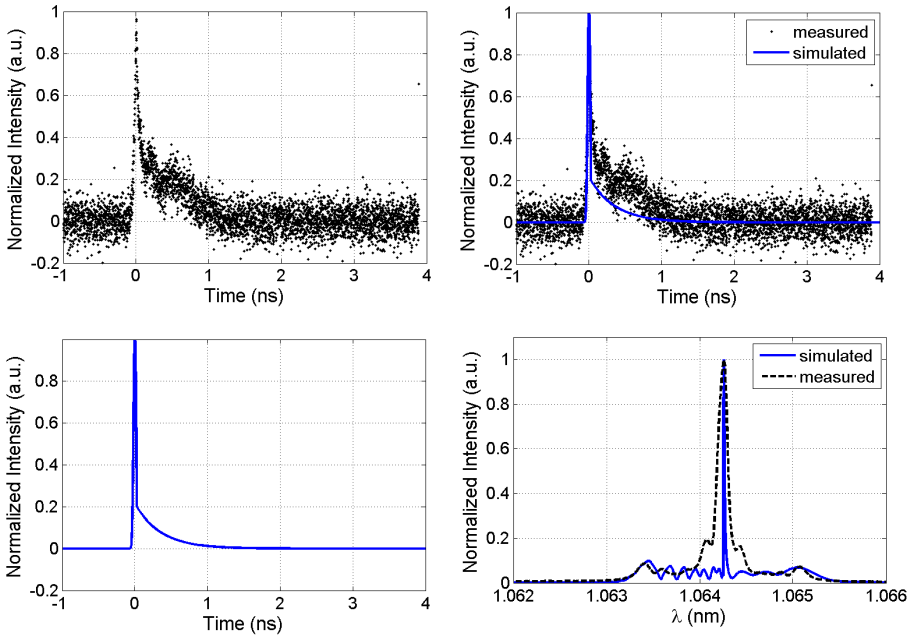

Figure 3.19: Simulation and comparison of a pulse with 67% of its energy in the tail. (a) Measured Temporal Profile. (b) Both temporal profiles. (c) Temporal profile of pulse with 67 % of the pulse energy in the tail which was simulated. (d) Comparison of measured and simulated spectra.

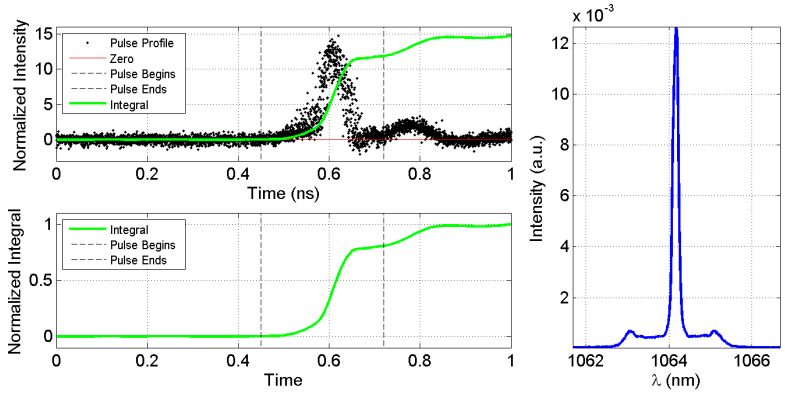

Figure 3.20: Temporal profile of a pulse with 81% of the energy in the pulse and 19% in the tail, corresponding to a substantial increase in the concentration of energy in the main pulse. The corresponding self-phase-modulation broadened spectrum (right) still shows a substantial fraction of the energy contained in an unbroadened central peak.

numerical investigation of the possibility of forming parabolic pulses generated from self-phase-modulation (SPM) broadened pulses was undertaken. The original determination of the possibility of parabolic pulse compression of SPM broadened pulses was based on two factors. The first being the literature [1, 25, 26, 27, 28], which suggested that convergence to the asymptotic solution was independent of the specific temporal and spectral profiles. The second factor being the result of numerical solution of the nonlinear Schrödinger equation (NLSE) starting with an unchirped 4 ps gaussian pulse as shown in Figure 3.21 (solid blue line). The corresponding chirp, temporal and spectral profile of the asymptotic parabolic pulse (dashed red line) as given by equations 2.20, 2.23, and 2.24 respectively are also plotted for comparison. Such a comparison shows fairly reasonable agreement between the numerical and asymptotic solutions, though there is some discrepency between them. By removing the phase from the pulse, the pulse can be compressed to 130 fs fwhm, meeting the original requirements of the system.

With the simple case of generating parabolic pulses from 4 ps gaussian pulses recapitulated, the more sophisticated analysis required for parabolic pulse generation from 60 ps gaussian pulses can now be completed, and a comparison between the simple and more complex cases done. Simulations of stage I started with a 1.25 nJ, 60 ps gaussian pulse propagated through 160 m of fiber is shown in Figure 3.22, and from which the linear chirp is removed such that the pulse is nearly transform limited, and the energy reduced to 66 pJ for the second stage. The compressed pulse, with fwhm of 4 ps is then amplified in a 25 m fiber amplifier with 25 dB gain to generate parabolic pulses, the results of which may be seen in Figure 3.23. It should be noted that there is a good amount of structure evident in all three plots shown, and that the deviation from a parabolic pulse is substantial, most especially in the spectral

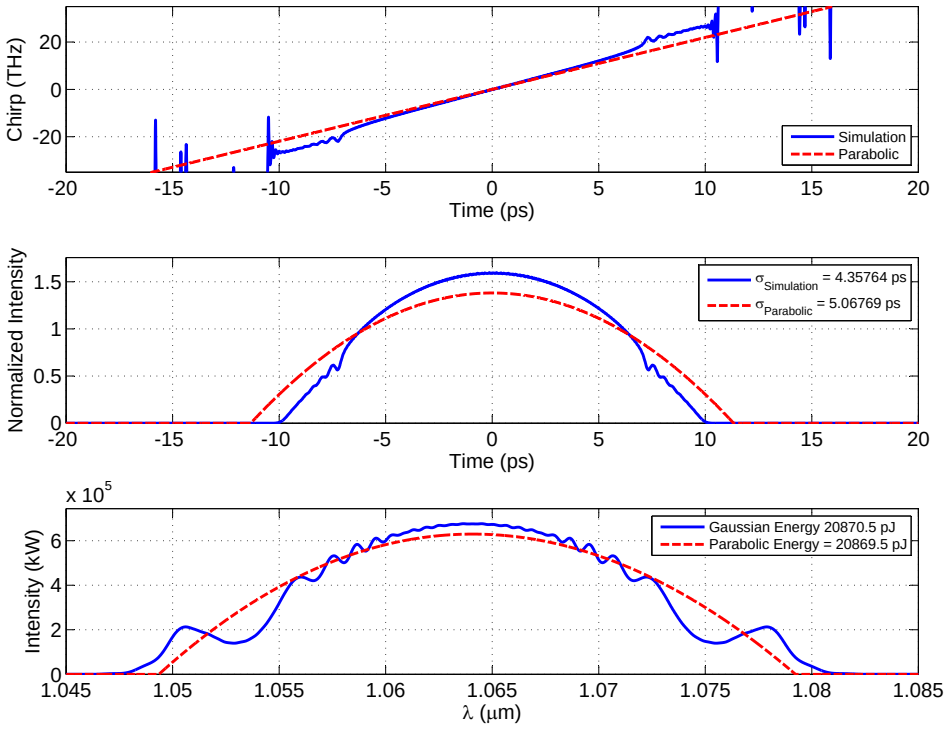

Figure 3.21: Numerical Simulation of 66 pJ, 4 ps gaussian pulse, showing chirp (top), temporal profile (middle), and spectrum (bottom). Each plot shows both the numerical simulation results (blue, solid) and asymptotic parabolic pulse solution (red, dashed).

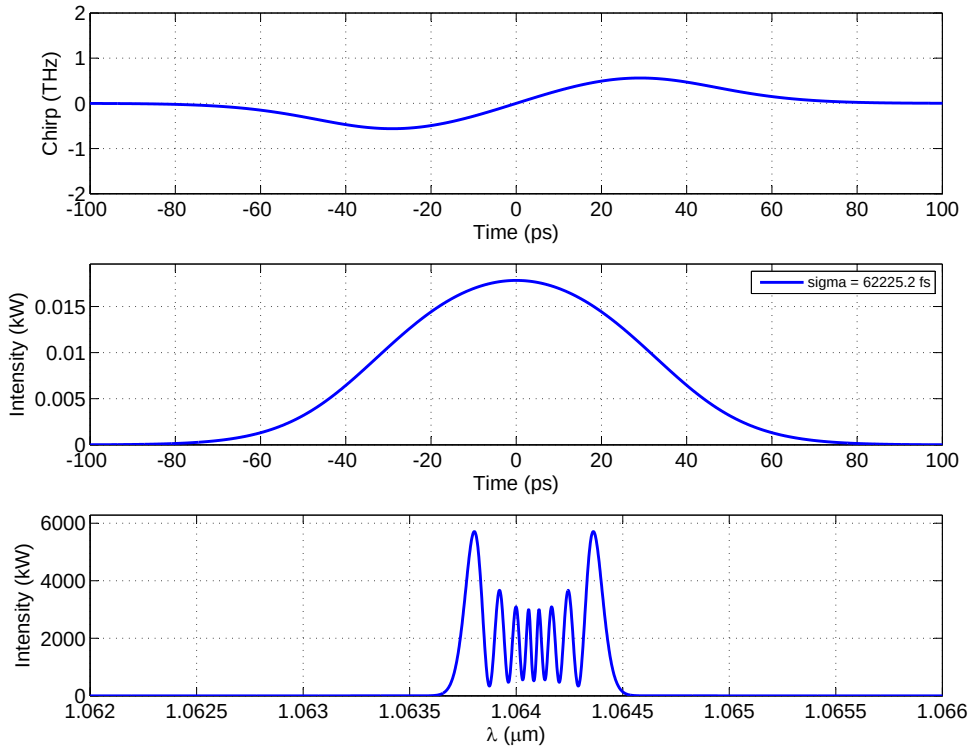

Figure 3.22: Numerical Simulation of 1.25 nJ, 60 ps gaussian pulse, showing chirp (top), temporal profile (middle), and spectrum (bottom). Each plot shows both the numerical simulation results (blue, solid) and asymptotic parabolic pulse solution (red, dashed).

domain, where it should be recalled that in addition to the temporal profile being parabolic, the spectrum is as well, and it is in the spectral domain where this lack of congruence between the asymptotic and numerical solution for parabolic pulses is most evident. The source of the structure both spectrally and temporally is the presence of the same frequency component at different times along the pulse. That the same frequency component is present at several times during the pulse can be seen in the chirp plot by recalling that the instantaneous frequency is $\omega_o + d\omega/dt$, where the second term in the relation is just the chirp.

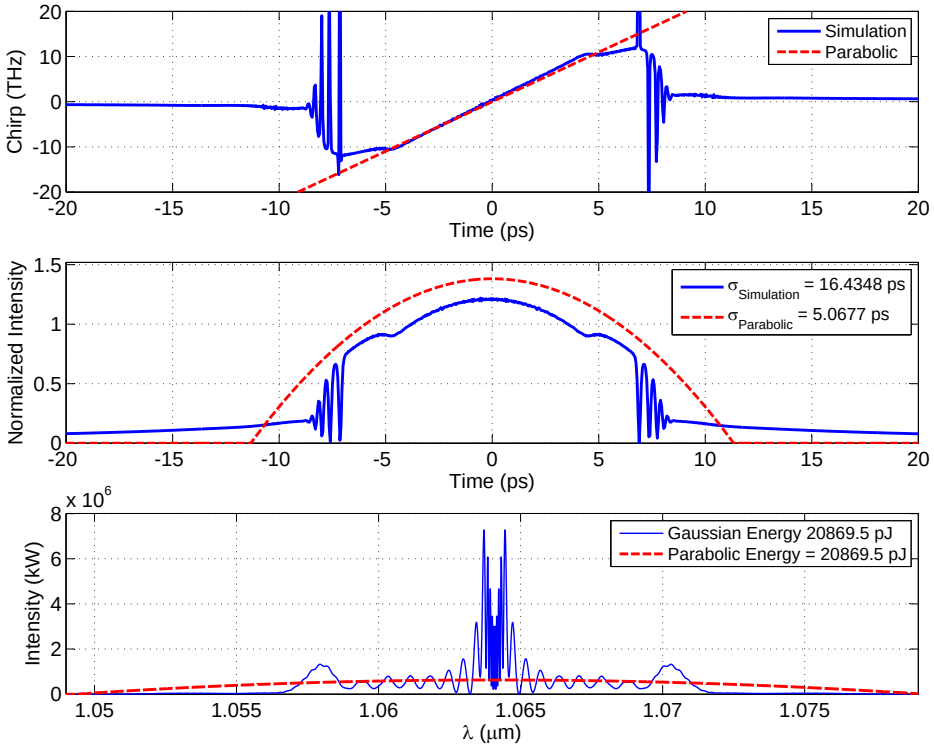

Figure 3.23: Numerical Simulation of 60 pJ, 2 ps pulse generated by compression of Stage I SPM broadened pulse, showing chirp (top), temporal profile (middle), and spectrum (bottom). Each plot shows both the numerical simulation results (blue, solid) and asymptotic parabolic pulse solution (red, dashed).

3.8 Conclusions

Generation of parabolic pulses from commercially available diodes using a two stage approach has been presented and discussed. In this work two problems have been identified that must be resolved before moving forward with this approach. First, it was found that gain-switched pulses from a standard diode laser appear to have number of characteristics not well suited for producing clean SPM-broadened pulses, such as an asymmetric temporal shape which has a long pulse tail. Second, it was found that, though parabolic pulse formation occurs for any arbitrary input temporal pulse profile, the deviation from the optimum parabolic input results in extensively spectrally-modulated SPM-broadened pulses, which are unsuitable for seeding fiber-based CPA systems. In conclusion, results of this study indicate that the approach of generating SPM-broadened pulses from pulsed laser diodes has to be modified from the initial approach explored in this thesis.

CHAPTER IV

Introduction to High Power Fiber Technology

4.1 Introduction

Demand for high power coherent light sources for a variety of applications including extreme ultraviolet generation, material processing, characterization and spectroscopy have driven the development of high power lasers and amplifiers ever further. Towards this end, fiber technology has provided reliable, robust, and compact systems capable of delivering muti-kW average [29], and multi-MW peak powers [30] with near diffraction limited beam quality. Current commercially available high power fiber systems are based on either a large core fiber with very weak guidance allowing single mode operation, or a mildly multi-mode large mode area fiber where mode management techniques yield a near diffraction limited output beam. This chapter will review the modal structure of fibers, current techniques for obtaining near diffraction limited output from high power lasers and amplifiers, and lay the foundations necessary to understand the performance of a laser or amplifier, as well as the techniques used to design chirally coupled core fibers (CCC).

The chapter begins with a discussion the modal structure of fibers and a description of the nature of the problem for power scaling as well as the current techniques employed to generate near diffraction limited output from fibers having a large mode

field diameter. The chapter will conclude with a description of an effectively single mode fiber based on the CCC structure, as well as the background necessary to understand the techniques employed to design the fiber. The following chapter will cover the experimental setup, results and analysis of laser and amplifier systems built using CCC fiber.

4.2 Modal Structure for Weakly Guiding Fibers

Fibers consist of cylindrically symmetric guiding and cladding regions with refractive indices of n_1 and n_2 respectively, where $n_1 > n_2$ allowing light to be guided in the core region by total internal reflection. Rather than explicitly referring to the refractive indices of the core and cladding region, the numerical aperture (N.A.) is frequently used, which gives the sine of the maximum acceptance angle of light incident on the fiber at an air (refractive index n_0), interface as given below.

$$N.A. = sin\theta_{NA} = \frac{1}{n_0}\sqrt{n_1^2 - n_2^2} \tag{4.1}$$

Exact solutions of Maxwell's equations which allow for electric and magnetic field vectors to point in the transverse (i.e. $\hat{\phi}$ and $\hat{r}$) as well as along the propagation direction ($\hat{z}$), and are given in Table 4.2, where the normalized transverse phase and attenuation constants u and v respectively, are defined as

$$u = \beta_{t1}a = a(n_1^2k_0^2 - \beta^2)^{1/2} \tag{4.2}$$

$$w = |\beta_{t1}|a = a(\beta^2 - n_2^2k_0^2)^{1/2} \tag{4.3}$$

, with "a" the diameter of the core and k_0 the wave vector with the usual definition of $2\pi/\lambda$. Note that both u and v are real, which requires that

$$n_2k_0 < \beta < n_1k_0 \tag{4.4}$$

$r < a:$	$E_z = AJ_q(\frac{ur}{a})sin(q\phi)e^{-i\beta z}$
	$E_r = [-A\frac{i\beta}{(u/a)}J'_q(\frac{ur}{a}) + B\frac{i\omega\mu}{(u/a)^2}\frac{q}{r}J_q(\frac{ur}{a})]sin(q\phi)e^{-i\beta z}$
	$E_\phi = [-A\frac{i\beta}{(u/a)^2}\frac{q}{r}J_q(\frac{ur}{a}) + B\frac{i\omega\mu}{(u/a)}J'_q(\frac{ur}{a})]cos(q\phi)e^{-i\beta z}$
	$H_z = BJ_q(\frac{ur}{a})cos(q\phi)e^{-i\beta z}$
	$H_r = [A\frac{i\omega\epsilon_0 n_1^2}{(u/a)^2}\frac{q}{r}J_q(\frac{ur}{a}) - B\frac{i\beta}{(u/a)}J'_q(\frac{ur}{a})]cos(q\phi)e^{-i\beta z}$
	$H_\phi = [-A\frac{i\omega\epsilon_0 n_1^2}{(u/a)}J'_q(\frac{ur}{a}) + B\frac{i\beta}{(u/a)^2}\frac{q}{r}J_q(\frac{ur}{a})]sin(q\phi)e^{-i\beta z}$
$r > a:$	
	$E_z = CK_q(\frac{wr}{a})sin(q\phi)e^{-i\beta z}$
	$E_r = [C\frac{i\beta}{(w/a)}K'_q(\frac{wr}{a}) - D\frac{i\omega\mu}{(w/a)^2}\frac{q}{r}K_q(\frac{wr}{a})]sin(q\phi)e^{-i\beta z}$
	$E_\phi = [C\frac{i\beta}{(w/a)^2}\frac{q}{r}K_q(\frac{wr}{a}) - D\frac{i\omega\mu}{(w/a)}K'_q(\frac{wr}{a})]cos(q\phi)e^{-i\beta z}$
	$H_z = DK_q(\frac{wr}{a})cos(q\phi)e^{-i\beta z}$
	$H_r = [-C\frac{i\omega\epsilon_0 n_2^2}{(w/a)^2}\frac{q}{r}K_q(\frac{wr}{a}) + D\frac{i\beta}{(w/a)}K'_q(\frac{wr}{a})]cos(q\phi)e^{-i\beta z}$
	$H_\phi = [C\frac{i\omega\epsilon_0 n_2^2}{(w/a)}K'_q(\frac{wr}{a}) - D\frac{i\beta}{(w/a)^2}\frac{q}{r}K_q(\frac{wr}{a})]sin(q\phi)e^{-i\beta z}$

Table 4.1: Exact Solutions of Maxwell's Equations in a Cylindrically Symmetric Step Index Dielectric Waveguide

for a mode to propagate in the core region and be attenuated in the radial direction. For $\beta < n_2 k_0$ light can propagate along the z axis, however the light also propagates along the radial direction, and hence power is lost from the guiding structure. These *"modes"* are known as leaky waves.

While the solutions of Table 4.2 are correct, for the vast majority of fibers produced, as well as those which are the topic of this and the following chapter, the index difference between the core and cladding regions is very small, and the fibers are not very strongly guiding. For weakly guiding fibers the field strength along the $\hat{z}$ direction is a factor on the order of $\sqrt{\Delta}$ less than the field strength of the transverse

components, where Δ is the normalized index difference, as defined in 4.5.

$$\Delta = \frac{n_1^2 - n_2^2}{2n_1^2} \approx \frac{n_1 - n_2}{n_1} = \frac{\delta n}{n_1} \tag{4.5}$$

With weak guidance, the fields can be satisfactorily decomposed along only the transverse directions, and as such can be represented in cartesian components as E_x and E_y for the electric field or H_x and H_y for the magnetic field. Modes for the weakly guiding fiber structure are known as the (LP) linearly polarized modes, and are a solution of the wave equation as shown in 4.6 and 4.7 below

$$\nabla_t^2 E_{x1} + (n_1^2 k_0^2 - \beta^2) E_{x1} = \nabla_t^2 E_{x1} + \beta_{t1}^2 E_{x1} = 0 \tag{4.6}$$

$$\nabla_t^2 E_{x2} + (n_2^2 k_0^2 - \beta^2) E_{x2} = \nabla_t^2 E_{x2} + \beta_{t1}^2 E_{x2} = 0 \tag{4.7}$$

, which in cylindrical coordinates becomes

$$\frac{\partial^2 E_x}{\partial r^2} + \frac{1}{r}\frac{\partial E_x}{\partial r} + \frac{1}{r^2}\frac{\partial^2 E_x}{\partial \phi^2} + \beta_t^2 E_x = 0 \tag{4.8}$$

where the usual separation of variables in cylindrical coordinates

$$E_x = \sum_i R_i(r)\Phi_i(\phi)e^{i\beta_i z} \tag{4.9}$$

is employed. The solutions have the form

$$R(r) = \begin{cases} AJ_l(\beta_l r) + A'N_l(\beta_l r) & \beta_t \quad real \\ CK_l(|\beta_l| r) + C'N_l(|\beta_l| r) & \beta_t \quad imaginary \end{cases} \tag{4.10}$$

and

$$\Phi(\phi) = \begin{cases} cos(l\phi + \alpha) \\ sin(l\phi + \alpha) \end{cases} \tag{4.11}$$

where l is an integer due to the boundary condition on Φ, and α is an arbitrary constant phase. By employing the boundary conditions at zero and infinite radius,

the the electric and magnetic fields are

$$E_x = \begin{cases} AJ_l(ur/a)cos(l\phi)e^{-i\beta z} & r \leq a \\ CK_l(wr/a)cos(l\phi)e^{-i\beta z} & r \geq a \end{cases} \tag{4.12}$$

and

$$H_y = \begin{cases} BJ_l(ur/a)cos(l\phi)e^{-i\beta z} & r \leq a \\ DK_l(wr/a)cos(l\phi)e^{-i\beta z} & r \geq a \end{cases} \tag{4.13}$$

where β is the propagation constant. The modes are designated as LP_{lm}, where l and m are integers designating the number of azimuthal and radial nodes. The azimuthal nodes, as mentioned previously are determined by requiring a complete revolution about the z-axis should bring the field back to the starting value as determined by equation 4.11. The radial boundary conditions set the number of radial nodes, which are found by graphical or numerical solution of the transcendental equation 4.14.

$$\frac{J_{l-1}(u)}{J_{l-1}(u)} = -\frac{w}{u}\frac{K_{l-1}(w)}{K_l(w)} \tag{4.14}$$

The normalized frequency paramter V,

$$V = (u^2 + v^2)^{1/2} = ak_0(n_1^2 - n_2^2)^{1/2} = n_1 ak_0\sqrt{2\Delta} \tag{4.15}$$

, defines the highest value for m allowed, the first few values of which are 2.405 (m=1) 3.832 (m=2) and 5.520 (m = 3), which are just the zeroes of the modified bessel function (i.e. $K_l(w)$). As an example, if a fiber has a V number between 3.832 and 5.520 there will be modes with m values of zero, one and two. It should be noted that a zeroth order mode (i.e. m = 0) is always present so that if the V number is below 2.405, then the fiber is single mode (SM) and only allows one mode to propagate. Using the forms given above, the intensity profiles for the first four fiber modes as shown in Figure 4.1, where the radial and azimuthal nodes can clearly

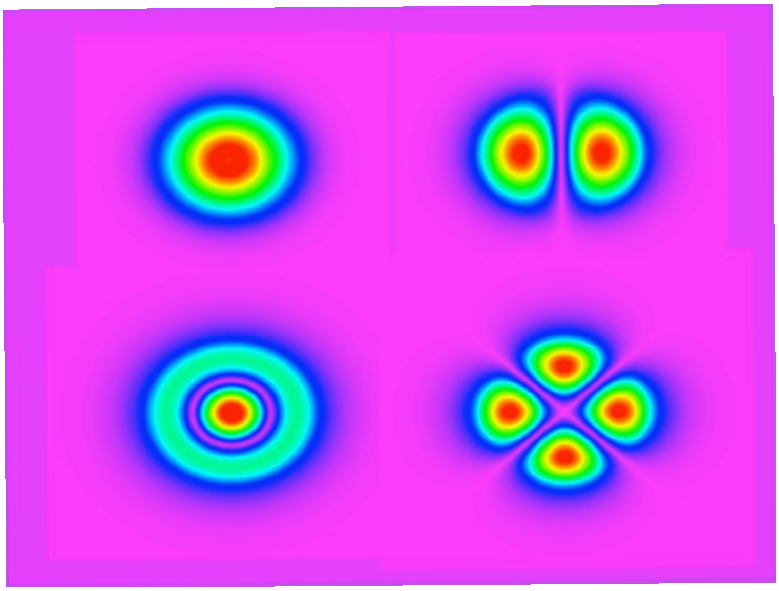

Figure 4.1: Mode profiles of the first four fiber modes. The modes are LP_{01} (upper left), LP_{11} (upper right) ,LP_{02} (lower left) , and LP_{21} (lower right

be seen. Note that the LP_{0m} modes have no azimuthal nodes, and are cylindrically symmetric, a fact that is exploited in the design of the CCC fiber to differentially select which modes are extracted from the fiber, and also which modes will propagate with low loss.

4.3 Review of Current Mode Management Techniques and Their Limitations

For power scaling, the larger the core cross section, the higher the peak or average power a fiber can handle without detrimental nonlinear effects degrading the

performance of the fiber. As mentioned previously, fibers designed for high power extraction use a double clad geometry for increasing the cross section of the waveguide for the pump light, mitigating nonlinearities from the pump. A similar strategy is employed for the inner or signal cladding, where the core is made as large as possible. This is either done in one of two manners; using a photonic crystal fiber (PCF) which has extremely weak guidance allowing for single mode operation with a large core, or mode management techniques to operate a mildly multimode fiber so that it has near diffraction limited output, and hence operates in the fundamental mode.

4.3.1 Photonic Crystal Fibers

Doped photonic crystal fibers used to build lasers and amplifiers have a solid core of dimension 2Λ which is surrounded by a periodic array of holes outside of the core region, with period Λ, making up a low refractive index cladding region. For the type of photonic crystal fiber (PCF) used for gain media, the holes in the cladding region slightly depress the average refractive index of the cladding so that total internal reflection is the guidance mechanism as it is in conventional single mode and large mode area fibers. For a PCF, the V number is

$$V_{PCF} = \frac{2\pi}{\lambda}\Lambda\sqrt{n_1^2 - \langle n_2\rangle^2} \tag{4.16}$$

where n_1 is the core refractive index, and $\langle n_2\rangle$ is the average refractive index in the cladding region. The single mode criterion for PCF is $V_{PCF} \leq \pi$, and not 2.405 due to the solutions to Maxwell's equations for PCF not being Bessel functions as was the case for the earlier cylindrically symmetric step index case. With a very low NA, typically around 0.03 for PCF, compared to 0.06 for conventional large mode area (LMA) fiber, the guidance mechanism is very weak. With such a low NA, single mode operation can be achieved for a very large core size.

Photonic crystal fiber however, has two significant deficiencies, weak guidance and the technical difficulties splicing PCF with a mode field diameter (MFD) beyond 29 μm. Weak guidance renders the fiber susceptible to bend induced loss, where a substantial amount of power can be radiated from the fiber. For systems operating at the hundred watt level and beyond this will destroy the fiber, and so the fiber must not have any bends. To ensure that the fiber remains straight it is made with a very large cladding, typically 2-3 mm in diameter, which is substantially larger than conventional LMA double clad fibers where the cladding region is 200-400 μm in diameter. This very large cladding prevents the fiber from bending and destroying itself. The difficulty which arises from this solution to the problem is twofold. First, the thermal management advantages of fibers, where the large surface area to volume ratio facilitates heat extraction, is greatly reduced for the PCF which is more appropriately called a rod rather than a fiber. The second is that the rod cannot be coiled, negating one of the principal advantages of fiber systems over conventional solid state systems, namely a small footprint, so that the oscillators or amplifiers built using PCF have a cavity length on the order of 1 m.

The final disadvantage for PCF based systems is that splicing PCFs with mode field diameters of 29 μm and beyond is not possible due to practical considerations, and so serves a second impediment to a compact system, as well as limiting the robustness of the performance of PCF based systems, due to the need to perform careful free space alignment.

4.3.2 Mildly multi-mode large mode area fibers and mode management techniques

The most commonly available type of high average power fiber laser systems are based on large mode area (LMA) fibers which have near diffraction limited output

due to the application of mode management techniques. These fibers are fairly weakly guiding, with a typical NA of 0.06, and only support a few guided modes for core sizes in the range of 20-30 μm. In order to operate the fibers in a single mode, a differential loss mechanism is employed to introduce higher loss for higher order modes (HOM). Second, careful excitation of the signal at the input for an amplifier can result in a large portion of the power being contained in the fundamental mode at the input, making higher order mode extraction from the fiber a more feasible prospect, a technique known as single mode excitation.

To introduce high loss for the higher order modes, the fiber is coiled to create bend-induced loss, which is larger for the higher order modes due a larger average value of r as compared to the fundamental mode. The mechanism for this loss, is shown in Figure 4.2, and is the requirement of phase continuity across the phase front, which here is a constant angular phase, and is governed by the following equation

$$\beta(r) = \frac{r_c}{r}\beta(r_c) \tag{4.17}$$

where r_c is the radius of the bend. For larger radii, the phase velocity, $\frac{\omega}{\beta}$ must be larger to maintain a constant phase front, and there comes a point where superluminal velocity is required, which is of course physically impossible. In order to meet this requirement of a constant phase across the curved waveguide, the wave vector $\vec{k}$ acquires a radial component such that the projection of the propagation vector into the $\hat{\phi}$ direction yields a smaller value of β and hence a larger phase velocity without exceeding the speed of light. This however comes at the price that power does not flow along the wave guiding structure beyond a critical radius, r_c. As the average value of $\langle R(r)^2 \rangle$ (4.10) is larger for HOMs, they are lossier than the fundamental

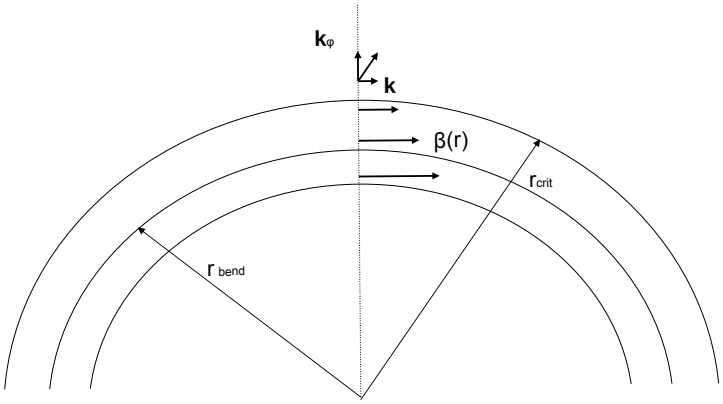

Figure 4.2: Schematic diagram of bend loss.

mode at a given radius. Bend induced loss from coiling for a fiber is calculated from

$$\alpha_b^{fiber} = \frac{\sqrt{\pi}u^2 e^{-\frac{3}{2}(w^3/a^3\beta^2)r_b}}{q_l w^{2/3} V^2 \sqrt{r_b a} K_{l-1}(w) K_{l+1}(w)} \tag{4.18}$$

where q_l is 2 for l equal to 0, and 1 otherwise. From this equation, the modal loss for a 0.06 NA, 20 μm LMA fiber was determined, and plotted for the first two modes, as shown in Figure 4.3. From the figure t is clearly evident that for a coiling radius in the neighborhood of 12-13 cm, the loss for the fundamental mode is much less than that of the first HOM. By reviewing equation 4.10, it is obvious that modes higher than LP_{11} have a larger average radial distribution and so equation 4.18 makes it clear that these higher order modes will have more loss than the first higher order mode, so if the fiber is coiled tight enough to remove LP_{11}, then all higher order modes will be removed from the core as well.

Coiling as a mode management technique has its limitations, namely that the

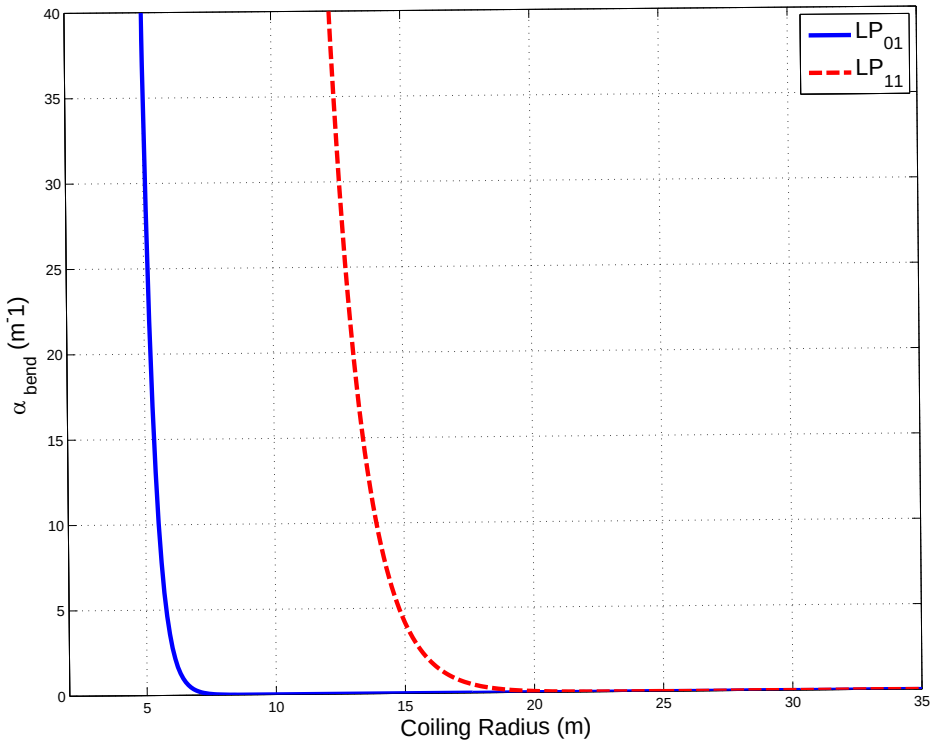

Figure 4.3: Modal loss due to coiling for LP_{01} and LP_{11}

range for small fundamental mode loss loss while achieving large HOM loss becomes very small, and it is not then possible to coil a fiber to only be loss for the HOM modes. The second difficulty for this technique is that each splice in a fiber system has inhomogeneities that causes scattering of light from the fundamental mode into higher order modes, and coiling is insufficient to extract the light from the higher order modes for monolithic systems for cores beyond $\sim$25 μm. This makes makes diffraction limited output from 25 μm and larger core monolithic systems impractical, setting the practical limit for monolithic systems to a core size of 20 μm. For free space systems, coiling and single mode excitation are fairly straight forward for 30 μm systems, and it has even been shown that with great effort and skill, a 65 μm system can be operated single mode [7], however free space fiber systems have limited robustness, and are not nearly as compact as their monolithic counterparts, limiting the technological attractiveness of this type of system.

4.4 Beam Propagation Method

The properties of CCC fibers can be determined using numerical methods such as beam propagation [31, 32], which generates numerical solutions of the scaler wave equation (i.e. polarization is neglected) and paraxial approximation (restriction of the propagation angle to a narrow range). The scaler field equation has the form of the familiar Helmholz equation for monochromatic waves

$$\frac{\partial^2\phi}{\partial^2 x}+\frac{\partial^2\phi}{\partial^2 y}+\frac{\partial^2\phi}{\partial^2 z}+k(x,y,z)^2\phi=0 \tag{4.19}$$

where $E(x,y,z)=\phi(x,y,z)e^{-i\omega t}$. By factoring out the rapidly varying phase ($\phi = ue^{i\bar{k}z}$) so that we can make the slowly varying envelope approximation (SVEA), we get a modified Helmholz equation

$$\frac{\partial^2 u}{\partial^2 z}+2i\bar{k}\frac{\partial u}{\partial z}+\frac{\partial^2 u}{\partial^2 x}+\frac{\partial^2 u}{\partial^2 y}+(k^2-\bar{k}^2)u=0 \tag{4.20}$$

where $\bar{k}$ is the average phase variation of the field ϕ. Now the SVEA can be made, and we obtain the following result.

$$\frac{\partial u}{\partial z} = \frac{i}{2\bar{k}}\left(\frac{\partial^2 u}{\partial^2 x} + \frac{\partial^2 u}{\partial^2 y} + (k^2 - \bar{k}^2)u\right) \tag{4.21}$$

Equation 4.21 is the basic BPM equation in three dimensions, and is most commonly solved by a finite difference method (which is known as the FD-BPM), as computational time scales linearly with the number of points. Though this method of solution allows rapid numerical solution for a dielectric waveguide, with a longitudinal step size much larger than the wavelength of light, the problems approximated by this method are limited by the SVEA to structures where the refractive index changes slowly on the scale of the wavelength of light, and where the light propagates in a narrow range of angles along the z-direction from the paraxial approximation. Also, with the second derivative with respect to z neglected, backward scattering cannot be included. Detailed results from the FD-BPM will be given for the CCC structures used in this thesis in the next chapter.

4.5 Numerical methods for the investigation of laser and amplifier performance

The performance of fiber amplifiers and lasers can be investigated by numerical solution of the coupled rate equations for the excited state population, N_2, signal power, $P^{\pm}$ ("+" for forward, and "−" backward), and pump power, P_p, which are

$$\begin{aligned}\frac{\partial N_2(z,t)}{\partial t} &= \left(\frac{\lambda_p \Gamma_p \sigma_p}{hcA}\right) P_p(z,t)[N - N_2(z,t)] - \frac{N_2(z,t)}{\tau} \\ &\quad - \left(\frac{\Gamma_s}{hcA}\right) N_2(z,t) \int \sigma_e(\lambda)[P^+(z,t,\lambda) + P^-(z,t,\lambda)]\lambda d\lambda \\ &\quad + \left(\frac{\Gamma_s}{hcA}\right) [N - N_2(z,t)] \int \sigma_a(\lambda)[P^+(z,t,\lambda) + P^-(z,t,\lambda)]\lambda d\lambda\end{aligned} \tag{4.22}$$

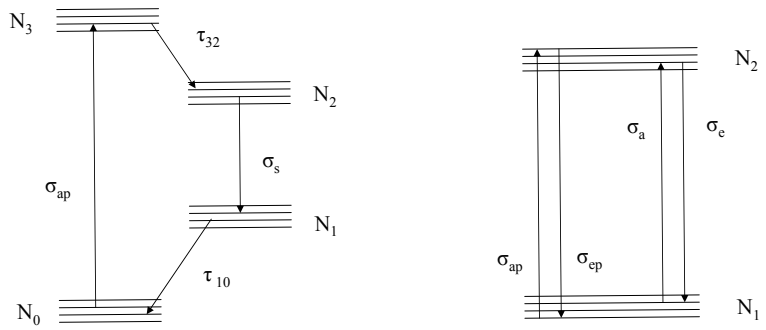

Figure 4.4: Energy level diagram for a laser or amplifier. A four level system is shown on the left, and an Yb type system on the right, where the system operates quasi four level (4 level above $\sim$ 1030 nm, and 3 level below).

$$\begin{aligned}\frac{\partial P^{\pm}(z,t,\lambda)}{\partial z} &= \Gamma_s\{\sigma_e(\lambda)N_2(z,t) - \sigma_a(\lambda)[N - N_2(z,t)]\}P_p^{\pm}(z,t) \\ &\quad +\Gamma_s\sigma_e(\lambda)N_2(z,t)P_0(\lambda) - \alpha(\lambda)P^{\pm}(z,t,\lambda) \qquad (4.23)\end{aligned}$$

$$\begin{aligned}\frac{\partial P_p(z,t)}{\partial z} &= -\Gamma_p\{\sigma_p[N - N_2(z,t)] + \sigma_{24}(\lambda_p)N_2(z,t)\}P_p^{\pm}(z,t) \\ &\quad -\alpha(\lambda_p)P_p^{\pm}(z,t) \qquad (4.24)\end{aligned}$$

where the variables are defined in Table 4.5 for a 35 μm core 200 μm double clad fiber.

These equations form the basis of numerical investigations for both amplifiers and lasers. However, time independent steady state analytic or quasi-analytical approximate solutions are known for strongly pumped amplifiers [33, 34] and lasers

Variable	Description	Value for Simulations	units
N	ion concentration		m^{-3}
N_2	excited state population		m^{-3}
P_p	pump power		W
$P^{\pm}$	signal power		W
Γ_p	pump overlap with core	0.019	
Γ_s	signal overlap with core	0.64	
λ_p	pump wavelength	915 or 975	nm
λ_s	signal wavelength	1064	nm
$\alpha(\lambda)$	signal scattering loss		m^{-1}
$\sigma_e(\lambda)$	signal emission cross section		m^2
$\sigma_a(\lambda)$	signal absorbtion cross section		m^2
σ_p	pump absorption cross section	0	m^2
σ_{es}	signal emission cross section	$0.34e-24$	m^2
σ_{as}	signal absorbtion cross section	0	m^2
σ_{24}	excited state absorption cross section	0	m^2
τ	relaxation lifetime	0.7	ms
σ_{ap}	pump absorption cross section at 915	0.133×10^{-24}	m^2
σ_{ep}	pump emission cross section at 915	1.0×10^{-27}	m^2
σ_{ap}	pump absorption cross section at 975	1.5×10^{-24}	m^2
σ_{ep}	pump emission cross section at 975	1.8×10^{-24}	m^2
$\alpha(\lambda_p)$	pump scattering loss		m^{-1}

Table 4.2: Explanation of variables used in equations 4.22, 4.23, and 4.24. Values used for numerical solution to equations

[35], which are substantially simpler from a computational point of view than the full rate equations given above. For an amplifier, the requirement to use these simplified solutions is a large signal and that amplified spontaneous emission (ASE) is negligible. So, when the system is operated within the regime where the approximations are valid, as is the case for the systems studied here, these analytical or quasi-analytical solutions will be used.

4.5.1 Analytical and quasi-analytical solutions for amplification

For an amplifier, the analytical solutions for the co-propagating geometry where the pump and signal are injected at the same end of the fiber are

$$P_s^+(z) \cong P_s^+(0) exp[-Rz/(1-q)]\phi(z) \tag{4.25}$$

for the signal and

$$P_p(z) \cong P_p(0) \left(\frac{P_s^+(z)}{P_s^+(0)}\right)^q e^{-Rz} \tag{4.26}$$

for the pump, where $\phi(z)$ is a solution of

$$\phi(z)^{1-q} \left| \frac{1 - B_3/B_4}{1 - (B_3/B_4)\phi(z)^{1-q}} \right|^{\left(1+\frac{B_2 B_4}{B_4}\right)} = e^{B_4(1-q)z} \tag{4.27}$$

with R, q, B_2, B_3, and B_4 defined below.

$$q = \frac{\Gamma_p[\sigma_{ap} + \sigma_{ep} - \sigma_{24}(\lambda_p)]}{\Gamma_s[\sigma_{es} + \sigma_{as}]} \tag{4.28}$$

$$R = \Gamma_p \sigma_{ap} N - \alpha_p - [\Gamma_s \sigma_{as} N + \alpha_s] q \tag{4.29}$$

$$B_2 = \frac{\lambda_s \Gamma_s[\sigma_{es} + \sigma_{as}]}{\Gamma_p \sigma_{ap} \lambda_p} \frac{P_s^+(0)}{P_p(0)} \frac{1}{1 + \frac{\sigma_{ep}}{\sigma_{ap}}} \tag{4.30}$$

$$B_3 = \left(\alpha_s - \frac{R}{1-q}\right) B_2 \tag{4.31}$$

$$B_4 = \frac{\Gamma_s \sigma_{es} N}{1 + \frac{\sigma_{ep}}{\sigma_{ap}}} + \frac{R}{1-q} - \alpha_s \tag{4.32}$$

A similar set of solutions is obtained for the counter-propagating amplifier equation where the pump and signal are injected on opposite ends of the fiber, with the signal being

$$P_s^-(z) \cong P_s^+(0) exp[R(L-z)/(1+q)]\hat{\phi}(L-z) \tag{4.33}$$

and the pump is

$$P_p(z) \cong P_p(0) \left(\frac{P_s^-(z)}{P_s^-(0)}\right)^q e^{-Rz} \tag{4.34}$$

where $\zeta = L - z$, and $\hat{\phi}$ is a solution of

$$\hat{\phi}(\zeta)^{1-q} \left| \frac{1 - C_3/C_4}{1 - (C_3/C_4)\hat{\phi}(\zeta)^{1-q}} \right|^{\left(1+\frac{C_2 C_4}{C_4}\right)} = e^{C_4(1-q)z} \tag{4.35}$$

with C_2, C_3, and C_4 as defined below.

$$C_2 = \frac{\lambda_s \Gamma_s [\sigma_{es} + \sigma_{as}]}{\Gamma_p \sigma_{ap} \lambda_p} \frac{P_s^-(L)}{P_p(L)} \frac{1}{1 + \frac{\sigma_{ep}}{\sigma_{ap}}} \tag{4.36}$$

$$C_3 = \left(\alpha_s - \frac{R}{1+q}\right) C_2 \tag{4.37}$$

$$C_4 = \frac{\Gamma_s \sigma_{es} N}{1 + \frac{\sigma_{ep}}{\sigma_{ap}}} + \frac{R}{1+q} - \alpha_s \tag{4.38}$$

Though the equations governing $\phi(z)$ and $\hat{\phi}(z)$ have a closed form it is still necessary to determine values for $\phi(z)$ and $\hat{\phi}(z)$ by numerical means. Figure 4.5 shows the result of a counter-propagating amplifier, with a 1W seed at 1064 nm, 975 nm pumping of a 5m amplifier, and N set such that 99 % of the pump power is absorbed, and alpha is either 0 or 5 dB of total absorption. Similar results are shown for the co-propagating configuration in Figure 4.6.

4.5.2 Analytical and quasi-analytical solutions for laser performance

For a laser [35], which has the restriction of a negligible pump emission cross section (i.e. $\sigma_{ep} \cong 0$) and $\alpha_s = 0$ as well as the restrictions imposed for the amplifier as described above, an analytical approximation to the solution is known. However

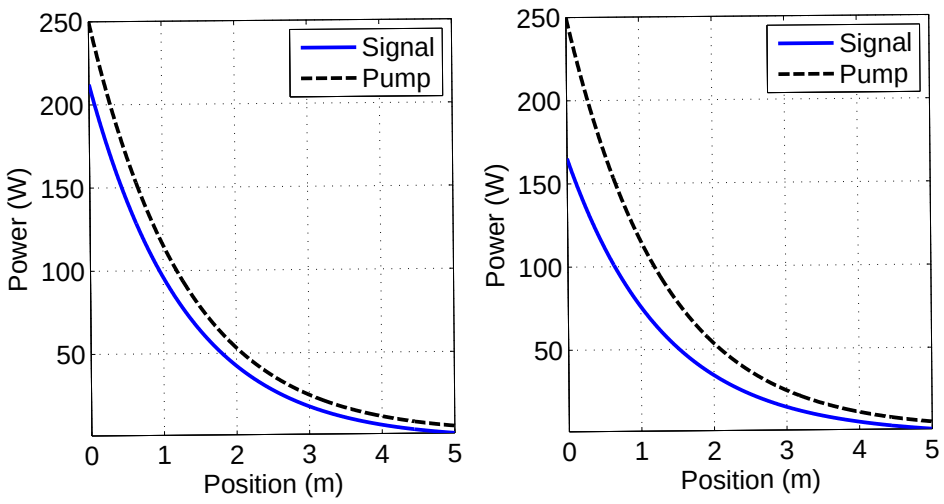

Figure 4.5: 5m amplifier seeded with a 1W 1064 nm seed pumped at 915 nm in the counter-propagating geometry, with total loss of 0 dB (left) and 5 dB (right)

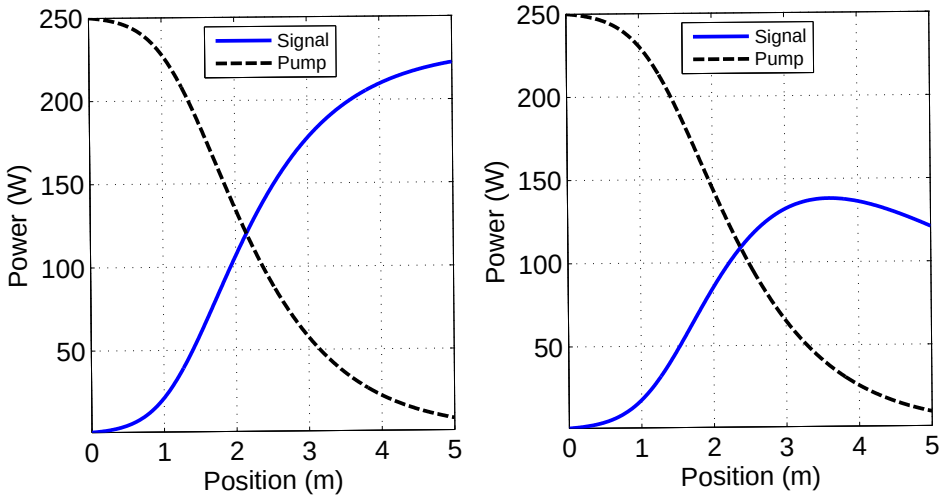

Figure 4.6: 5m amplifier seeded with a 1W 1064 nm seed pumped at 975nm in the co-propagating geometry, with total loss of 0 dB (left) and 5 dB (right)

the primary interest in this work is to investigate the behavior of a laser where $\alpha_s \neq 0$ as well as pumping the laser at 915 nm or 975 nm, the later of which has non-negligible pump emission cross section (i.e. $\sigma_{ep} \neq 0$), and it is the inclusion of $\sigma_{ep} \neq 0$ which requires a novel derivation of the quasi-analytic solution given below. The starting point for solutions is the same set of equations as for the amplifier, in which the time dependance is explicitly removed so that the equations can be rewritten as

$$\frac{N_2(z)}{N} = \frac{\frac{(P_p^+(z)+P_p^-(z))\sigma_{ap}\Gamma_p}{h\nu_p A} + \frac{\Gamma_s}{hcA}\int \sigma_a(\lambda)[P^+(z,\lambda)+P^-(z,\lambda)]\lambda d\lambda}{\frac{(P_p^+(z)+P_p^-(z))(\sigma_{ap}+\sigma_{ep})\Gamma_p}{h\nu_p A} + \frac{1}{\tau} + \frac{\Gamma_s}{hcA}\int(\sigma_e(\lambda)+\sigma_a(\lambda))[P^+(z,\lambda)+P^-(z,\lambda)]\lambda d\lambda} \tag{4.39}$$

$$\pm\frac{dP_p^{\pm}(z)}{dz} = -\Gamma_p\{\sigma_{ap}N + [\sigma_{24}-(\sigma_{ap}+\sigma_{ep})]N_2(z)\}P_p^{\pm}(z) - \alpha(z,\lambda_p)P_p^{\pm}(z) \tag{4.40}$$

$$\begin{aligned}\pm\frac{dP^{\pm}(z,\lambda)}{dz} &= \Gamma_s[(\sigma_e(\lambda)+\sigma_a(\lambda))N_2(z) - \sigma_a(\lambda)N]P^{\pm}(z,\lambda) \\ &\quad +\Gamma_s\sigma_e(\lambda)N_2(z)P_0(\lambda) - \alpha(z,\lambda)P^{\pm}(z,\lambda)\end{aligned} \tag{4.41}$$

with the parameters as shown in Table 4.5 for a 35 μm core 200 μm double clad fiber. Restricting pumping to one end, and noting that the reflected pump is negligible at the unpumped end of the fiber unless special measures are teken, the pump power can be described by $P_p(z)$ rather than the more complex $P_p^+(z)+P_p^-(z)$ and substituting $P^{\pm}(z,\lambda) = P_s^{\pm}(z)\delta(\lambda-\lambda_s)$ and integrating equation 4.39 yields

$$\frac{N_2(z)}{N} = \frac{\frac{P_p(z)\sigma_{ap}\Gamma_p}{h\nu_p A} + \frac{\Gamma_s}{h\nu_s A}\sigma_{as}[P_s^+(z)+P_s^-(z)]}{\frac{P_p(z)(\sigma_{ap}+\sigma_{ep})\Gamma_p}{h\nu_p A} + \frac{1}{\tau} + \frac{\Gamma_s}{h\nu_s A}(\sigma_{ap}+\sigma_{ep})[P_s^+(z)+P_s^-(z)]} \tag{4.42}$$

which after multiplying both sides by $\Gamma_s\sigma_{es}$ and substituting $P_{sat} = \frac{h\nu_s A}{\Gamma_s\sigma_{es}\tau}$ results in

$$N_2(z)\Gamma_s\sigma_{es} = \frac{\frac{NP_p(z)\sigma_{ap}\Gamma_p}{(\nu_p/\nu_s)P_{sat}} + \Gamma_s\sigma_{as}\frac{P_s^+(z)+P_s^-(z)}{P_{sat}}}{1 - \frac{P_p(z)\Gamma_p\tau}{h\nu_p A}(\sigma_{ap}+\sigma_{ep}) + \frac{P_s^+(z)+P_s^-(z)}{P_{sat}}} \tag{4.43}$$

Gain is defined in the usual manner to be

$$g_s(z) = \Gamma_s\sigma_{es}N_2 + \Gamma_s\sigma_{as}N \tag{4.44}$$

where the first term is equation 4.43, which when substituted into equation 4.41 gives the following differential equation governing signal behavior in the fiber.

$$\frac{dP_s^{\pm}(z)}{dz} = [g_s(z) - \alpha_s]P_s^{\pm}(z) \tag{4.45}$$

Defining $\psi(z)$ and B to be

$$\psi(z) = \frac{P_s^{+}(z) - P_s^{-}(z)}{P_{sat}} \tag{4.46}$$

and

$$B = \frac{2\sqrt{P_s^{+}(z)P_s^{+}(z)}}{P_{sat}} \tag{4.47}$$

repsectively, and substituting into equation 4.45 generates a differential equation in terms of the dimensionless variable $\psi(z)$

$$\frac{d\psi(z)}{dz} = \left(\frac{g_0'(z)}{1 + \frac{P_p(z)\Gamma_p\tau}{h\nu_p A}(\sigma_{ap} + \sigma_{ep}) + \sqrt{\psi(z)^2 + B^2}} - \alpha_s \right) \sqrt{\psi(z)^2 + B^2} \tag{4.48}$$

where $g_0'(z)$ is

$$g_0'(z) = \frac{NP_p(z)\sigma_{ap}\Gamma_p}{(\nu_p/\nu_s)P_{sat}} - \sigma_{as}\Gamma_s N(1 + \frac{P_p(z)\Gamma_p\tau}{h\nu_p A}(\sigma_{ap} + \sigma_{ep}) \tag{4.49}$$

which is numerically integrable, and subject to the boundary condition

$$\psi(L) = \frac{[1 - R_2]\sqrt{R_1}}{[1 - R_1]\sqrt{R_2}}\psi(0) \tag{4.50}$$

where R_1 and R_2 are the power reflectivity coefficients of the left and right end of the laser cavity, with the pump being from the left end. The solutions for co-propagating (pump and signal extraction from opposite ends of the laser) and counter-propagating (pump and signal extraction from the same end of the laser) are shown in Figure 4.7 and 4.8 respectively.

If the pump emission cross section is negligible an approximate analytical solution exist [35], and the differential equation for $\psi(z)$ becomes

$$\frac{d\psi(z)}{dz} = \left[\frac{g_0(z)}{1 + \sqrt{\psi^2(z) + B^2}} - \alpha_s \right] \sqrt{\psi^2(z) + B^2} \tag{4.51}$$

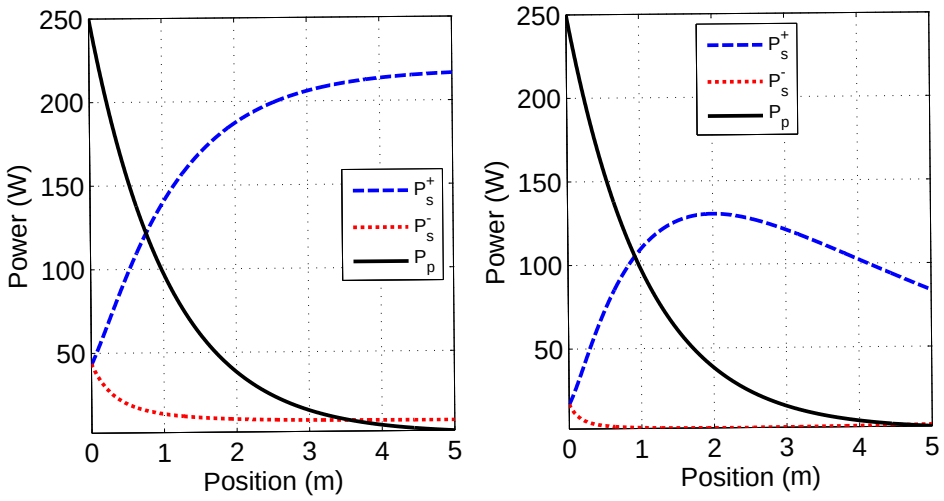

Figure 4.7: 5m laser operating at 1064 nm and pumped at 915 nm in the counter-propagating geometry, with total loss of 0 dB (left) and 5 dB (right)

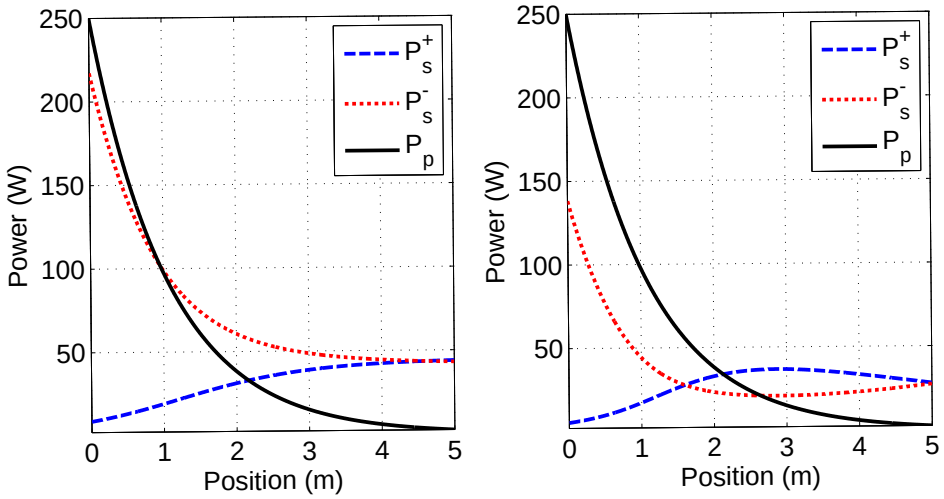

Figure 4.8: 5m laser operating at 1064 nm and pumped at 915 nm in the co-propagating geometry, with total loss of 0 dB (left) and 5 dB (right)

where $g_0(z)$ is

$$g_0 = \frac{N\Gamma_p\sigma_{ap}P_p(z)}{(\nu_p/\nu_s)P_{sat}} - N\Gamma_s\sigma_{as} \tag{4.52}$$

, which unless otherwise noted, the terms for the analytical result have the same definitions as for the quasi-analytic result given above for non-negligible pump emission cross section. If the signal absorption is zero, then 4.51 is integrable and the pump and signal are

$$P_p(z) \cong P_p(0)exp[-(\Gamma_p\sigma_{ap}N + \alpha_p)z] \tag{4.53}$$

and

$$P_s^{\pm}(z) = \frac{1}{2}P_{sat}\left(\sqrt{\psi^2(z) + B^2} \pm \psi(z)\right) \tag{4.54}$$

respectively.

4.6 Concluding remarks

With the background material covered, it is time to move on to the design process and then to the experimental and theoretical results. The next chapter will detail the results achieved and establish the success of the CCC design as an ESM fiber, as well as gauging the potential for building kW regime systems.

CHAPTER V

Effectively Single-Mode Chirally Coupled Core Yb-doped Fiber Lasers and Amplifiers for High Power Scaling

5.1 Introduction

Fiber lasers with multi-kW average [29] and multi-MW peak [30], powers in diffraction-limited output beams have been recently demonstrated using so called Large-Mode Area (LMA) fibers, in which single-mode operation is achieved in a multimode core (typically 20 μm to 30 μm diameter, with 65 μm to 80 μm being state of the art demonstrations [30]) by employing careful mode-management [36, 37], Such an approach has limited robustness and can not be monolithically integrated for LMA fibers with core sizes exceeding $\sim$25 μm, thus offsetting many traditional technological advantages of conventional single-mode fiber technology and hindering development of power scalable all-fiber large-core fiber laser systems.

In order to overcome this bottleneck, higher order mode suppression based on the fiber structure itself, rather than external factors has been proposed and demonstrated [2], which will enable the construction of complex monolithic systems with core sizes far beyond the current 25 μm limits. The design of an effectively-single-mode (ESM) large mode area fiber is based on the chirally-coupled-core (CCC) structure. Such fibers permit mode-distortion-free splicing and compact coiling (below 15 cm coiling radius) thus enabling next generation all-fiber high power optical systems.

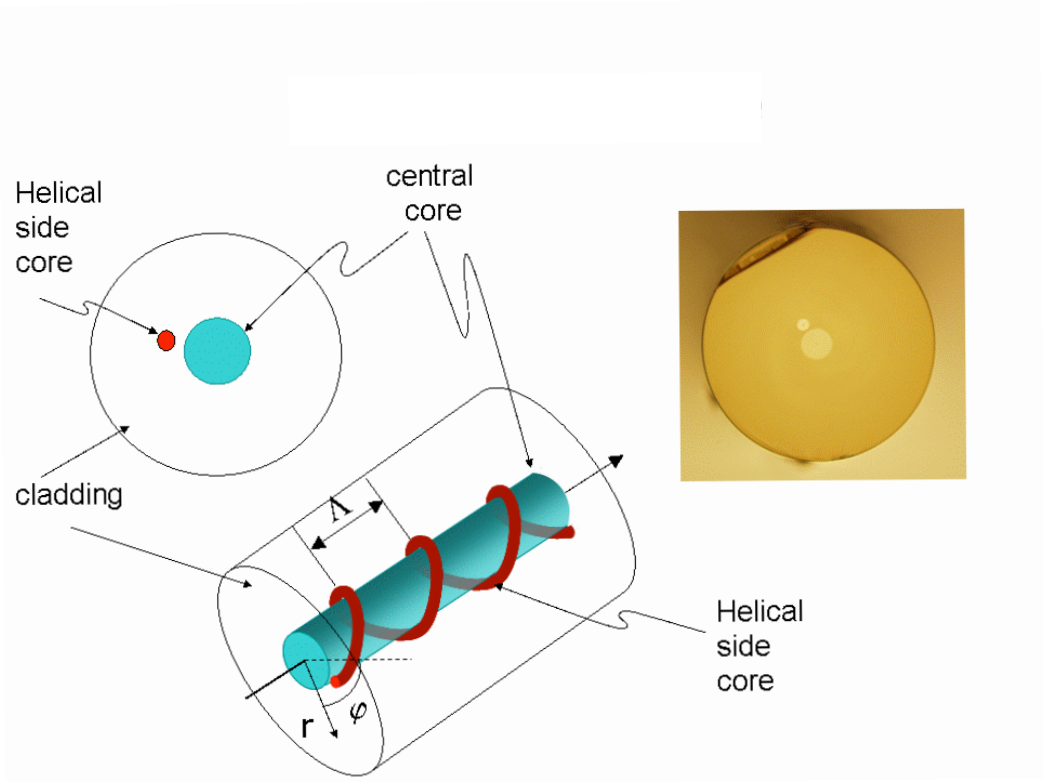

Figure 5.1: Chirally coupled core fiber schematic, and an image of a fiber end

However, the first CCC demonstrations have been achieved with undoped (passive) fibers. In this chapter the development of the first Yb-doped (active) CCC fibers is presented. To begin with, the techniques for the design of CCC fibers are outlined, and examples are shown to give insight into the design parameters available. Next, the measured performance of both laser and amplifier systems are compared to the theoretical models developed in the previous chapter. Finally, fiber designs currently undergoing testing and future directions for research are discussed.

5.2 Effectively single mode fibers

For high power systems, the active components of a system are typically 10-20 m in length for thermal management reasons, while passive components are typically pig-tailed with 1-2 m of fiber. A pig-tailed component, such as a spectral filter, requires light to exit the fiber, propagate through the dielectric coated filter, and re-couple into another fiber lead fiber, each component of which is rigidly fixed in a holding body, with micro-lenses on the ends of the fibers to facilitate coupling. The length scales for active and passive components set the target for HOM suppression.

With this in mind, the benefits of greater HOM suppression in an effectively-single-mode-fiber (ESM) will be highlighted. The most important benefit of greater HOM suppression are increased robustness of the system to perturbation. To understand this, the residual power in the HOMs as light propagates along an ESM fiber was calculated with BPM, the results of which are shown in Figure 5.2 for several attenuation rates. For the lowest suppression considered, 10 dB/m, the fiber length required to eliminate HOMs from propagating in the fiber is on the order of several meters, which is fine for the long active components, however for passive components, the length required for HOM suppression is greater than the 1-2 m of

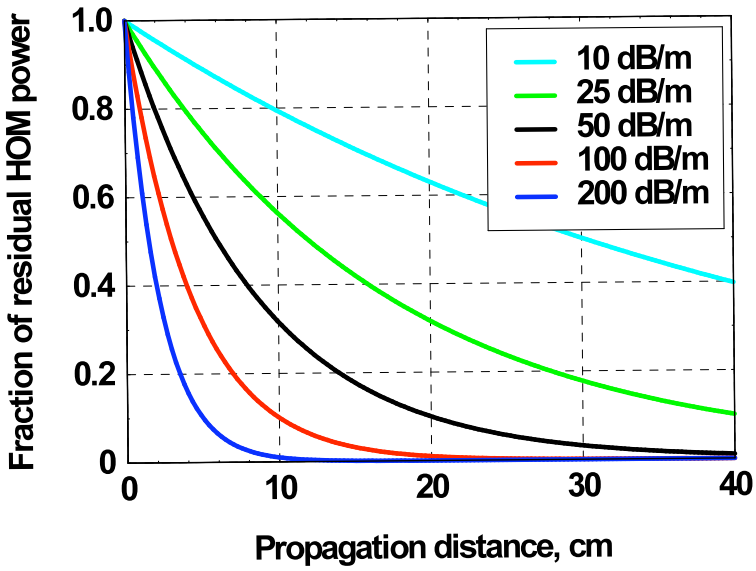

Figure 5.2: Determination of requirements for higher order mode suppression

pig-tailed fiber, and so monolithic systems cannot be constructed with such weak HOM suppression. Moving the target up to 25 dB/m allows monolithic integration of the system, with limited robustness. For 50 dB/m, monolithic systems are starting to exhibit robust performance. However, it is in the range of 100-200 dB/m where only a few tens of cm are sufficient to extract virtually all HOM content from the fiber, and it is with this level of HOM suppression where the ESM fiber becomes essentially indistinguishable from truly single mode fiber, requiring only a few cm to produce distortion free near diffraction limited output.

5.3 CCC design

The CCC structure has both a central and side core, with the latter helically spun about the former with a period Λ as shown in Figure 5.1. The structure is designed such that only higher order modes, and not the fundamental, couple from

the central to the side core. The power once coupled from the central into the side core is then radiated from the fiber via bend-induced loss. The net result is an effectively single mode fiber capable of outputting near diffraction limited beams independent of excitation or coiling conditions.

The optimal fiber designs were determined by numerical investigation using beam propagation method (BPM) which calculates the parameters of the structure such as modal loss, dispersion, and group velocity, within the approximations of the scaler theory as outlined in the previous chapter. As an example, the calculated modal loss as a funcion of helical period and side core NA for the first two modes is shown in Figure 5.4 at 1064 nm, where the target is low loss for LP_{01}, restricting the choice to the red region (< 0.3 dB/m) of the loss map, whereas for LP_{11} the target is high loss, on the order of 100 dB/m or greater, restricting the choice to the blue (~ 100 dB/m) or purple (> 100 dB/m) regions. Notice that there are several possibilities for low fundamental loss and high LP_{11} loss to choose from, and that the regions of interest are islands of low fundamental loss with high HOM loss. Modes higher than LP_{11} are not shown here, however they were calculated, and help determine the optimum design point, though typically LP_{11} is the most challenging mode to mitigate. To give a better idea as to the numerical values typical for a particular set of parameters, a 1D scan of modal loss vs. helix period is shown, where it can be seen that for a helical period in the region of 8.8-9.4 mm the fundamental mode loss is on the order of 0.2 to 0.3 dB/m and HOM losses are nearly 100 dB/m or greater.

To reach a design capable of efficiently extracting all higher order modes from the central core while allowing the fundamental mode to propagate with only small loss it was necessary to adjust more than the parameters shown in the previous two figures. The set of adjustable parameters include the NA of the central and side cores, edge

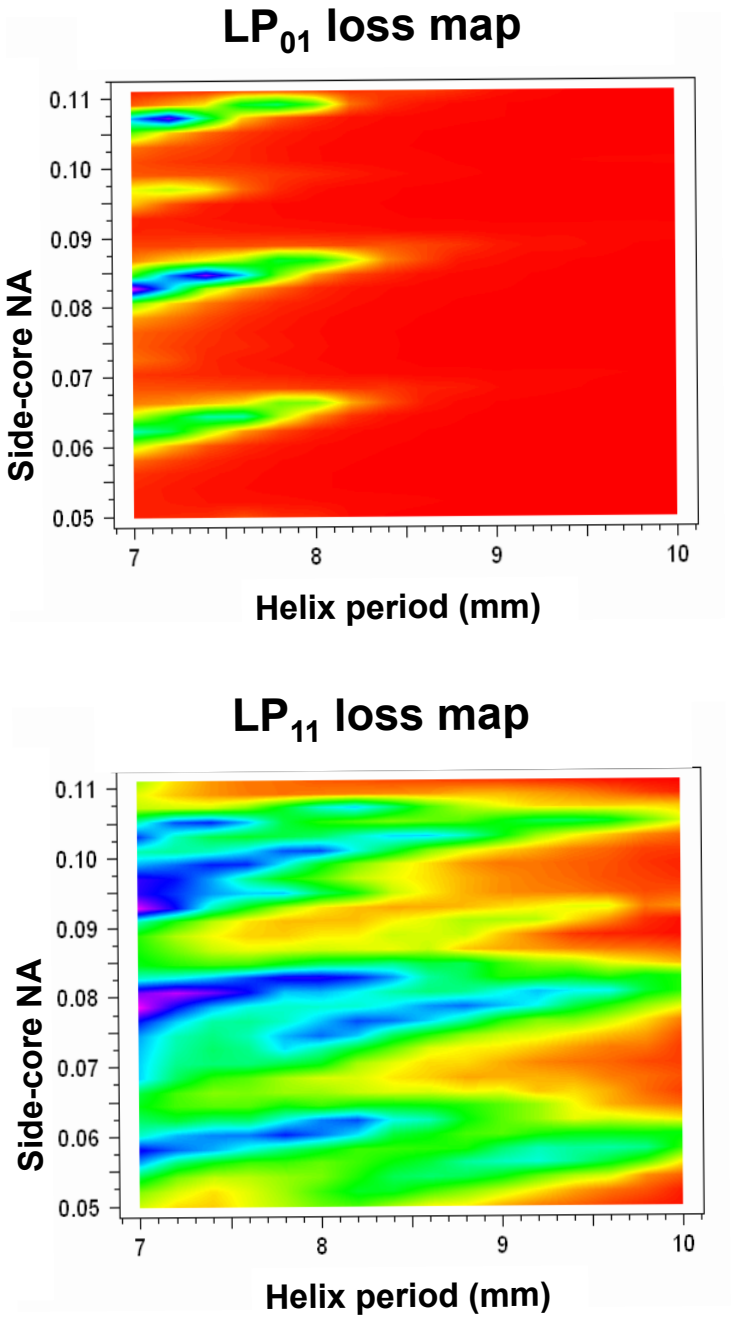

Figure 5.3: Calculated modal loss for a 33 μm core CCC fiber as a function of period and side core NA, with LP_{01} (left) and LP_{11} (right).

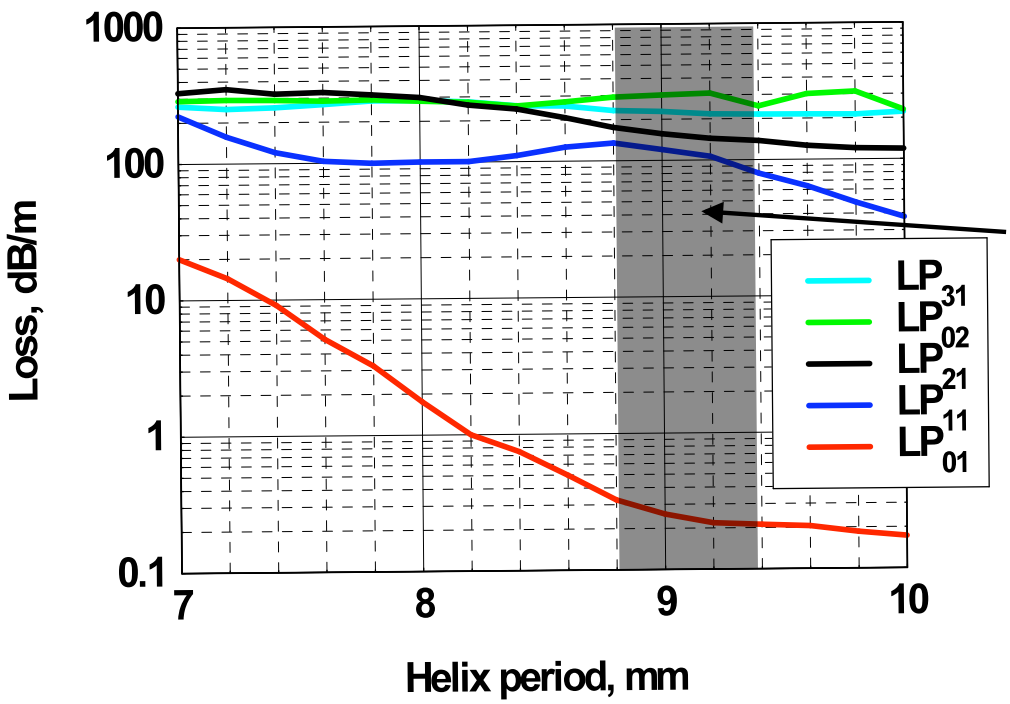

Figure 5.4: Calculated modal loss for a 33 μm core CCC fiber as a function of period

to edge separation of the central and side cores, size of each core and the helical pitch of the side core. Once a design has been determined to both have good performance, and to have that good performance over a reasonable range of parameters (i.e. having tolerance in the design), the specifications are sent to the manufacturer. They then produces a pre-form fiber based on the specifications provided and then send the specifications of the manufactured pre-form back to us. With the specifications such as the ratio of the core sizes fixed, core NAs, etc..., a second set of simulations are run and the pitch of the fiber can be adjusted to optimize the design of the fiber. The adjustments are then sent to the manufacturer who then pulls the pre-form into a fiber of the final design, ensuring good performance of the final product.

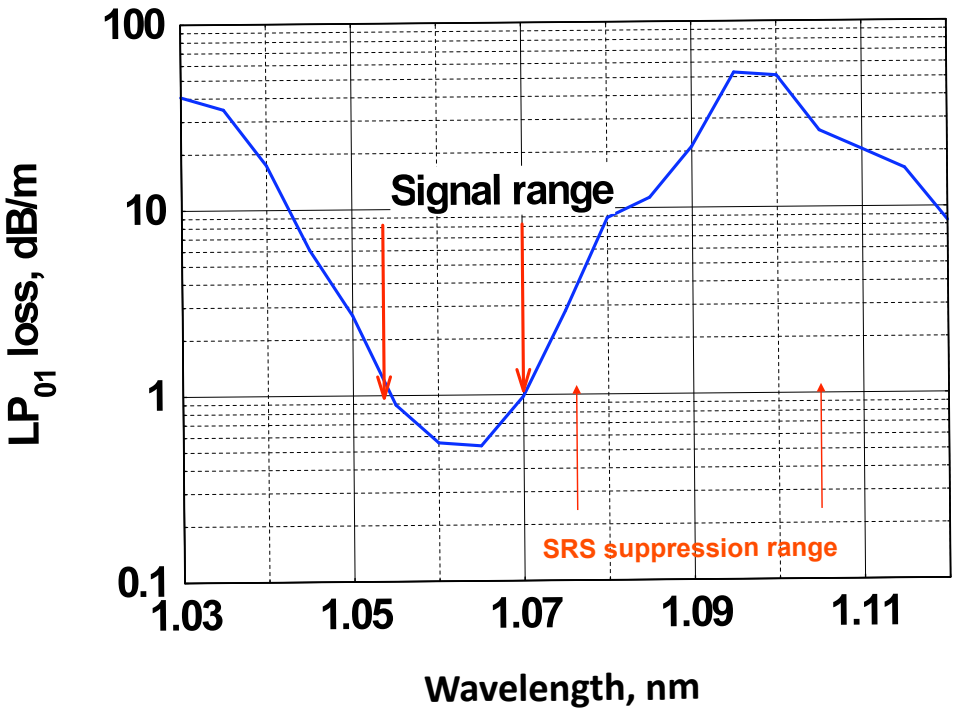

Figure 5.5: Calculated modal loss for a 33 μm core CCC fiber as a function of wavelength. The signal wavelength has reasonable loss, while in the SRS regime, the loss ranges between 3 and 50 dB.

Targeted wavelength dependent loss can be engineered into the CCC structure to suppress stimulated raman scattering (SRS) by choosing suitable parameters which allow HOM suppression at the signal wavelength, 1.064 μm, and fundamental mode loss in the regime of raman scattering regime near 1.1 μm an example of which is shown in Figure 5.5.

5.4 Robust Single Mode Performance from a CCC Fiber Laser

A laser setup was built to investigate the slope efficiency and modal robustness of the laser as well as for power scaling experiments. A five-meter active CCC fiber

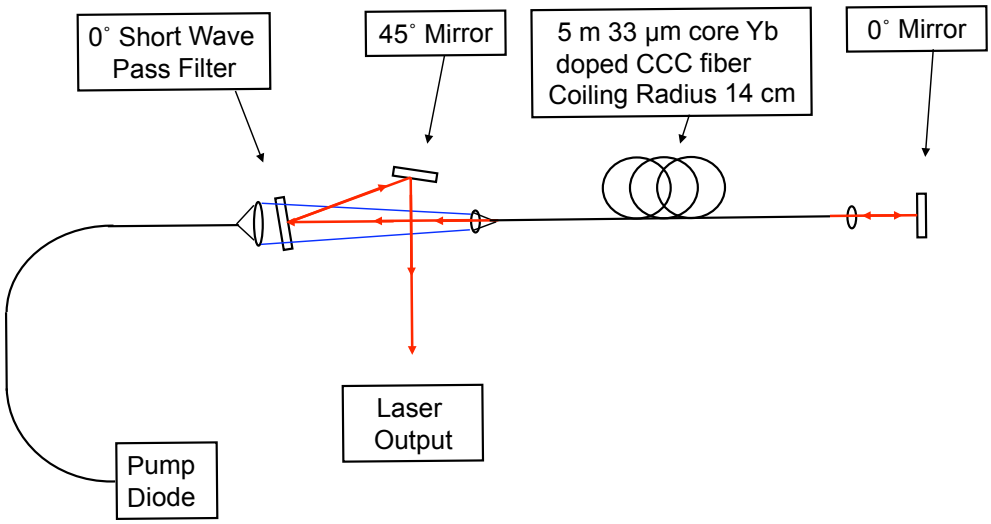

Figure 5.6: Laser setup, with 5 m 33 μm CCC fiber

was set up in a free space laser configuration, as shown in Figure 5.6. No external mode management techniques were used in the setup, and the setup was free space, the latter condition making this a stringent test of CCC fiber as an effectively-single-mode fiber. The experiment used a 5 m CCC fiber with a 33 μm, 0.06 NA central and 16 μm, 0.10 NA side core, which had an edge-to-edge separation of 4 μm and helical period of 7.4 mm. The active fiber is double clad, with 250 μm 0.47 NA outer cladding, with only 47 % of the pump light coupling into the core. The light interacting with the core had an absorption of $\sim$2 dB/m at 915 nm. The pump source was a 220 W, 915 nm pump diode stack delivered via a 600 μm, 0.22 NA fiber to the 250 μm 0.47 NA CCC fiber, which resulted in a low coupling efficiency due

geometrical considerations, which result in a substantial portion of the pump light falling outside of the acceptance angle of the CCC fiber. That this is the case can be seen by recalling the definition of NA, $sin\ \theta_{NA} = NA$, where θ_{NA} is the maximum angle of incidence for which light will be guided by total internal reflection, and noting that when the output light from the 600 μm pump fiber is focused down to a size of $\sim$250 μm, light will be incident at an angle greater than the 0.47 NA fiber can accept and a portion of the pump light will not be captured by the double clad Yb-doped fiber, a condition known as overfilling. The coupling optics were an 8 mm aspheric and 19 mm spherical lens separated by 17 cm, which gave optimal coupling efficiency between the delivery and gain fibers, though with the pump substantially overfilling the active fiber only 52.7 % coupling efficiency could be achieved. The maximum pump power interacting with the core is therefore 54 W which severely restricts the total output power of the laser.

Both ends of the active fiber were straight cleaved, and the 5 m segment coiled to a radius of 14 cm. The cavity was formed by the straight cleave near the pumped end, and a short pass filter used as a 0° retroreflector for the signal wavelength at the unpumped end. The pump was protected from ASE as well as the signal by three short pass dielectric filters that were placed between the delivery and active fibers, the one closest to the active fiber having been angled slightly to facilitate signal extraction from the laser.

The measured output power is shown in Figure 5.7 and reached 37 W, the brightness and power of the pump diode being the limiting factors. The threshold and slope efficiency were 6 W and 75 % respectively. The beam profile was single mode and stable at all powers, with the measured beam profile of the highest power shown in the lower right inset of Figure 5.7 and the spectrum in the upper left where the

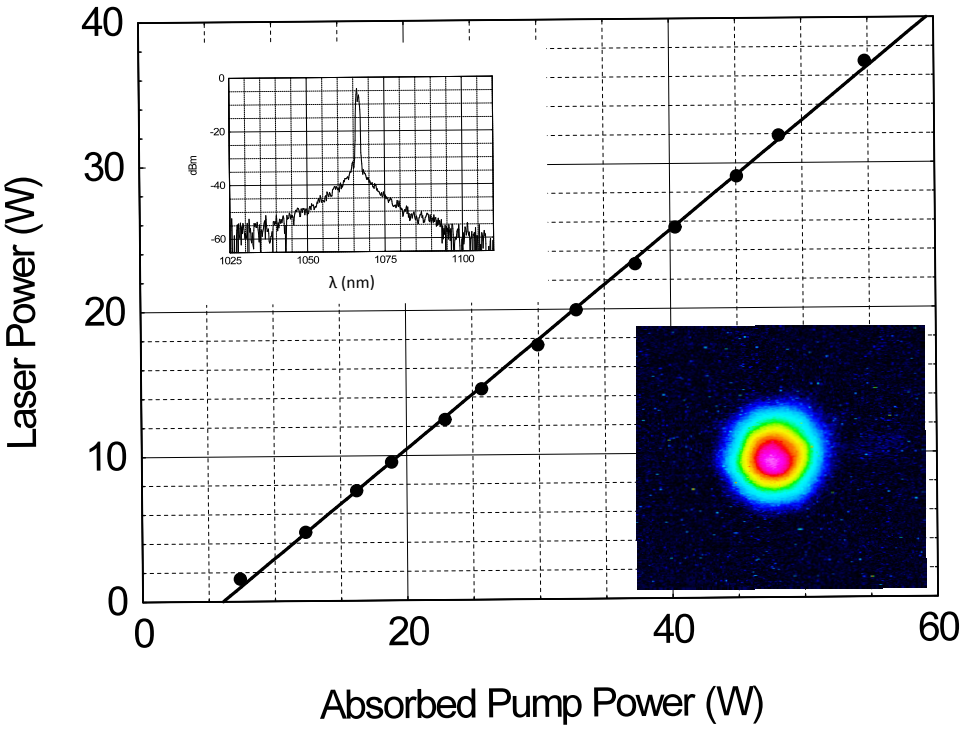

Figure 5.7: Laser performance, spectrum (inset: upper left), and mode field profile (inset: lower right) with 915 nm pump, with a threshold of 6 W and slope efficiency of 75 %.

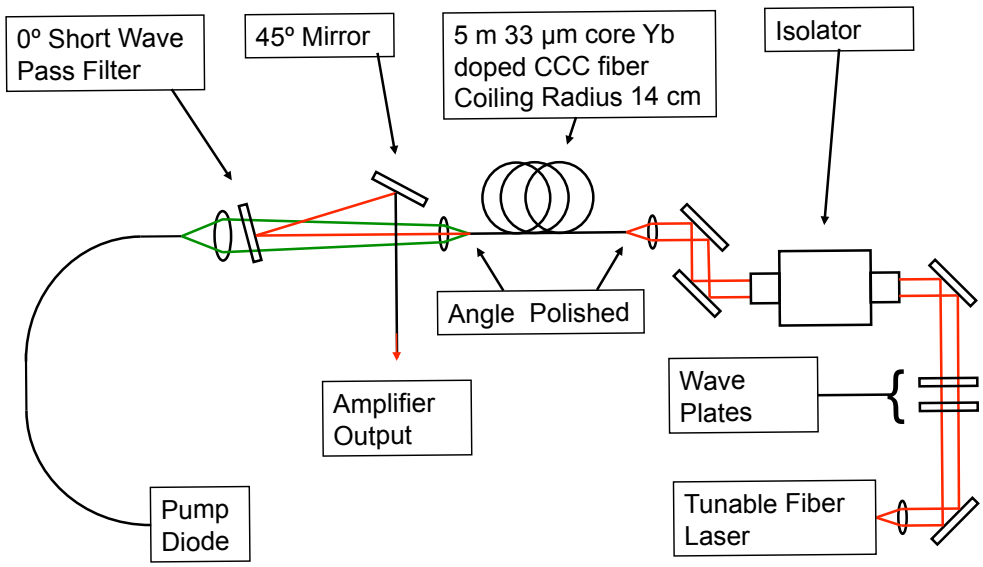

Figure 5.8: Amplifier setup with a tunable fiber laser seed

output has a line width below the resolution of the OSA (0.05 nm) centered at 1066 nm. Thus, the CCC fiber met or surpassed all expectations of performance, with gain characteristics comparable to LMA technology, and the single mode output at all measured powers as well as for small misalignments of the 0° retroreflector as long as the laser was above threshold.

5.5 Gain Characteristics and Power Scaling of CCC in an Amplifier Configuration

To measure the small signal and wavelength dependent gain characteristics, as well as the robustness of the modal output and power scaling ability of CCC fiber an amplifier setup was built as shown in Figure 5.8. To begin with the active fiber

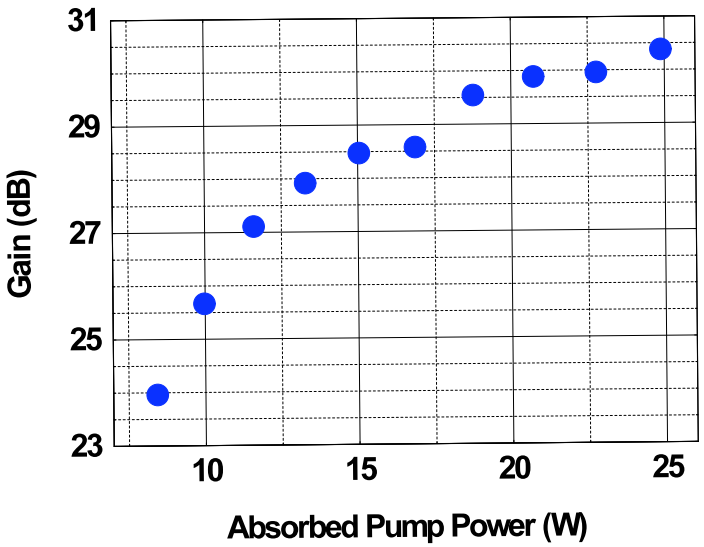

Figure 5.9: Small signal gain at 1064 nm, showing a maximum gain of 30.3 dB.

was prepared by having both ends angle polished to 12° in order to substantially reduce feedback. The small signal characteristics of the amplifier were measured by seeding with a 1 mW seed from a tunable fiber laser, which uses a reflective grating set up in littrow configuration as one end of the cavity for the tunable element. To prevent feedback from the amplification stage, an isolator as well as a quarter and half waveplate were placed between the seed laser and the amplifier. The pumping configuration and signal extraction for the counter propagating amplifier are the same as for the laser described above.

The small signal gain as a function of absorbed pump power and wavelength are shown in Figures 5.9 and 5.10 respectively. For fixed wavelength at 1064 nm, a maximum gain of 30.3 dB was measured, a value in line with that expected for a free space LMA Yb-doped amplifier. The 12° angle polished fiber end attenuates

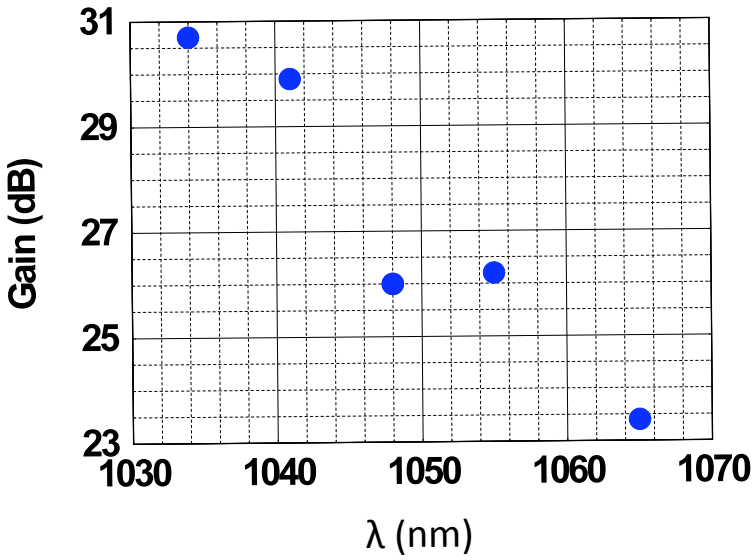

Figure 5.10: Small signal gain as a funciton of wavelength for a 1 mW injected seed with 8 W absorbed pump.

the Fresnel reflection by ∼30 dB, and when the gain is above this attenuation value, lasing begins, which depletes the gain and prevents further increases in small signal gain. This was the limiting factor for the measured small signal gain. Gain as a function of wavelength showed the expected trend with the highest gain at 1030 nm and decreasing gain with increasing wavelength.

Next, power scaling test were begun by adding a single mode pre-amplification stage between the tunable laser and the CCC stage, with a set of waveplates and an isolator inserted before and after the pre-amplifier stage. With this setup an 84 mW seed signal was injected, and the measured output power and spectrum shown in Figure 5.11. The slope efficiency was 54 %, and the maximum output power was 21 W at 1064 nm.

With the arrival of new high brightness diodes further efforts to power scale were

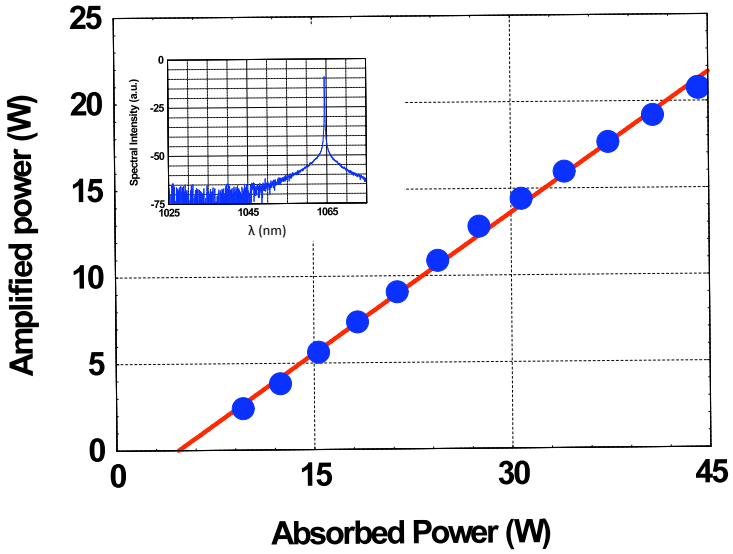

Figure 5.11: Large signal gain with a 84 mW seed at 1064 nm and pumped at 915 nm had a slope efficiency of 54 %.

undertaken. The new diodes operated at a nominal 974 nm, with a maximum output power of 350 W coupled into a 200 μm 0.20 NA delivery fiber. With this shift in pump wavelength, pump absorption will triple to ~6 dB/m, though the high fluence is expected to bleach a partial length of the fiber, not necessitating a reduction in active fiber length. This change in pump brightness required a pair of 25.4 mm lenses separated by 52.6 cm for optimum coupling, which increased the coupling efficiency to 90% now that the delivery fiber is underfilling the 250 μm 0.20 NA clad active fiber. In order to further increase the final output power a 5 m 30 μm Yb-doped amplifier in a counter-propagating configuration was inserted between the single mode pre-amplifier and the 33 μm CCC stage, which after a set of waveplates and an isolator provided a 6 W seed for the final amplification stage. The measured output power is shown in Figure 5.12, with a maximum output of 87 W. The output

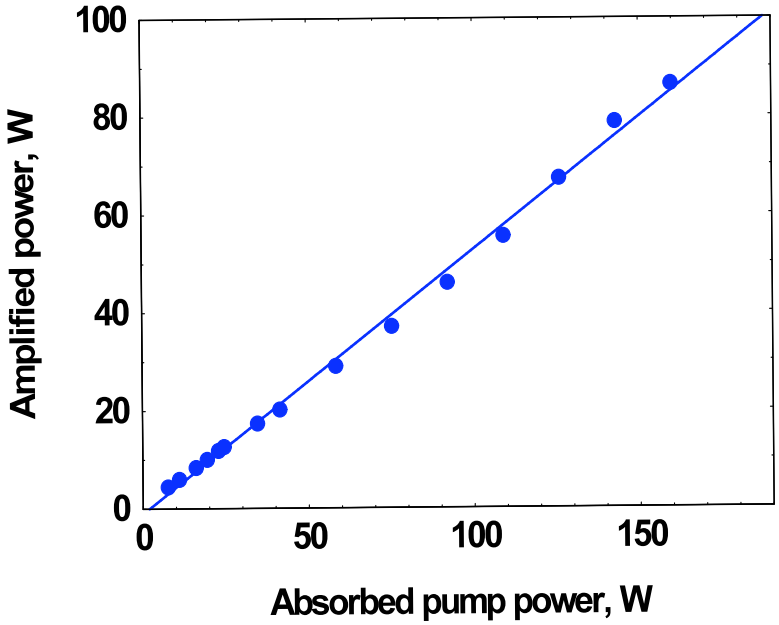

Figure 5.12: Large signal gain with a 6 W seed at 1064 nm and pumped at 974 nm had a slope efficiency of 54 %.

signal was again centered at 1064 nm having a width below the resolution of the OSA used (0.05 nm), and robust single mode output at all measured powers.

5.6 Effect of Fundamental Mode Loss on Efficiency for Lasers and Amplifiers

While the CCC fiber geometry represents a breakthrough in achieving single mode performance from a large mode area fiber that can be coiled and integrated into a monolithic system, the design has a small amount of fundamental mode loss along with high HOM loss. In this and the following subsections, analysis of the effect of loss on the efficiency of lasers and amplifiers is investigated.

Beyond this fundamental question, understanding the loss seen in the specific design point for the fiber tested and comparing the performance predicted by BPM, measured performance, and the performance predicted by the laser and amplifier

models developed in the previous chapter will shed light onto the reliability of the predictions by BPM and the performance of the fiber itself. For the set of simulations below, the Yb-doped fiber characteristics shown in Table 4.5 were used, with the doping concentration artificially adjusted such that the total pump absorption is ∼98 % regardless of the fiber length to facilitate the comparison of different lengths of fiber, with the same pump absorption and fundamental mode loss from the signal.

5.6.1 Experimental Laser Analysis

The slope efficiency of a 33 μm core 5 m laser with 915 nm pumping, operating at 1064 nm was calculated as a function of fundamental mode loss, for the counter-propagating configuration (pump and signal extraction from the same fiber end), and is shown in Figure 5.13, which corresponds to the configuration of the laser as shown previously in Figure 5.6. With a measured slope efficiency of 75%, the theoretical model predicts a total loss of ∼1 dB, or a unit loss of 0.2 dB/m, as determined from Figure 5.13, which is well in line with that predicted by BPM.

5.6.2 Comparing the Counter-propagating and Co-propagating Configurations for a Fiber Laser with Loss

The counter-propagating and co-propagating power as a function of length are compared first with $\alpha_s = 0$ dB and then at $\alpha_s = 5$ dB in Figure 5.14. For this particular set of parameters, notice that both configurations where $\alpha_s = 0$ dB have similar output powers of slightly over 40 W, while when $\alpha_s = 5$ dB the co-propagating laser behaves substantially worse than the counter-propagating configuration. The co-propagating configuration is more sensitive to modal loss than the counter-propagating configuration, and when loss is present there is an optimal length. Moreover, even if the optimal length of 2.01 m had been selected, the

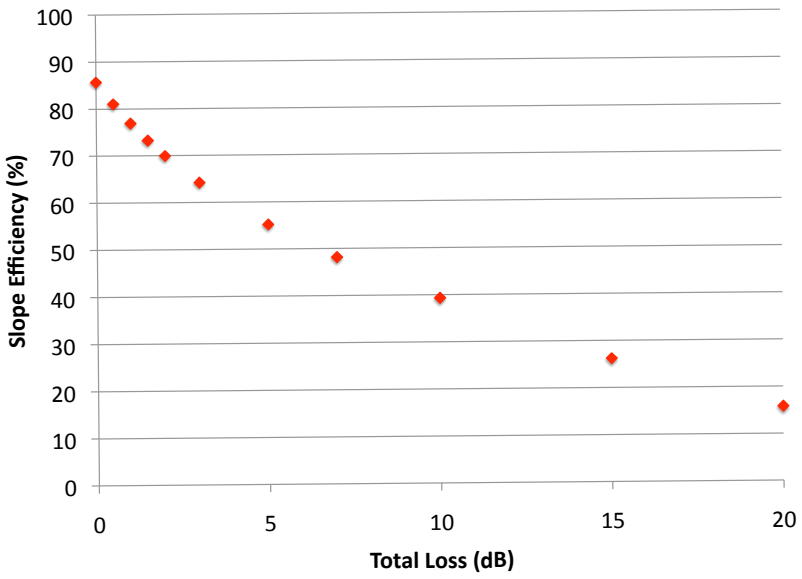

Figure 5.13: Slope efficiency as a function of fundamental mode loss as calculated from theoretical model for counter-propagating laser configuration for 5m 915 nm pumped laser operating at 1066 nm.

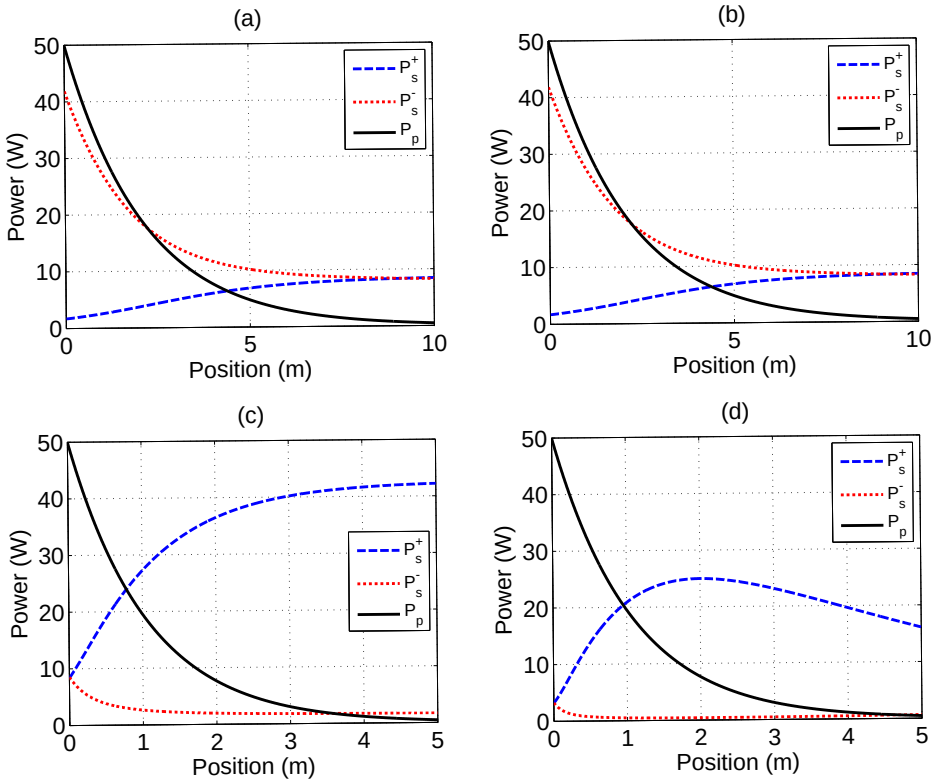

Figure 5.14: Power as a function of length for both the counter-propagating (‘a’ and ‘b’) and the co-propagating (‘c’ and ‘d’) configuration for a 5 m laser pumped at 915 nm operating at 1064 nm. The left most figures (‘’a and ‘c’) have no signal loss, and the right most (’b‘ and ’d‘) have a total loss of 5 dB

maximum output would have been ∼25 W compared to ∼42 W for the counter-propagating case. This is due to pump depletion when the signal is largest in the co-propagating configuration, and is the reason a laser should be setup in the counter-propagating configuration. Finally, it should be noted that this effect could be mitigated by decreasing the length of the fiber in order to allow more pump through to 2.01 m, and thereby allowing for more pump power at the output end, however this would be an inefficient use of the available pump power, with ∼7 W of the available 50 W wasted as pump through, and is therefore not done.

5.6.3 Comparing Efficiencies for 915 nm and 974 nm Pumping for a Counter-propagating Laser Configuration

With higher brightness pump diodes that operate at a nominal 974 nm now available for power scaling experiments, the next generation of experiments will be pumped with these high brightness diodes, so it is instructive to compare predicted performance at 974 nm to 915 nm for the same counter-propagating laser configuration as shown in Figure 5.15. It is clearly evident from the figure that the a laser pumped at 915 nm is ∼10-15 % more efficient than one operated at 915 nm. While pumping at 915 nm is more efficient, there are two advantages to pumping at the longer wavelength. First, the pump absorption is three times higher at the longer wavelength allowing for shorter fiber lengths, and second, the highest brightness diodes available for future experiments are at the longer wavelength as well.

5.6.4 Laser Efficiency Dependence on Length and Total Loss

For the counter-propagating laser configuration the performance of the laser with the same pump absorption (∼ 98%) and fixed total pump absorption as length is varied are investigated. The results are shown in Figures 5.16 and 5.17 for 915 nm

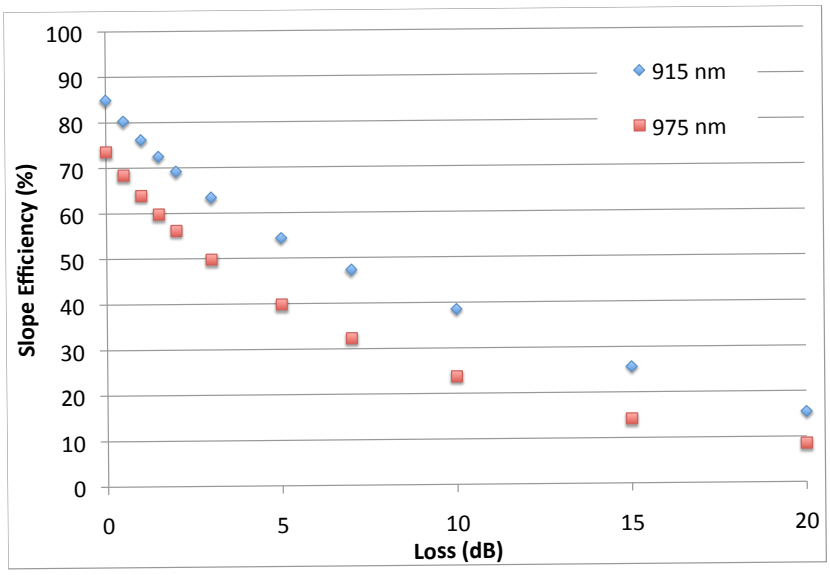

Figure 5.15: Slope efficiency for two pump wavelengths for a 5 m counter-propagating laser.

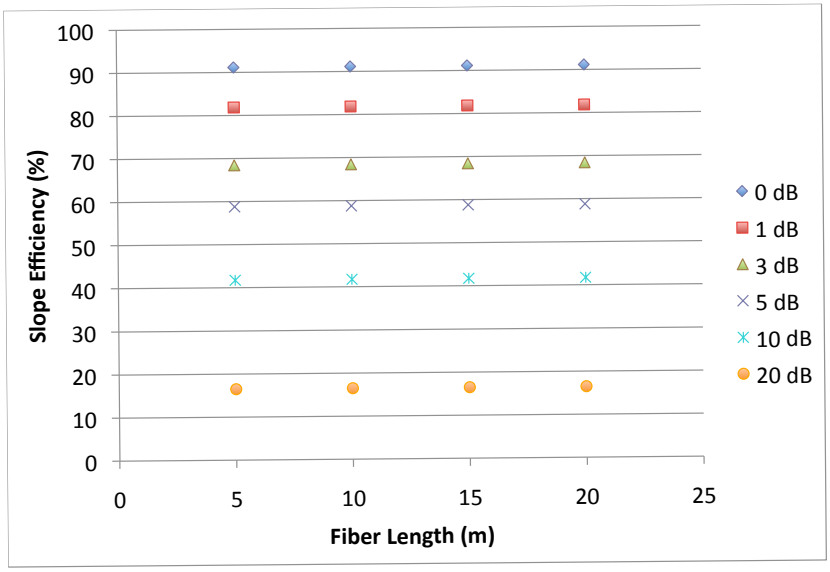

Figure 5.16: Slope efficiency for varying α_s as a function of length for a laser operating at 1064 nm and pumped at 915 nm in the counter-propagating configuration.

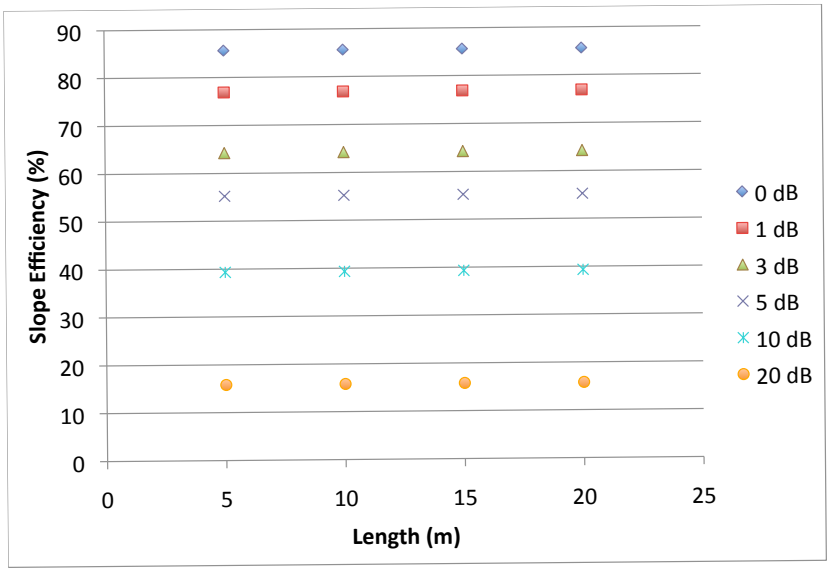

Figure 5.17: Slope efficiency for varying α_s as a function of length for a laser operating at 1064 nm and pumped at 974 nm in the counter-propagating configuration.

and 974 nm pumping respectively. From these figures it is evident that the slope efficiency of the laser is only dependent on the total loss for the laser, and not the fiber length. So, if loss per unit length becomes higher than desired, a higher doping concentration could be employed to facilitate efficient operation of a shorter active fiber length, with the only caveat being that a more robust thermal management scheme will have to be employed.

5.6.5 Amplifier Slope Efficiency Dependence on Seed Power

The slope efficiency for an amplifier seeded with either 84 mW or 6 W was 54%, which prompted investigation of the effect of seed power on slope efficiency for a counter-propagating amplifier. Slope efficiency versus seed power can be seen in Figure 5.18, where the slope efficiency was calculated for a modal loss of 0 dB or

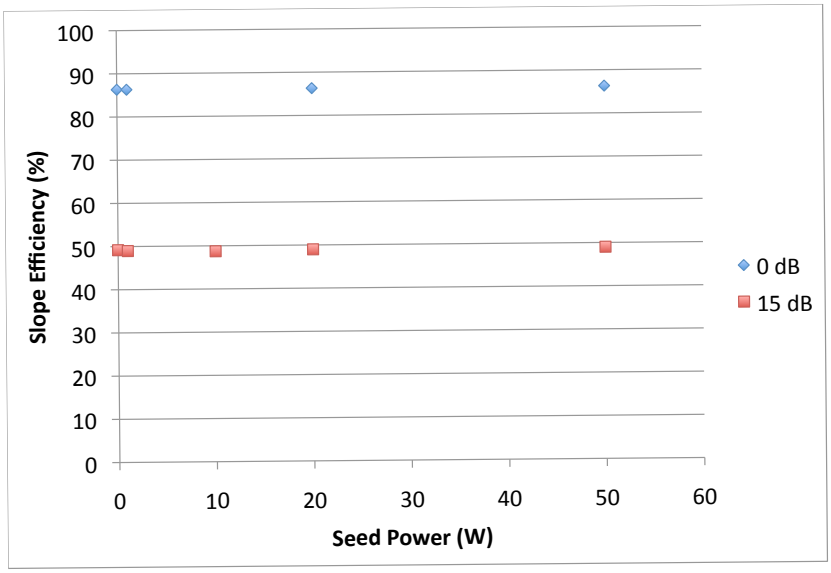

Figure 5.18: Slope efficiency for varying seed power at 1064 nm and pumped at 915 nm in a counter-propagating configuration for $\alpha_s = 0$ and $\alpha_s = 15$ dB.

15 dB. The surprising result is that a larger seed does not affect the slope efficiency of the amplifier, which implies that in either case gain becomes saturated and a larger signal simply saturates the amplifier earlier than a smaller signal, without substantially affecting the increase in total output power.

5.6.6 Comparing Efficiencies for 915 nm and 974 nm Pumping for a Counter-propagating Amplifier Configuration

The counter-propagating configuration was investigated for pumping at 974 nm and 915 nm. For a 1 W seed signal at 1064 nm and the ion concentration adjusted to yield 95% pump absorption for the fiber amplifier, Figure 5.19 shows the slope efficiencies at both 915 nm and 974 nm, where it can be seen that there is an advantage at lower signal loss which disappears at higher loss values for shorter wavelength pumping. Therefore, with a suitable choice of fiber length for high pump absorption

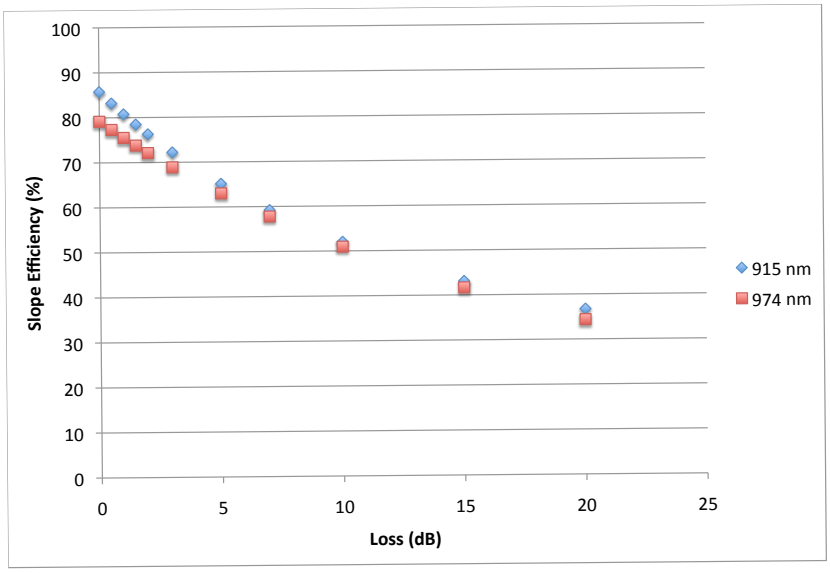

Figure 5.19: Comparison of the slope efficiency for a counter-propagating amplifier configuration seeded with a 1 W 1064 nm seed pumped at either 915 nm or 974 nm.

there is no substantial efficiency advantage to either pump wavelength. However, as pumping at the longer wavelength requires a shorter length of fiber to achieve 95% pump absorption for a real fiber, it is generally preferred for power scaling as a shorter fiber has a higher nonlinear threshold and thus a higher output power can be achieved for long wavelength pumping.

5.6.7 Comparing the Counter-propagating and Co-propagating Configurations for a Fiber Amplifier with Loss

To determine the most advantageous configuration for an amplifier setup, both the counter-propagating and co-propagating configurations are investigated. The results are shown in Figure 5.20, where the counter-propagating configuration has a clear advantage over the co-propagating configuration as was seen in the laser setup. The reasons are the same for the amplifier as they were for the laser, namely that a large

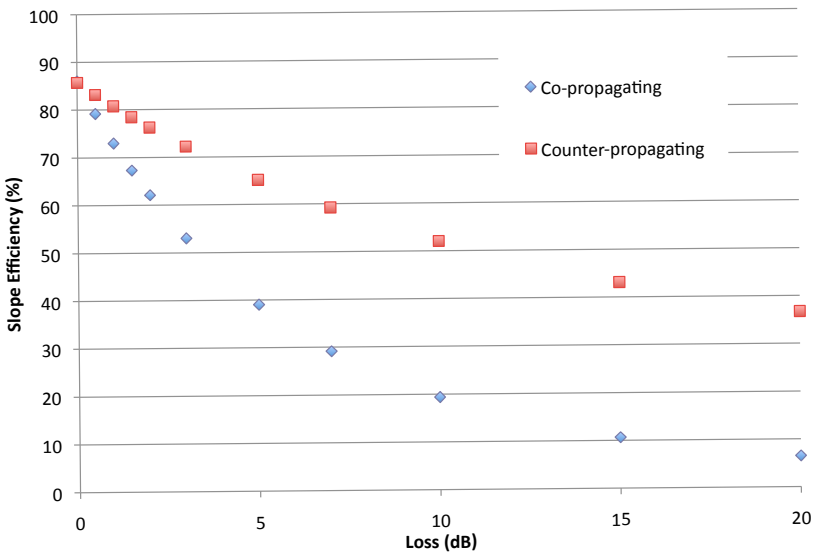

Figure 5.20: Slope efficiency vs loss for the co-propagating and counter-propagating amplifier configurations pumped with 915 nm, and injected with a 1 W 1064 nm seed

signal with only residual pump, as is the case near the output of the co-propagating configuration, results in decreased gain at the end of the gain fiber. So again for maximum power extraction from an amplifier, as is almost always the case when large core fibers are used, the counter-propagating configuration is preferred.

5.6.8 Amplifier Efficiency Dependence on Length and Total Loss

The final investigation was to understand the behavior of the amplifier in the counter-propagating configuration as fiber length was varied, but fundamental loss remained constant. A counter-propagating amplifier configuration pumped at either 974 nm or 915 nm was investigated, the results of which are shown in Figures **??** and 5.22 respectively, where the amplifier was again seeded with a 1W 1064 nm seed. The results show that at either pump wavelength, the slope efficiency of the

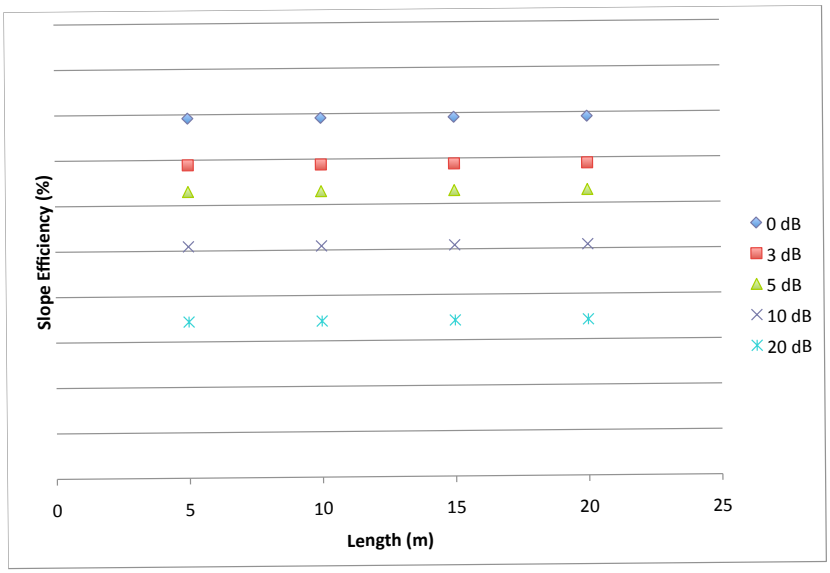

Figure 5.21: Slope efficiency as a function of length for a 1 W seed at 1064 nm pumped at 974 nm.

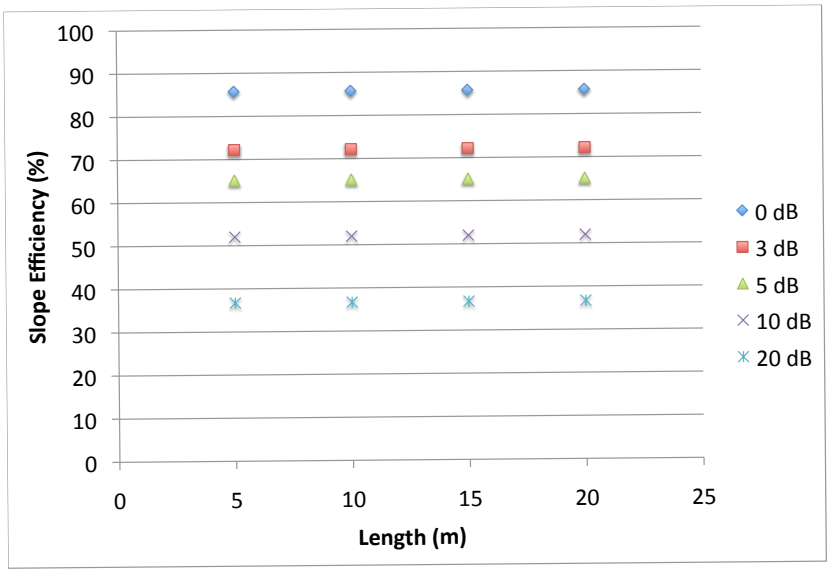

Figure 5.22: Slope efficiency as a function of length for a 1 W seed at 1064 nm pumped at 974 nm.

amplifier was independent of the unit loss, and only depended on the total loss for the amplifier. As was seen earlier, a shorter amplifier will have a higher nonlinear threshold and hence higher output power, and is thus preferred, but in this case there must be a balance between thermal management and output power must be maintained or the amplifier will not have a long lifetime.

5.7 Conclusions

The design of an ESM Yb-doped fiber based on the CCC structure using BPM produced a robust effectively-single-mode-fiber that does not rely on external mode management techniques to achieve single mode operation. With these fibers both lasers and amplifiers were constructed that exhibited behavior consistent with more conventional LMA fiber technology, including reasonable slope efficiencies (75% laser and 54% amplifier), high small signal gain (30.3%) and wavelength dependent small signal gain typical of conventional LMA fibers. Beyond these basic performance criteria, the laser exhibited single mode output at all powers, and irrespective of small mis-alignments of the 0° retro-reflector, provided the laser was above threshold. Similarly the amplifier exhibited single mode output irrespective of alignment conditions as long as a seed was present, and at all powers where the amplifier was operated.

After characterization of the performance of the CCC Yb-doped fiber based lasers and amplifiers was completed, a systematic look at the performance of fiber based systems with signal loss was undertaken. The results were consistent and for the most part applicable to either laser or amplifier systems, namely: slope efficiency depended on total loss rather than the loss per unit length, the counter-ropagating configuration was the preferred setup as it is less sensitive to length as well as loss, and that 974 nm pumping had a slight disadvantage in terms of absolute slope efficiency,

but being able to use shorter lengths of fiber in the system will facilitate a higher nonlinear threshold and therefore a greater maximum output power.

CHAPTER VI

Conclusions

6.1 Develoment of Monlithic Mode-Locking Free Femtosecond Technology

The techniques for generating femtosecond pulses from conventional fabry-perot laser diodes using nonlinear spectral broadening techniques in Yb-doped positive dispersion fiber amplifiers were explored. The concept is to exploit the maturity of current single-mode fiber technology and demonstrate that monolithic mode-locking-free technology is feasible.

The technical approach undertaken was to employ an injection locked fabry-perot laser diode followed by two stages of nonlinear spectral broadening to generate femtosecond pulses. In this thesis it was demonstrated that a gain switched fabry-perot laser diode can be injection locked to generate a single longitudinal mode pulse, and that pulse can be compressed using spectral broadening. By this technique a 60 ps pulse was compressed to 4 ps.

Gain-switched pulses from laser diodes suffer from a low level quasi-cw component, as evidenced by an unbroadened spectral component in the measured SPM spectrum. Efforts made to optimize the operating conditions of the injection locked diode did not improve the observed spectra, and future efforts to produce mode-locking free femtosecond laser technology as begun in this work will need to address

this unbroadened quasi-cw component by either electronic or nonlinear means.

6.2 Demonstration of First Yb-doped Chirally-Coupled-Core Fibers Laser Systems

The first Yb-doped Chirally-Coupled-Core fiber based lasers and amplifiers were demonstrated. Robust single mode performance was shown independent of excitation or any other external mode management techniques. Gain and power efficiency characteristics are not compromised in any way in this novel fiber structure up to the 87 W maximum power achieved. Both the small signal gain of 30.3 dB at 1064 nm, and the wavelength dependence of the small signal gain were comparable to currently deployed large-mode-area fiber technology. The efficiencies of the laser and amplifier were measured to be 75% and 54% respectively.

There is a design trade off in Chirally-Coupled-Core structures between LP_{01} loss and HOM suppression. With this in mind, loss effects on amplifier and laser efficiency in different configurations were investigated. From these investigations it was seen that the slope efficiency depends only on the total loss of the active fiber, and that when loss is present, the counter-propagating configuration has substantial advantages over the co-propagating case. Chirally-Coupled-Core fiber as the technological basis for the next generation of monolithic high power fiber laser systems has been established.

BIBLIOGRAPHY

BIBLIOGRAPHY

[1] V. I. Kruglov, A. C. Peacock, J. D. Harvey, and J. M. Dudley. Self-similar propagation of parabolic pulses in normal-dispersion fiber amplifiers. *J. Opt. Soc. Am. B*, 19(3):461–469, 2002.

[2] Chi-Hung Liu, Guoqing Chang, Natasha Litchinitser, Almantas Galvanauskas, Doug Guertin, Nick Jabobson, and Kanishka and Tankala. Effectively single-mode chirally-coupled core fiber. *Advanced Solid-State Photonics*, pages ME2+, January 2007.

[3] E. Snitzer. Optical maser action of nd^{+3} in a barium crown glass. *Phys. Rev. Lett.*, 7(12):444–446, Dec 1961.

[4] S.B. Poole, D.N. Payne, and M.E. Fermann. Fabrication of low-loss optical fibres containing rare-earth ions. *Electronics Letters*, 21(17):737–738, August 15 1985.

[5] R.J. Mears, L. Reekie, S.B. Poole, and D.N. Payne. Neodymium-doped silica single-mode fibre lasers. *Electronics Letters*, 21(17):738–740, August 15 1985.

[6] Aghapi G. Mordovanakis, Kai-Chung Hou, Yu-Chung Chang, Ming-Yuan Cheng, John Nees, Bixue Hou, Anatoly Maksimchuk, Gerard Mourou, Almantas Galvanauskas, and Bruno Lafontaine. Demonstration of fiber-laser-produced plasma source and application to efficient extreme uv light generation. *Opt. Lett.*, 31(17):2517–2519, 2006.

[7] Kai-Hsiu Liao, Aghapi G. Mordovanakis, Bixue Hou, Guoqing Chang, Matthew Rever, Gerard A. Mourou, John Nees, and Almantas Galvanauskas. Generation of hard x-rays using an ultrafast fiber laser system. *Opt. Express*, 15(21):13942–13948, October 2007.

[8] R. Fork, B. Greene, and C. Shank. Generation of optical pulses shorter than 0.1 psec by colliding pulse mode-locking. *Quantum Electronics, IEEE Journal of*, 17(12):2406–2406, Dec 1981.

[9] D. Grischkowsky and A. C. Balant. Optical pulse compression based on enhanced frequency chirping. *Applied Physics Letters*, 41(1):1–3, 1982.

[10] C. V. Shank, R. L. Fork, R. Yen, R. H. Stolen, and W. J. Tomlinson. Compression of femtosecond optical pulses. *Applied Physics Letters*, 40(9):761–763, 1982.

[11] J. G. Fujimoto, A. M. Weiner, and E. P. Ippen. Generation and measurement of optical pulses as short as 16 fs. *Applied Physics Letters*, 44(9):832–834, 1984.

[12] W. H. Knox, R. L. Fork, M. C. Downer, R. H. Stolen, C. V. Shank, and J. A. Valdmanis. Optical pulse compression to 8 fs at a 5-khz repetition rate. *Applied Physics Letters*, 46(12):1120–1121, 1985.

[13] J. Mark, L. Y. Liu, K. L. Hall, H. A. Haus, and E. P. Ippen. Femtosecond pulse generation in a laser with a nonlinear external resonator. *Opt. Lett.*, 14(1):48–50, 1989.

[14] D. E. Spence, P. N. Kean, and W. Sibbett. 60-fsec pulse generation from a self-mode-locked ti:sapphire laser. *Opt. Lett.*, 16(1):42–44, 1991.

[15] Daniel K. Negus, Luis Spinelli, Norman Goldblatt, and Gilles Feugnet. Sub-100 femtosecond pulse generation by kerr lens mode-locking in ti:al2o3. In *Advanced Solid State Lasers*, page SPL7. Optical Society of America, 1991.

[16] François Salin, Jeff Squier, and Michel Piché. Mode locking of ti:ai2o3 lasers and self-focusing: a gaussian approximation. *Opt. Lett.*, 16(21):1674–1676, 1991.

[17] U. Keller, G. W 'tHooft, W. H. Knox, and J. E. Cunningham. Femtosecond pulses from a continuously self-starting passively mode-locked ti:sapphire laser. *Opt. Lett.*, 16(13):1022–1024, 1991.

[18] O. E. Martinez. Grating and prism compressors in the case of finite beam size. *J. Opt. Soc. Am. B*, 3(7):929–934, 1986.

[19] O. E. Martinez, J. P. Gordon, and R. L. Fork. Negative group-velocity dispersion using refraction. *J. Opt. Soc. Am. A*, 1(10):1003–1006, 1984.

[20] E. Treacy. Optical pulse compression with diffraction gratings. *Quantum Electronics, IEEE Journal of*, 5(9):454–458, Sep 1969.

[21] Donna Strickland and Gerard Mourou. Compression of amplified chirped optical pulses. *Optics Communications*, 56(3):219 – 221, 1985.

[22] J.D. Kafka and T.M. Baer. Peak power fluctuations in optical pulse compression. *Quantum Electronics, IEEE Journal of*, 24(2):341–350, Feb 1988.

[23] J. D. Kafka, B. H. Kolner, and T. Bauer. Compression of pulses from a continuous-wave mode-locked nd:yag laser. *Opt. Lett.*, 9(11):505, 1984.

[24] Govind Agrawal. *Nonlinear Fiber Optics, Fourth Edition.* Academic Press, October 2006.

[25] D. Anderson, M. Desaix, M. Karlsson, M. Lisak, and M L. Quiroga-Teixeiro. Wave-breaking-free pulses in nonlinear-optical fibers. *J. Opt. Soc. Am. B*, 10(7):1185, 1993.

[26] K. Tamura and M. Nakazawa. Pulse compression by nonlinear pulse evolution with reduced optical wave breaking in erbium-doped fiber amplifiers. *Opt. Lett.*, 21(1):68, 1996.

[27] M. E. Fermann, V. I. Kruglov, B. C. Thomsen, J. M. Dudley, and J. D. Harvey. Self-similar propagation and amplification of parabolic pulses in optical fibers. *Phys. Rev. Lett.*, 84(26):6010–6013, Jun 2000.

[28] Jens Limpert, T. Schreiber, T. Clausnitzer, K. Zöllner, H. Fuchs, E. Kley, H. Zellmer, and A. Tünnermann. High-power femtosecond yb-doped fiber amplifier. *Opt. Express*, 10(14):628–638, 2002.

[29] V. Gapontsev, D. Gapontsev, N. Platonov, O. Shkurikhin, V. Fomin, A. Mashkin, M. Abramov, and S. Ferin. 2 kw cw ytterbium fiber laser with record diffraction-limited brightness. *Lasers and Electro-Optics Europe, 2005. CLEO/Europe. 2005 Conference on*, pages 508–, June 2005.

[30] Kai-Chung Hou, Ming-Yuan Cheng, Almantas Galvanauskas, Doruk Engin, Rupak Changkakoti, and Pri Mamidipudi. Multi-mw peak power scaling of single-transverse mode pulses using 80-m core yb-doped lma fibers. In *Advanced Solid-State Photonics*, page MF5. Optical Society of America, 2006.

[31] M. D. Feit and Jr. J. A. Fleck. Light propagation in graded-index optical fibers. *Appl. Opt.*, 17(24):3990–3998, 1978.

[32] R. Scarmozzino, A. Gopinath, R. Pregla, and S. Helfert. Numerical techniques for modeling guided-wave photonic devices. *Selected Topics in Quantum Electronics, IEEE Journal of*, 6(1):150–162, Jan/Feb 2000.

[33] A. Hardy and R. Oron. Signal amplification in strongly pumped fiber amplifiers. *Quantum Electronics, IEEE Journal of*, 33(3):307–313, Mar 1997.

[34] A.A. Hardy and R. Oron. Amplified spontaneous emission and rayleigh backscattering in strongly pumped fiber amplifiers. *Lightwave Technology, Journal of*, 16(10):1865–1873, Oct 1998.

[35] I. Kelson and A.A. Hardy. Strongly pumped fiber lasers. *Quantum Electronics, IEEE Journal of*, 34(9):1570–1577, Sep 1998.

[36] Martin E. Fermann. Single-mode excitation of multimode fibers with ultrashort pulses. *Opt. Lett.*, 23(1):52–54, 1998.

[37] Jeffrey P. Koplow, Dahv A. V. Kliner, and Lew Goldberg. Single-mode operation of a coiled multimode fiber amplifier. *Opt. Lett.*, 25(7):442–444, 2000.